Physics – Uspekhi **61** (7) 645 – 691 (2018)

REVIEWS OF TOPICAL PROBLEMS

PACS numbers: **62.25. – g**, 68.65.Pq, 73.22.Pr

Physics and chemistry of graphene. Emergentness, magnetism, mechanophysics and mechanochemistry

E F Sheka, N A Popova, V A Popova

DOI: https://doi.org/10.3367/UFNe.2017.11.038233

Contents

Abstract. Graphene is considered a specific object whose electronic structural features are presented in the light of the general concept of emergent phenomena that arise as a result of a quantum phase transition caused by the breaking of continuous symmetry. This review starts by examining the spin symmetry breaking of the graphene electron subsystem caused by the correlation of its odd p_z-electrons that depends on the distance between these electrons and becomes noticeable when the shortest distance, determined by the C = C bond length, exceeds the critical magnitude $R_{cr} = 1.395$ Å. The symmetry breaking is reliably predicted by the unrestricted Hartree–Fock (UHF) formalism, which provides a sufficient level of quantitative self-consistent description for the problem. Empirical support has been given to and reliable certification obtained for UHF emergents such as (i) open-shell electron spin-orbitals; (ii) splitting and/or spin polarization of electron spectra; (iii) a spin-mixed ground state and, as a consequence, violation of the exact spin multiplicity of electronic states, and (iv) the existence of local spins at zero total spin density. Using this approach greatly expands our understanding of the ground state of graphene and other sp^2 nanocarbons and not only gives a clear insight into the spin features of graphene chemistry, accentuating its emergent character, but also expectedly predicts the occurrence of new graphene physics-related emergents. In the latter case, symmetry breaking is relevant for both the spin system and time reversal and imposes on graphene special physical properties such as ferromagnetism, superconductivity, and topological nontriviality. This review shows, for the first time, that not only the ferromagnetism but also the mechanical properties of graphene are essentially emergent, extending this feature to the entire physics of graphene.

Keywords: graphene, graphane, open-shell molecules, emergent phenomena, spin symmetry breaking, unrestricted Hartree – Fock (UHF) quantum-chemical approximation, Dirac quasirelativistic approach, hexagonal honeycomb structure, Dirac fermions, spin-orbital coupling, local spins, time reversal symmetry breaking, topological nontriviality, high temperature ferromagnetism, interfacial superconductivity, mechanical properties, static deformation, dynamic deformation, covalent bonds

E F Sheka, N A Popova, V A Popova Peoples Friendship University of Russia (RUDN),
ul. Miklukho-Maklaya 6, 117198 Moscow, Russian Federation
E-mail: sheka@icp.ac.ru

Received 16 May, revised 6 November 2017
Uspekhi Fizicheskikh Nauk **188** (7) 720 – 772 (2018)
DOI: https://doi.org/10.3367/UFNr.2017.11.038233
Translated by Yu V Morozov; edited by A Radzig

As is commonly the case with new emergent phenomena, it is the experiments that tell us these things must be true, not the theories. Theories can help us better understand the experiments, in particular by providing a tangible prototype vacuum, but the deeper reason to accept these conclusions is that the experiments give us no alternative.
(R Laughlin [2, p. 298])

1. Introduction

This review presents graphene, the remarkable Dirac material, in the context of the comprehensive answer to one of the main questions in the graphene science — graphenics — specified in the epigraph. This question concerns the relationship between empirical and virtual graphenics, arising from the unique position of the virtual partner. Indeed, theoretical and computational studies have never before attracted so much attention in the natural sciences. The ready availability of modern computing methods and relative ease of their implementation, in contrast to the ever-growing complication of real experiments and high demands on the experimental conditions, put virtual graphenics at an advantage and give it reason to claim the role of conceptual leader. It is not for nothing that authors of numerous publications (amounting to many hundreds now) declare in concluding remarks the discovery of new properties in graphene, and the creation of novel graphene-like materials and/or methods allowing the desired properties to be imparted to graphene. But how do matters actually stand? Are the claims that virtual graphenics are mainstream for their leading role justified and what is behind them if they are? Are there any very important features of graphene left out of the field of view of researchers? The present review is an attempt to answer these questions.

The reliability of any research technique and results obtained by it depend on the instrumentarium. A major tool in modern virtual graphenics is computational programs with algorithms based on the density functional theory (DFT) in relation to either molecules or crystals with a given structural cell repeated in space by application of periodic boundary conditions. The main variants of the programs being used are restricted quantum-chemical (RQCh) approximation programs without regard for electron spin. Another widely used tool is constituted by programs based on tight binding (TB) approximation algorithms intended largely to calculate crystal properties. They are also consistent with the RQCh approximation, whereas the preliminary determination of structural computational elements is made with the use of DFT programs.

The analysis of computed results indicates that the maximum accuracy of empirical energy data lies within 10–15%. The accuracy of the calculated structural data is of roughly the same order. Such accuracies are quite sufficient in most cases if they do not include the concealment of some qualitative changes. However, in the case of graphene, a change in the length of a C=C bond in a benzene molecule by 1.5% of 1.40 Å, i.e., up to 1.42 Å, results in a significant qualitative rearrangement of the closed-shell benzene electron subsystem into the open-shell electron subsystem of graphene. This transition is accompanied by the loss of a few percent of energy and goes beyond calculations by DFT and TB methods.

However, a system with a thermodynamically large number of electrons exhibits specific states experiencing low-energy quantum phase transitions that lead to the appearance of new properties known as *emergent* [1–5]. The open-shell structure of an electron system is one of these properties which allows graphene to be considered in terms of the emergentness of its properties. Because these peculiarities of graphene properties are impossible to clarify using DFT and TB algorithms, the last methods should be discarded as unsuitable for the purpose. Therefore, the discussion of the problem in question is based on the results of the unrestricted Hartree–Fock (UHF) method, the reliability of which was evaluated in each concrete case by comparison with experimental data. This work resulted in the creation of the emergent empirical and virtual graphenics concept submitted to the judgment of the reader.

The layout of the review is as follows. It consists of three main Sections (2–4), the Introduction, and the Conclusions. Section 2 describes the emergentness of a many-electron system and UHF emergents of open-shell electron systems; it presents evidence of their physical reality for molecules in general, and graphene molecules in particular. The efficiency of the UHF approximation for describing emergent properties of graphene molecules is exemplified by their spin chemistry with reference to the conservation of qualitative and quantitative characteristics of UHF emergents, taking into consideration relativistic effects. A brief description of the graphene crystal electronic structure is presented in the quasirelativistic approximation, with the discussion of potential emergent phenomena accounting for the topological nontriviality of graphene. Section 2 is concluded by comments on insurmountable difficulties hampering graphene transition from semimetal to semiconductor. In Section 3, the emergent physics of graphene is considered in terms of its ferromagnetism and superconductivity. Section 4 deals with unification of the emergent nature of graphene physics and chemistry as exemplified by its mechanophysics and mechanochemistry. The final section contains concluding remarks on the universal character of the unique properties of graphene determined by its emergent electron system due to spin symmetry and time-reversal symmetry breaking.

2. Fundamentals of graphene emergentness

2.1 Emergent phenomena in a many-electron system

The Nobel Prize winner in Physics 1977 P W Anderson launched the discussion of emergent phenomena in physics in his famous article "More is different" [1], in which he considered problems arising from the analysis of peculiarities in the solution of many-electron Hamiltonians, namely the Hartree–Fock Hamiltonian, when the standard symmetrical (read, RQCh) solutions to the restricted Hartree–Fock (RHF) method are at variance with physical reality and are substituted by UHF approximation. The substitution concerns the manner of wave function presentation leaving the Hamiltonian unaltered. The discussion was continued by other reputed physicists, including one more Nobel Prize laureate in Physics 1998 R B Laughlin, and opened the door to a realm of unexpected phenomena [2–6]. The crux of the problem is that RHF solutions are consistent with the reductionist view of the electron system, according to which a system of many interacting electrons adiabatically reduces to the sum of solutions for individual electrons, when the interelectron interaction turns off. In contrast, a UHF solution does not obey such a law; as a result, there are new residual (so-called emergent) phenomena. Thus, the key question to answer is whether these residual phenomena can

be regarded as compatible with physical reality. The answer divides quantum chemisists into reductionists and emergentists, saying NO and YES, respectively. Coming back to virtual graphenics, it is worth noting that the majority of respondents belong now to the reductionists; the emergentists are in a minority, and the present review provides actually the first attempt to represent their views focused on the peculiar electronic properties of graphene.

The transition to the exposition of emergent graphenics needs to be preceded by considering the basic provisions of the emergentness concept that apply in full measure to many-electron systems. The concept is intended " ...to characterize certain phenomena as 'new', which is quite unexpected in the psychological sense, unexplainable in theoretical terms, and unpredictable based on the information about spatial parts or other components of systems" [1] [7]. According to this concept and Anderson's definition [1], an emergent phenomenon represents a collective effect of a large number of particles (electrons) that needs very low energy to manifest itself and cannot be strictly derived from microscopic equations of motion; it rapidly disappears as the system disintegrates into constituent components (electrons). Emergent phenomena obey certain laws formulated as Earman's [8] and Butterfield's [9] principles:

- Earman principle states: although idealizations are useful and perhaps even necessary for progress in physics, sound principles of interpretation suggest that no effect can be regarded as a true physical effect if it disappears upon cancellation of idealizations.
- Butterfield principle states: a weaker but still vivid, new, and reliable behavior develops before a limit is reached, i.e., for finite N. It is this weaker behavior that is the physically real one.

The quality under discussion regarding emergent phenomena was pointed out in the 1998 Nobel lecture of R Laughlin [2]. According to this outstanding physicist (whose work was a decade ahead of the graphene era), the reality of emergent phenomena is confirmed by experiment rather than theory. Theories help to better understand experimental findings, but there is no alternative to experiments. Laughlin concluded his lecture with the following words:

I have no idea whether the properties of the universe as we know it are fundamental or emergent, but I believe the mere possibility of the latter must give string theorists pause for it would imply that more than one set of microscopic equations is consistent with experiment — so that we are blind to the microscopic equations until better experiments are designed — and also that the true nature of these equations is irrelevant to our world. So the challenge to conventional thinking about the universe posed by these small-science discoveries is actually troubling and very deep.... I emphasize these things because there is a regrettable tendency in solid-state physics to equate an understanding of nature with an ability to model, an attitude that sometimes leads to overlooking or misinterpreting the higher organizing principle actually responsible for an effect.

[1] Such a formulation of the emergentness concept with respect to a physical system is consonant with its general philosophical formulation: "Emergentness is a type of a sudden change counterposed to a usual quantitative change (result). Emergentness is impossible to explain rationally or derive logically from the preceding existence levels of initial elements; it is declared to be an indecomposable 'simple integrity' (*Sovremennyi Filosofskii Slovar* (Modern Philosophical Dictionary) Moscow: Panprint, 1998).

There is nothing new in the statements that the concept of emergent phenomena has direct relevance to graphene [6, 10, 11]. However, the authors of the present review had arrived at this conclusion before they came to know these publications, based on the unique properties of this material alone. We were astounded to see how difficult it was to find an article, among the huge number of papers concerning graphene one way or another, that did not contain a reference to the standard set of unique applications anticipating graphene as the principal motivation for undertaking a given investigation. This fact is probably a natural reaction to the unprecedentedly high number of publications, on the one hand, and the wide scope of problems they have covered, on the other hand. This consideration appears to be the sole code opening the door to the realm of an incredible intermixture of scientific disciplines, methods, objectives, and results of research. That part of the considerable amount of graphene information that was obtained in basic research gives indisputable evidence of the unique qualities of graphene as the thus far sole known object that could integrate multiple interests of natural sciences from mathematics to geology. On the other hand, the considerable body of currently available data that are difficult to comprehend and understand in full measure inevitably leads to differentiation of the graphene science into separate branches, such as physics, chemistry, biophysics and medical biology. In all of them, graphene retains its uniqueness, demonstrating an amazing versatility. The question is, what is the cause of graphene's universal uniqueness?

The search for the answer demonstrates that a specific feature that probably underlies the universal uniqueness of a many-electron system arises from its fundamental properties. One of them immediately attracting attention is continuous symmetry, namely spin and temporal symmetries. It is exactly this issue of symmetry breaking and its relation to emergentness in a many-electron system that was raised in the work of Andersen [1] cited in a preceding paragraph. It is well known that the substitution of RHF functions by their UHF analogs in the transition from the RHF formalism to the UHF one means the transition from a single-determinant spin-symmetric approximation to the double-determinant one with a broken spin symmetry, which was the embodiment of the well-known Löwdin ideologeme "different orbitals for different spins" [12].

The essence of the arising problem consists in the fact that UHF wave functions as eigenfunctions of both the electronic Hamiltonian (identical with the Hamiltonian in the RHF formalism) and the operator S_z of spin z-projection can or cannot (because of spin symmetry breaking) perform this role for the spin operator squared $\hat{S}^2$. The distinction between UHF and spin-symmetric RHF solutions is manifested as a decrease in the total system's energy: $\Delta E^{\mathrm{RU}} = E^{\mathrm{RHF}} - E^{\mathrm{UHF}} > 0$, and well-apparent spin mixing ('contamination'): $\Delta\hat{S}^2 = \hat{S}^2_{\mathrm{UHF}} - \hat{S}^2_{\mathrm{exact}}$, which, in turn, violates the purity of spin multiplicity of the ground state and results in the appearance of additional spin density. The set of these quantities forms the characteristic feature that, in conformity with the Butterfield principle, makes the electron system of interest capable of emergent behavior.

Conversely, adherents of the reductionist concept not infrequently describe spin mixing as a drawback of the UHF method leading to erroneous conclusions (see papers [13, 14] and references cited therein). At the same time, there is no doubt that the existence of nonzero values of ΔE^{RU} and $\Delta\hat{S}^2$ suggests a significant correlation between electrons that

requires the use of multideterminant schemes of configuration interaction (CI) to be adequately described. In addition, this concept provides a basis for the unshakeable opinion that, could the double-determinant UHF approximation as the first step of CI be improved up to the full-scale CI theory, it would be possible to expect logical restoration of continuous symmetry and elimination of spin contamination.

However, R Laughlin noted in Ref. [2] that the restoration of continuous symmetry is far from being questionless. Indeed, "*...if the system contains a thermodynamically large number of particles it can happen that a small change to the equations of motion results in a violent rearrangement of the ground state and low-lying excitations and a corresponding breakdown of the one-to-one mapping. This is a quantum phase transition. We say that two states are the same phase of matter if they can be slowly transformed into each other without encountering a quantum phase transition, and different phases of matter if they cannot*."

It is obvious in this context that two situations are conceivable as regards spin symmetry breaking in the UHF approximation: (1) the anticipation of restoration of continuous symmetry by the transition to multideterminant spin-projective wave functions of higher levels of the CI theory, and (2) the impossibility of restoring continuous symmetry in this way and recognition of symmetry breaking and the existence of phase transition in a given electron system prone to the manifestation of emergentness. The former case actually takes place in small systems of several light atoms (see papers [4, 15] and references cited therein). Polyatomic systems having a *thermodynamically greater number of particles* are more tolerant of symmetry breaking and the accompanying quantum phase transition [1–5], which makes the UHF solution a good approximation for the description of their ground state.

Simultaneously, the glossary of the ground state is inevitably enriched in new terms, sometimes referred to as 'new order parameters' [4] that indicate novel properties acquired by electron systems and represented as *emergents*. There is a rather wide set of UHF emergents. For example, an incomplete list of the respective quantities includes the aforementioned drop in the system's energy ΔE^{RU} or spin mixing $\Delta\hat{S}^2$, supplemented by splitting or spin polarization of energy terms, distortion of exact spin multiplicity of electronic states, the presence of local spins with a given value for each atom even for zero total spin density, quantitative characteristics of molecular and atomic chemical susceptibility (activity), etc.

The emergent character of the ground state has a direct bearing on graphene. Empirically, graphene specimens divided into micro- (nano-) and macrofragments make up two large pools characterized by spatially unquantized (molecular) and quantized (crystalline) electronic properties, respectively. These two pools comprise graphene-based materials with low- and high-performance operational characteristics in the respective applications [16]. Because continuous symmetry breaking is independent of concrete details of individual objects [1–5], it is a universal property intrinsic to the entire graphene family and, therefore, a reliable marker in the search for common emergent phenomena characteristic of the properties of interest in the sea of available facts and observations. The review is the first example of such a search, which has already shown that the concept of continuous symmetry breaking allows us to unite specific spin-dependent chemical properties of graphene molecules, including mechanochemical, topochemical, and biomedical ones with spin-dependent physical properties of crystals, such as ferromagnetism, superconductivity, and topological nontriviality. Emergentness of the latter is further strengthened by a time-reversal symmetry breaking. As follows from the epigraph set at the beginning of this review, categorization of these phenomena as emergents is based on the consistency between experimental data and their theoretical interpretations.

2.2 UHF emergents of open-shell molecules and physical reality

Far from all molecules exhibit emergent properties. Therefore, they are categorized into two significantly differing types: closed-shell molecules, having spin-symmetric electron shells (spin-orbitals) without specific emergent features, and open-shell ones, showing emergent properties. The type of a given molecule depends on its internal electronic and structural characteristics. The main distinctive feature of open-shell molecules is unsaturated valence bonds or odd electrons. As a consequence, molecules with saturated valence bonds are, as a rule, assigned to the first type and turn into open-shell molecules only after inducing in them in one way or another the bond dissociation. However, the presence of unsaturated valence bonds, though necessary, is not always sufficient for a molecule to acquire open-shell properties, as exemplified by a benzene molecule having six odd p_z-electrons with all shells closed and containing two oppositely spinning electrons each. However, when the distance between p_z-electrons determined by the length of the C=C bond exceeds $R_{\mathrm{cr}} = 1.395$ Å, molecules composed of a set of benzene (benzenoid) rings become open-shell structures [17].

The family of sp^2-nanocarbons, including fullerenes, carbon nanotubes, and graphene, comprises a unique set of molecules with multiple equilibrium C=C bonds, most of which are longer than R_{cr}. The electronic structure of such molecules undergoes quantum phase transition accompanied by a continuous symmetry breaking and gaining emergent properties. The experience based on numerous quantum-chemical calculations summarized in monographs [18, 19] has shown that the UHF formalism providing a basis for the statement of the emergentness question [1] reliably reveals the open-shell character of these molecules and spin symmetry breaking.

It was mentioned above that the possibility of restoring continuous symmetry by applying higher approximations of the CI theory to open-shell molecules with broken spin symmetry has been discussed by many authors. However, the convincing theoretical and empirical data obtained for sp^2-nanocarbons do not confirm such a possibility. Suffice it to say that a computing experiment with 14 polyaromatic radicals using various CI approaches, such as UMP2, QCISD, UHF, and UDFT [20], has demonstrated that the degrees of spin contamination $\Delta\hat{S}^2$ suggesting the open-shell character of the molecules are in excellent agreement among themselves for the first three methods, whereas the absence of contamination in the case of UDFT gives evidence of the closed-shell nature of the same molecules. Deviation of molecular energies in the UHF approximation from those obtained with the use of higher CI approximations does not exceed 10%. The UHF approximation based on the wave functions is evidently well adapted for describing symmetry breaking effects, whereas the DFT formalism is less suitable for the purpose, as mentioned by many authors [21, 22].

Each UHF wave function generates a nonzero matrix with a spin density, whose real and imaginary parts are the spin density and spin current density, respectively, forming an

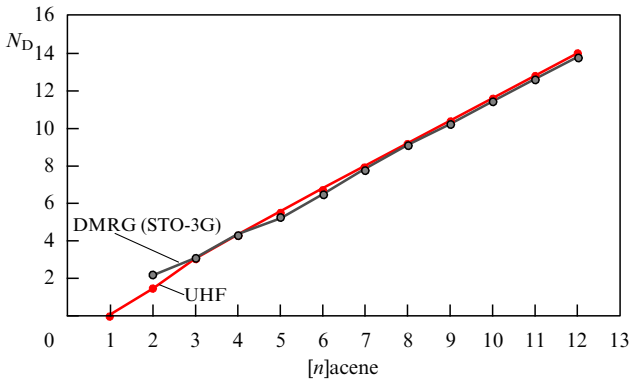

Figure 1. Total number N_D of effectively unpaired electrons in n-polyacenes calculated with the use of DMRG (density matrix renormalization group, STO-3G) and UHF approximations. (Adapted from Ref. [29].)

emergent spin structure [23] with additional quantitative characteristics, including total, N_D, and partial with respect to each atom, N_{DA}, numbers of effectively unpaired electrons [24–26]; these characteristics determine the radical state of the molecule as a whole and of its individual atoms at the quantitative level. For carbonaceous molecules with an even number of electrons and the equal numbers of electrons with different spins, $N_\alpha = N_\beta$, the quantity $N_D = 2\Delta\hat{S}^2$. Both quantities, N_D and N_{DA}, lend themselves to theoretical and experimental verification. Thus, Fig. 1 presents for a set of n-polyaromatic hydrocarbons (n-PAH) the N_D values calculated with the aid of UHF algorithms [2] and the density matrix renormalization group (DMRG) method (see paper [29] and references cited therein).

Clearly, the two sets of data in Fig. 1 are virtually identical. Moreover, the linearly growing dependence of $N_D(n)$ on the number of benzenoid units in molecules accounts fairly well for the difficulty of experimental synthesis of longer n-PAH, among which pentacene ($n = 5$) is the last well characterized polyacene. It turned out that higher polyacenes are actually chemically reactive, which accounts for the existence of PAH with $n = 6$, 7, and 8 only in a modified form, where the additionally introduced protective groups inhibit the high chemical activity inherent in these molecules, or in crystalline neutral matrices at very low temperatures. Molecules with $n > 8$ cannot generally be obtained by chemical synthesis.

In addition to indirect manifestation of N_D, convincing direct evidence of its existence has been obtained in the past decade by scanning its N_{DA} fractions over atoms of open-shell molecules by noncontact atomic-force microscopy (NC-AFM) with a carbon oxide molecule at the tip of the probe (CO tip) (see papers [30, 31] and references cited therein). Pentacene and a set of olympicenes and triangulenes consisting of condensed benzenoid rings with $n = 5$ constitute the pioneer portion of the molecular pool investigated up to now by this method. The AFM image of a pentacene molecule presented in the left panel of Fig. 2a gives evidence of nonuniform interaction between the oxygen atom at the tip apex of the needle and molecule atoms: it is most intense in the center but subsides toward the periphery. The AFM image is consistent with calculated brightness-inverted atomic N_{DA} maps of these molecules in Fig. 2b, where flare spots correspond to atoms with maximum chemical activity [29].

After the manuscript had been submitted for publication, an article appeared that reported an alternative AFM option taking advantage of the needles of a new configuration having a lone oxygen atom at the tip end (CuO_x tip) [32]. The right panel of Fig. 2a demonstrates an AFM image of a 3, 4, 9, 10-perylene tetracarboxylic dianhydride (PTCDA) molecule. Unlike the preceding case, the color contrast of the AMF image obtained by scanning the molecule with the CuO_x tip allows revealing carbon atoms most actively interacting with the oxygen atom at the needle tip (as flare spots). Due to this,

[2] Graphene and other sp^2 nanocarbons are assigned to so-called 'singlet' open-shell molecules having equal numbers of electrons with spins α and β: $N_\alpha = N_\beta$. UHF calculations of such molecules encounter difficulties related to the initial electron density matrices, because the above equality makes them identical for both spin families. The problem was solved for the first time with the CLUSTER-Z1 program that was used to obtain the results summarized in monographs [18, 19] and presented in this review. It was proposed that the results of these calculations be used in the triplet (or higher) spin state as the zero approximation for electron density matrices [26]. Today, this principle is applied in the popular NNChem program complex [27]. The problem is specifically stipulated for the set of Gaussian-03 programs [28].

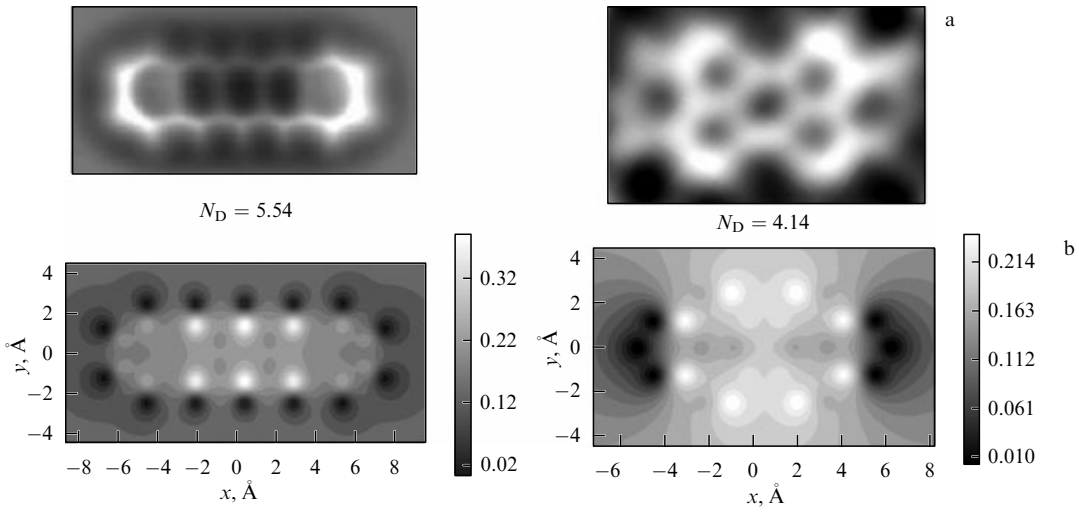

Figure 2. (a) Atomic-resolution AFM images of pentacene molecules on the Cu(111) surface (CO tip) and PTDCA on the Ag(l 11) surface (CuO_x tip), as adapted from papers [30] and [32], respectively. (b) Distribution of calculated N_{DA} values for pentacene (left) and PTDCA (right) molecules; adapted from papers [29] and [33], respectively.

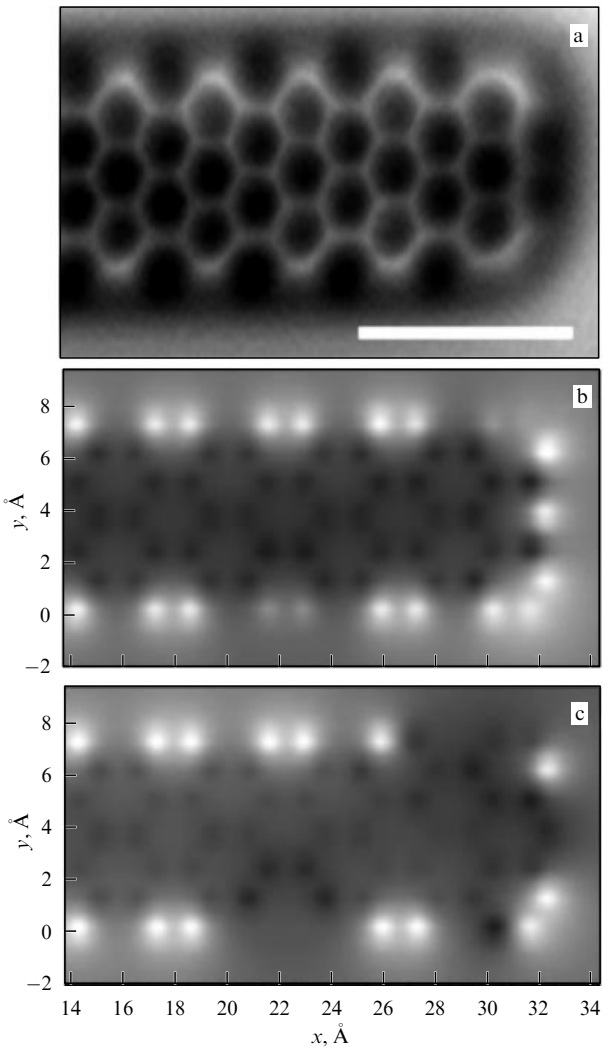

Figure 3. (a) Atom-resolved AFM image of a graphene nanoribbon with armchair edges and a zigzag end; the measured portion is 1 nm (adapted from Ref. [34]). Distributions of N_{DA} (b) and absolute spin density (c) over atoms of a (15, 3)NGr ribbon molecule with zigzag edges [33]. Neither edges nor ends of graphene ribbons were chemically terminated in the calculations.

the AFM image is in excellent agreement with the calculated N_{DA} map of the PTCDA molecule (Fig. 2b), clearly identifying atoms with a maximum chemical activity. Similar agreement was also observed between the AMF image [32] and the calculated N_{DA} map of a dicorannulene molecule [33] having a complicated configuration of condensed benzenoid units.

Analogous accordance was documented for a graphene nanoribbon with unterminated ends and edges [34] (see its AMF image obtained by scanning a $(n, 3)$-nanoribbon with a CO tip in Fig. 3a). The image — perfectly consistent with the calculated N_{DA} map of the nanographene molecule (15, 3)NGr (Fig. 3b) — shows the well-apparent two-zone structure of the graphene pool of effectively unpaired electrons. On the other hand, the set of the data presented in Figs 1–3 provides compelling evidence that N_D and N_{DA} emergents of sp^2 nanocarbons are physically real entities.

Results of UHF calculations suggest zero total spin density generated by effectively unpaired electrons in open-shell molecules with an even number of valence electrons. However, the spin density on each atom of the molecule differs in this case from zero; it changes both magnitude and sign while passing from one atom to another and thereby ensures 'antiferromagnetic' nullification of total density. Figure 3c plots the distribution of the absolute spin density over atoms of a (15,3)NGr molecule fragment. Evidently, spin density is highest in edge atoms, as in N_{DA}. However, in contrast to the N_{DA} map, the basal plane is quite apparent against the light of spin density, because the difference between densities at the edges and in the plane is much smaller than in the image of effectively unpaired electrons. The overall picture presented in Fig. 3b, c is typical of any open-shell molecule and suggests one more characteristic emergent, namely a system of local spins with spin density varying in a wide range and subordinating to antiferromagnetic nullification of its total value, if $N_\alpha = N_\beta$. Now, after we proved that UHF emergents of open-shell molecules represent a physical reality, let us consider their manifestations in the graphene electronic structure at greater length.

2.3 Local emergents in the landscape of graphene molecules

Graphene molecules actually comprise a practically incalculable number of substances formed by planar benzenoid ring clusters of various sizes and shapes. Despite such great diversity, graphene molecules possess a set of common properties determined by UHF emergents. Let us consider them as exemplified by rectangular unterminated (bare) and terminated (framed) (n_a, n_z) NGr fragments (n_a and n_z number benzenoid cycles along fragment armchair and zigzag edges, respectively). In the examples below, termination is extended over all edge atoms and effected by bonding to each of them one hydrogen or oxygen atom or a hydroxyl group. The attachment of hydrogen and hydroxyl subtracts one odd electron from each atom, whereas oxygen displaces two electrons.

Table 1 presents three emergent quantities: ΔE^{RU}, $\Delta\hat{S}^2$, and N_D, representing a criterial triplet of any open-shell molecule [35]. These 'first line' quantities are supplemented by the magnetic constant J (see Section 3.2 for more details about the role and determination of this parameter). The table convincingly demonstrates the emergent character of these open-shell molecules. High $\Delta\hat{S}^2$ values suggest a strong correlation between molecular p_z-electrons. Accordingly, bare molecules have a large number N_D of effectively

Table 1. Criterial parameters of correlation between odd p_z-electrons and magnetic constants in rectangular nanographenes [35].

(n_a, n_z) NGr	Odd electrons, N	ΔE^{RU}, kcal mol^{-1}	N_D	$\Delta\hat{S}^2$	J, kcal mol^{-1}
Bare molecules					
(5, 5)	88	307	31	15.5	−1.429
(7, 7)	150	376	52.6	26.3	−0.888
(9, 9)	228	641	76.2	38.1	−0.600
(11, 11)	322	803	97	48.5	−0.436
(15, 12)	456	1038	139	69.5	−0.324
Framed (terminated) molecules					
(5, 5)-H	66	55	14.6	7.3	−2.295
(5, 5)-OH	66	116	17.8	8.9	−2.074
(5, 5)-O	44	64	16	8	−2.079
(11, 11)-H	276	256	55.2	27.6	−0.587
(11, 11)-O	230	328	61.6	30.8	−0.528

unpaired electrons, accounting for more than one third of the total number of p_z electrons. Naturally, this number decreases with termination but remains large enough to ensure a marked radicalization of the molecules and their high chemical activity in this case as well. The data presented in Table 1 collectively illustrate the size and peripheral termination dependence of UHF emergents of graphene molecules.

The total number N_D of effectively unpaired electrons not only gives qualitative evidence of molecule radicalization but also serves as a quantitative measure of their chemical activity or *molecular chemical susceptibility* (MCS) introduced in Ref. [36]. The distribution of this number over atoms of the molecule in terms of N_{DA} is actually the *atomic chemical susceptibility* (ACS) distribution, due to which ACS–N_{DA} atomic maps provide 'chemical portraits' of the respective molecules [37]. Both MCS–N_D and ACS–N_{DA} can be regarded as new emergent 'chemical order parameters' of the open-shell molecules.

Atomic ACS–N_{DA} maps of graphene have a very specific but yet standard form. Figure 4 represents local emergents, N_{DA} and spin density, of a bare (11, 11)NGr molecule both as atomic maps and graphs. It can be seen that the graphene molecule divides into two sharply different parts as to both parameters: the peripheral zone, encompassing 46 edge atoms, and the interior (hereinafter referred to as the honeycomb) zone or the basal plane. Due to the six-fold difference between N_{DA} values in these regions, the basal plane is practically invisible in Fig. 4a, despite the large average N_{DA} value of ~ 0.2. Quantities above average values (from 0.34 to 0.22) are inherent only in the 40 atoms adjacent to edge atoms along the molecule perimeter. This atomic fraction is well apparent in the histogram (Fig. 4c) for those

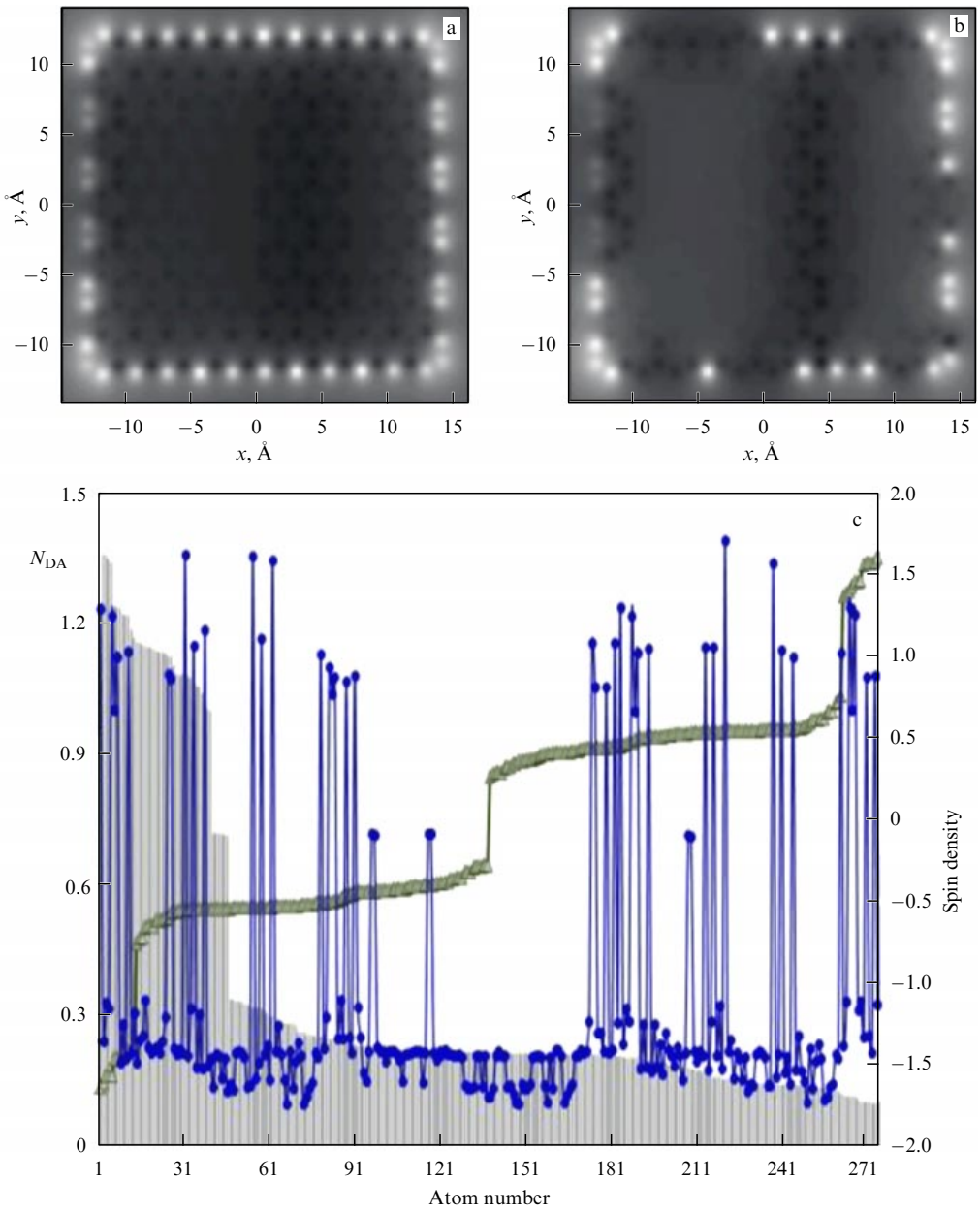

Figure 4. ACS-N_{DA} (a) and spin density (b) maps of a bare (11,1 l)NGr molecule. (c) ACS-N_{DA} depending on atom number in the output file (curve with dots); max → min N_{DA} (histogram) and spin density (curve with triangles) distribution depending on ordinal number. For the first 46 atoms, the histogram sequentially represents 22 zigzag and 24 armchair edge atoms [33].

atoms having numbers from 47 to 86. It follows from the N_{DA} histogram that the chemical activity of graphene atoms varies significantly both at the edge periphery and (to a lower degree) in the basal plane. The most intense among the 46 atoms are the 22 and 24 atoms making up zigzag and armchair edges of the molecules, respectively. N_{DA} values are 1.39–1.10 for the zigzag edges, whereas a much wider spread (from 1.22 to 0.71) is characteristic of the armchair edges.

The difference in spin density between edge and honeycomb zone atoms markedly decreases, which results in flaring the structure in the basal plane on the spin density map, as shown in Fig. 4b. Both the ACS–N_{DA} map and the absolute spin density map can be regarded as giving compelling evidence of local spins on atoms. The curves plotted in Fig. 4c give a good indication of the sources of antiferromagnetic nullification of total spin density.

The variability in electron density of carbon atoms along the edges of a graphene fragment and the adjacent honeycomb region is a common property of graphene molecules as confirmed in experiments for an arbitrary graphene fragment with unterminated edges, based on electron energy loss spectra (EELSs) with atomic resolution [38].

Figure 5 is a pictorial presentation of the state of carbon atoms in the vicinity of zigzag and armchair edges. Clearly, peculiarities depending on atom positions are localized in low-energy parts of the EELSs representing K-edges of EEL signals from carbon atoms. All these spectra show a characteristic EELS peak P_b at 285 eV related to the transition of the nuclear s-electron to the unoccupied σ^*-orbital. Additional peaks at 281 eV (P_z) and 282.8 eV (P_a) for zigzag and armchair edge atoms are due to s-electron excitation into the free p_z^*-orbital, whereas a change in the EELS profile is associated with variations in the local density of states. The peaks of edge atoms are especially well pronounced (spectrum *1*), but their intensity decreases for adjacent atoms (spectrum *2*); the peaks of carbon atoms in the basal plane practically disappear (spectra *3* and *4*). Moreover, there is an intraset difference between EELSs of zigzag and armchair edge atoms. Figure 6a shows that the difference between the spectra of two neighboring zigzag atoms *8* and *10* is so strong that peak P_z is substituted by peak P_a. A similar difference holds for the adjacent atom *9* even if with a change in intensity distribution between P_a and P_b peaks. EELSs in Fig. 6b reflect the difference in the behavior of the adjacent armchair atoms *3* and *4*, manifested as a change in the intensity ratio P_a/P_b.

The observed STEM (scanning transmission electron microscope) images are formed by all electrons of carbon atoms. The contribution from σ-electrons is virtually identical in all atoms, whereas that of p_z-electrons is essentially nonuniform. Differential signals in the form of EELSs are presented in Figs 5, 6. The observed peculiarities are in excellent agreement with the conclusions drawn from the above analysis of ACS–N_{DA} and spin density distributions in graphene molecules:

(1) electron densities of zigzag and edge atoms modified by local high-density spins are much larger than those of other atoms, but differ between themselves in favor of the former; these atoms make up the first line of defense for a graphene molecule;

(2) the second barrier is built from atoms of near-edge rows with somewhat lower but still significant spin density (see the behavior of 40 neighboring atoms in Fig. 4c); they form the transient state between edge and honeycomb atoms;

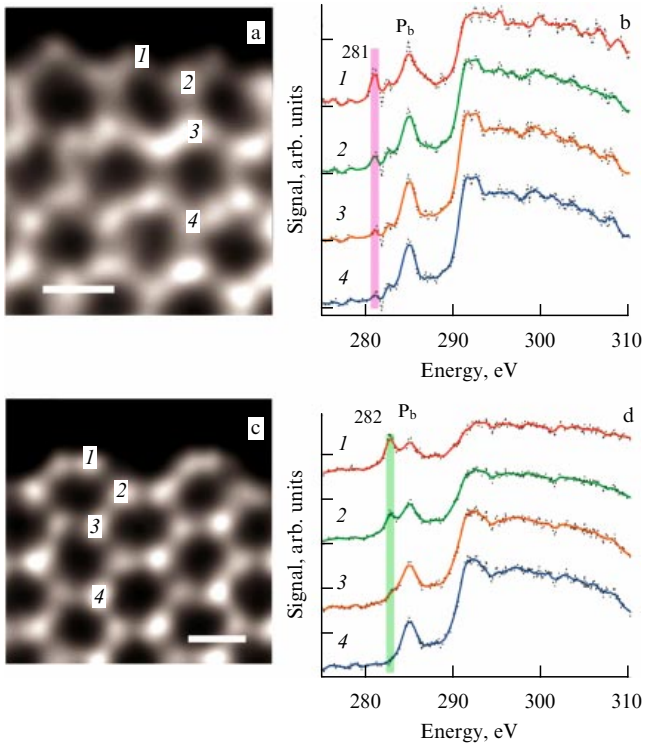

Figure 5. STEM-EELS mapping of graphene fragment edges. (a) Dark-field STEM image, and (b) EEL spectra in the region of zigzag edges from the regions corresponding to the numbers in figure (a). (c) Dark-field STEM image, and (d) EELSs in the region of armchair edges from the regions corresponding to the numbers in figure (c). Scale bars: 2 Å. Numbers in STEM images match the numbers on EELSs. (Adapted from Ref. [38]).

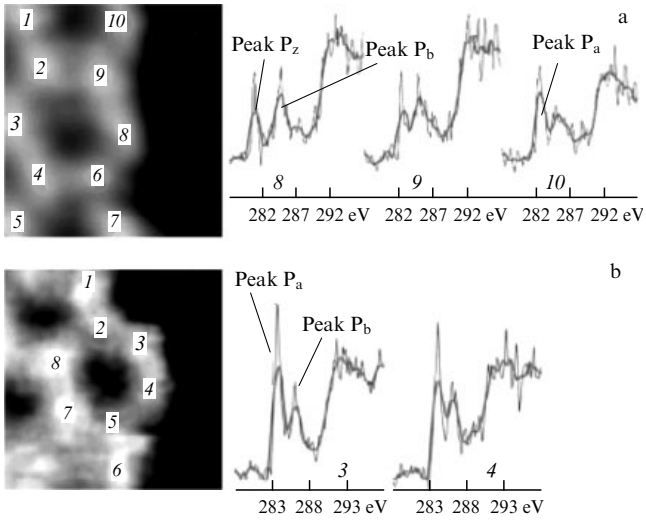

Figure 6. STEM fragments and EELSs from the edge regions of a graphene specimen for zigzag (a) and armchair (b) atoms. (Adapted from Ref. [38].)

(3) the region with the perimeter formed by these atoms contains honeycomb atoms of the basal plane; electron density is most uniformly distributed by virtue of relatively low spin density;

(4) the electron density and ACS–N_{DA} distributions inside the sets of edge, adjacent, and honeycomb atoms vary significantly, thereby demonstrating that atomic groups are

not rigorously standardized and can be highly sensitive to external impacts.

Thus, it becomes obvious that the electronic structure of a graphene molecule is characterized by an intrinsically high potential for variation. This property should be included on the list of other graphene characteristics, together with the emergent properties considered in the foregoing discussion.

The two-zone presentation of electron density of a pure graphene molecule is not news. It underlies numerous theoretical computational considerations of the role of edge atoms in graphene, dating back to 1996 [39] and continuing up to the present time (see papers [40–43] and references cited therein). In these studies, model graphene structures were largely handmade (using pencil) molecules and/or supercells of a regular honeycomb package described by standard 1.42-Å long C=C bonds both in the basal plane and at zigzag and armchair edges. The studies were designed to elucidate the spectrum of crystal's electron bands and its specific features in the Fermi level domain conditioned by the presence of edge atoms. Such features were regarded as manifestations of the special magnetic behavior of graphene flakes and/or lakes, including nanoribbons. However, the result fell short of expectations because the magnetic behavior of graphene was not directly related to the specific properties of edge atoms, as was shown in experiments and will be discussed below in Section 3. In this context, it is in order to recall a skeptical comment by R Hoffmann in his well-known article entitled"Small but strong lessons from chemistry for nanoscience" [44]:

"*There is a special problem that theory has with unterminated structures — ribbons cut off on the sides, polymers lacking ends. If passivation is not chosen as a strategy, then the radical flakes of the unterminated carbon atoms, or undercoordinated transition metals, will generate states that are roughly in the middle energetically, above filled levels, below empty levels in a typical molecule that has a substantial gap between filled and unfilled levels. If such levels — states, the physicists call them — are not identified as 'intruder' states, not really real, but arising from the artifact of termination, they may be mistaken for real states in the band gap, important electronically.... These band gap states are, of course, the origin of the reactivity of the terminated but not passivated point, line, or plane. But they have little to do with the fundamental electronic structure of the material.*"

2.4 Fundamentals of computational spin chemistry of graphene

The emergents of open-shell molecules considered in preceding sections have a direct bearing on fundamental problems of graphene chemistry. One of them is the spatially distributed region of target atoms ready to enter into a chemical reaction. Unlike the sp^2-nanocarbon era, the dawn of which was marked by the appearance of the C_{60} fullerene, molecular chemistry had to do with an active region confined to one, sometimes two–three atoms. For this reason, well-developed molecular chemistry is largely concerned with monoderivatives and far more rarely with bi- and polyderivatives. Fullerenes represent a totally new class of compounds whose activity region covers the entire molecule [18]. Carbon nanotubes and graphenes belong to the same type. Therefore, the result of any chemical attack is a polyderivative of the starting molecule, and simulation of any chemical reaction involving one of the aforementioned sp^2-nanocarbons implies the necessity to search for a descriptor

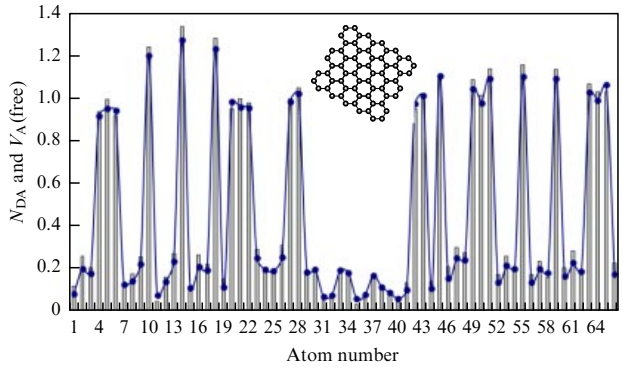

Figure 7. ACS–N_{DA} (histogram) and free valency V_A^{free} (curve with dots) for atoms of the (5, 5)NGr molecule. The inset shows the equilibrium structure of a (5, 5)NGr molecule. (Adapted from Ref. [35].)

capable of defining a sequence of events leading to the formation of the polyderivative. It turned out that in the case of sp^2-nanocarbons, the problem can be addressed at the quantitative level, with MCS–N_D and ACS–N_{DA} emergents playing the key role in its solution.

Indeed, it follows from the HF formalism that N_D and N_{DA} are unique quantitative descriptors of open-shell molecules. Thus, for molecules with an even number of electrons, N_{DA} is identical to the free valency V_A^{free} of atom A [45]. The distribution of V_A^{free} is shown in Fig. 7 by a curve with dots for a bare (5,5)NGr molecule together with ACS–N_{DA} (histogram). The figure illustrates the small difference between V_A^{free} and N_{DA} distributions. The first important conclusion following from the analysis of this distribution is that the initial stages of any chemical reaction must proceed at the periphery of the molecule with the participation of its edge atoms having the highest N_{DA} values. The second conclusion reads: the reaction will proceed till reactivity is fully satisfied after $N_D = 0$ is reached, because the reactivity region is extended in space and the formation of the first monoderivative does not inhibit the reactive capacity of the molecule. This consideration leads to the third conclusion that chemical reactions involving graphene are polyderivative reactions, i.e., they yield polyderivatives. The fourth conclusion concerns the control of chemical reactions.

The excellent agreement between N_{DA} and V_A^{free} values suggest that the former can actually serve as a quantitative measure of ACS and a quantitative descriptor of target atoms with respect to which the atom–atom contacts in addition reactions are the most preferable. Thus, ACS–N_{DA} distribution is a unique map introducing a transparent method for consecutive algorithmic computational synthesis of polyderivative graphene molecules by tracing the maximum N_{DA} value for the choice of an atom of the graphene skeleton at each stage of the reaction. The consistent application of this approach is illustrated by numerous examples of chemical modification of the C_{60} fullerene [18] or stepwise hydrogenation and oxidation of graphene molecules [19, 46, 47].

It turned out that the very first addition of a reactant or a modifier to an edge atom of a graphene molecule, chosen based on the maximum N_{DA} value, causes a marked change in the ACS–N_{DA} map of the initial molecule. However, the analysis of this map makes it possible to distinguish again the atom with maximum N_{DA} and thereby locate the second-step target atom. Analysis of the map of the second derivative reveals the location of the third-step target atom, etc. In this

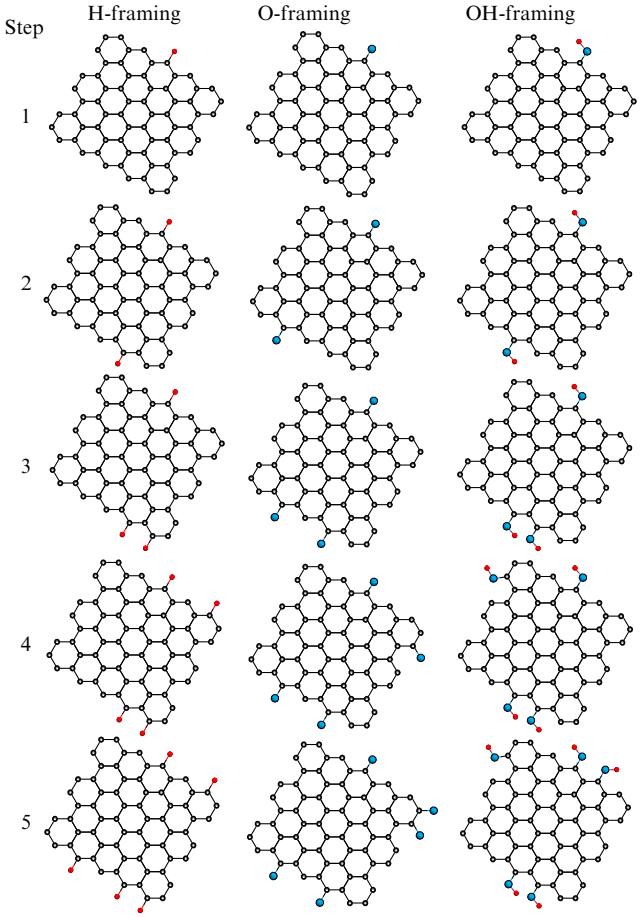

Figure 8. Equilibrium structures of polyhydrides and polyoxides of the initial (5, 5)NGr molecule corresponding to steps 1–5 of the respective chemical reactions. Grey, blue, and red balls denote carbon, oxygen, and hydrogen atoms, respectively. (Adapted from Ref. [29].)

way, a stepwise (e.g., hydrogenation, oxidation, or any other) reaction is managed to conduct.

Figure 8 presents a set of polyhydrides and polyoxides of the initial (5,5)NGr molecule obtained at the early stages of the respective stepwise reactions related to framing the initial molecule. One important conclusion suggested by Fig. 8 is that, despite the seemingly local change in the molecular structure caused by the first addition, the second target carbon atom does not match the corresponding atom that was ranked second in terms of size on the initial list of N_{DA} for pure molecules. Also, the location of this atom and the sequence of the next steps vary, depending on the chemical nature of the involved reactant. These two features reflect redistribution of C = C bond lengths over the molecule and thereby reveal the collective action of its effectively unpaired electrons, as well as the nonlocal character of each chemical addition act. It is appropriate to recall the characteristic of emergentness of the electron system as a manifestation of a collective effect irreducible adiabatically to a system of free electrons [1].

Taken together, the polyderivative character of chemical transformations of graphene, delocalization of its structural response to each local change of $sp^2 \rightarrow sp^3$ hybridization, and the resulting redistribution of C = C lengths accompanied by variations in N_{DA} distribution lead to important consequences that significantly complicate spin-dependent graphene chemistry [19]. An example is presented in Fig. 9

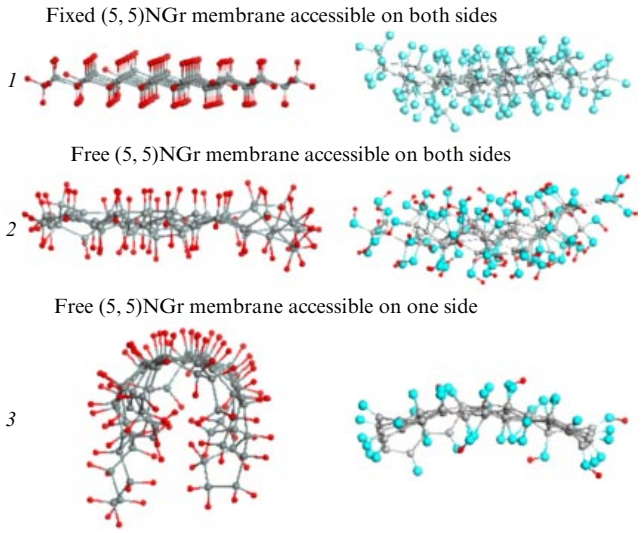

Figure 9. (Color online.) Equilibrium structures of saturated polyderivatives of the (5, 5)NGr molecule: graphene hydrides (left column) and graphene oxides (right column) (see text). Grey, blue, and red balls mark carbon, oxygen, and hydrogen atoms, respectively. Graphene oxides differ not only in the state of the graphene membrane, but also in reactants: *1* — atomic oxygen, *2* — hydroxyls, and *3* — atomic oxygen + hydroxyls mixture. (Adapted from Ref. [19].)

showing equilibrium structures corresponding to the completed cycles of stepwise hydrogenation and oxidation of (5,5)NGr molecules. Clearly, the structure and chemical composition of the product of graphene chemical modification depend on a variety of factors, viz. graphene membrane molecule location in space (free or fixed), its accessibility to a reactant on one or both sides, not mentioning the composition of the reactant itself, etc. The leading role of 'chemical' emergents, N_D and N_{DA}, in the quantitative solution to this problem can hardly be overestimated.

Results of quantum-chemical (QC) calculations are in excellent agreement with experiment. For example, graphene membranes were successfully hydrogenated in experiments [48] (see cases *1* and *2* in Fig. 9). In case *1*, an ordered crystalline structure corresponding to a graphane model [49] was obtained; in case *2*, an amorphous structure was produced. (A detailed description of computational graphene hydrogenation can be found in Refs [19, 46]). Experimental data on graphene oxides suggest the existence of a large class of products under this name differing in reagent composition and mode of membrane fixation [50]. Nevertheless, all structural studies reveal only amorphous substances. The search for regular crystalline structures has been unsuccessful.

Investigations into graphene physics encounter such great difficulties unfolding against the background of complex chemical patterns of these materials that it is opportune to speak about the conflict between graphene chemistry and physics [29]. This issue will be discussed in Section 2.8. Now, we shall consider the emergentness of graphene from the physical standpoint with reference to such characteristic emergent properties as magnetism and superconductivity [1–5].

2.5 Nonrelativistic and relativistic UHF formalism

It was shown above that spin symmetry breaking is closely related to the correlation between electrons, leading to spin

mixing apparent as spin contamination $\Delta\hat{S}^2$. However, vectorial spin-orbit coupling (SOC) E^{SO} also mixes spin states, which brings up the central problem of modern quantum chemistry covering the relationship between electron correlation and spin-orbit effects. It is time to remember the accurate commentary by W Liu [51] concerning the topic: "*Only the combination of both relativity theory and correlation can precisely match experiments that are, without exception, fully relativistic and correlated.*" It is important to note another statement by W Liu that correlation is fully described by parametrized RSD (restricted single determinant) wave functions by using a particular method, while relativity shows up in Hamiltonian. The development of nonrelativistic and relativistic quantum chemistry during the last decade [52, 53] fully confirms the validity of this assertion.

Implementation of the first program resulted in the creation of a large number of nonrelativistic (NR) methods suitable for considering configuration interaction (CI). The generalized Hartree–Fock (GHF) approximation [12] is one of the areas of this development, while the UHF formalism is one of the best GHF realizations [54]. Implementation of the second program involves the relativistic Dirac equation and possible simplifications of its Hamiltonian. At present, there is a wide spectrum of relativistic Hamiltonians, including SOC, due to the efforts of many quantum chemistry groups. The issue is extensively discussed in Refs [52, 53, 55]. Many of these Hamiltonians serve as seamless bridges between the Schrödinger and Dirac equations, which affords grounds to argue that the relativity problem in chemistry has been solved [53]. Certainly, a number of special problems remain to be solved, but the common house of relativistic quantum chemistry (RQC) is built on a solid foundation.

To clarify the situation with regard to open-shell molecules, we shall consider nonrelativistic (NRQC) and RQC approaches on the platform of UHF approximation. In the Hartree–Fock method, the ith wave function is substituted by a one-electron molecular spinor with two components (2c-relativistic HF approximation). Accordingly, the wave function expressed in unrestricted HF formalism as

$$\psi_i = \begin{pmatrix} \psi_i^{\alpha} \\ \psi_i^{\beta} \end{pmatrix} \tag{1}$$

assumes in the relativistic approximation the form

$$\psi_i^{+} = \sum_p c_{ip\alpha}^{+} \chi_p \alpha + \sum_p c_{ip\beta}^{+} \chi_p \beta\,, \tag{2}$$

$$\psi_i^{-} = \sum_p c_{ip\alpha}^{-} \chi_p \alpha + \sum_p c_{ip\beta}^{-} \chi_p \beta\,. \tag{3}$$

Here, α and β label spin functions, while χ_p represents the spatial basis function. Equations (2) and (3) define the Kramers pair of spinors. When spinors ψ_i^{+} and ψ_i^{-} are symmetric with respect to time-reversal (by analogy with spin symmetry of functions ψ_i^{α} and ψ_i^{β} in the case of RHF), the relativistic HF method for many-atom molecules is the two-component (2c) Kramers restricted Hartree–Fock (KRHF) approximation [56]. In the case of broken time-reversal symmetry, the spinor pair [Eqns (2) and (3)] defines the 2c Kramers unrestricted Hartree–Fock (KUHF) method [56, 57]. KUHF spinors are called degenerate Kramers pairs in analogy with functions ψ_i^{α} and ψ_i^{β} of the UHF approximation [58]. Given that SOC is neglected, it can be expected that the solutions provided by UHF and KUHF algorithms should be identical.

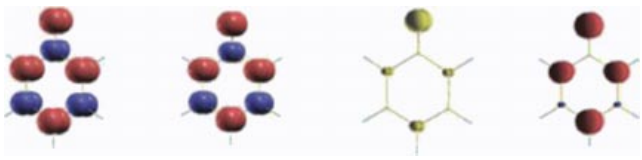

Figure 10. Spin density distribution over phenoxyl radical (C_4H_5O) atoms calculated in different approximations [58] (by courtesy of L Bučinský).

Two-component spinors (2) and (3) fairly well perform the role of basic sets of the generalized complex Hartree–Fock (GCHF) approximation [54]. It was shown in the framework of this approximation based on Kramers pairs that upon application of its unrestricted formalism to open-shell molecules the Kramers pair degeneracy can be characterized by a parameter identical to spin contamination $\Delta\hat{S}^2$ in the UHF approximation [58]. For example, the KUHF approximation was employed together with UHF to consider the phenoxyl radical C_6H_5O.The two methods gave evidences that the molecule is identified as open-shelled, while both $\Delta\hat{S}^2$ and its relativistic analog are equal to 0.6024. The similarity of the results gives evidence that SOC in the molecule of interest is negligibly small, and spin contamination in both cases is due only to electron correlation. This observation holds not only for spin contamination $\Delta\hat{S}^2$ but also for the spin structure. Indeed, the correlation-stimulated contribution from determinants with higher multiplicity and different $\langle\hat{S}^2\rangle$ values but identical expected $\langle\hat{S}_z\rangle$ influences the spatial spin density distribution, giving rise to additional positive and negative density regions, but does not affect the total population of S_z spins. It is this effect that accounts for the presence of spin density and/or local spins in graphene molecules, discussed in the preceding sections (see Figs 3, 4).

Figure 10 demonstrates the spin density distribution of a C_6H_5O molecule co-linear with the magnetic field and calculated in the framework of different approximations of the theory [58]. It follows that the results obtained with the applications of the UHF and KUHF approximations are perfectly identical but strikingly different from those obtained in the restricted approximation for open-shell molecules (ROHF), and in the unrestricted approximation of the density functional theory (UDFT). This means that the subdivision of molecules into two groups in terms of the state of their electron shells, first introduced in NRQC, is retained in RQC, too, as a result of quantum phase transition preventing restoration of continuous symmetry.

2.6 Relativistic electrons of a graphene crystal

The close relationship between UHF emergent phenomena in graphene molecules (KUHF emergents are pending discussion) and C = C bond length distribution is quite apparent in the mechanochemical and topochemical behavior of these molecules, confirmed in numerous experiments (see Section 4 and book [19] with references cited therein). Taken as a whole and nominated as spin peculiarities, the chemical behavior of graphene molecules gives convincing evidence of broken spin symmetry of electronic states in this substance, prompting an evaluation of graphene's physical properties from the same standpoint. However, solid-state many-electron approximations used to calculate graphene crystals were previously proposed for graphite and actually intended for the elucidation of its electronic band spectrum. They were developed

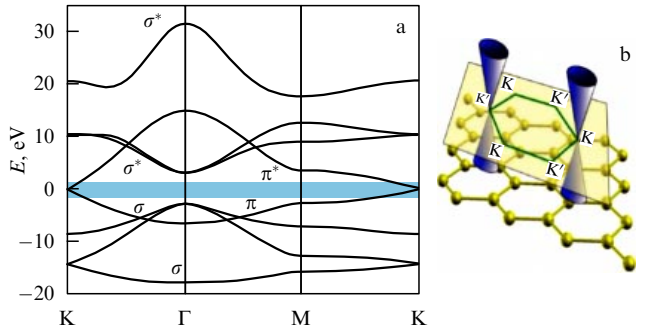

Figure 11. (a) Common view of a graphene band structure. The Fermi level is set to zero. Strips below (above) the Fermi level are related to valence (conduction) bands. (b) Two pairs of valence (conduction) Dirac cones adjoining at the Fermi level at points K and K′.

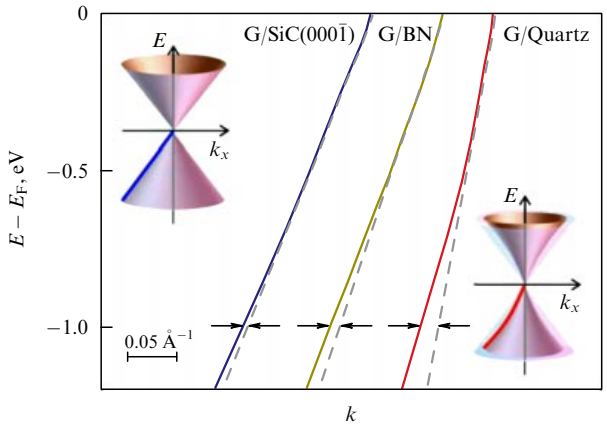

Figure 12. Experimental dependences $E_2(k_0 + k)$ for graphene on SiC(000$\bar{1}$), BN, and quartz substrates. Insets illustrate changes in Dirac cones in graphene upon transition from weak (left) to strong (right) interactions with the substrate [65].

outside the framework of the HF formalism, mostly in terms of the simpler tight binding (TB) approximation for neighboring atoms [59, 60]. These calculations showed that the low-energy part of the band spectrum of a graphene crystal is identical to the Dirac spectrum for massless fermions, obtained in the framework of the quasirelativistic approximation [61]. Such an approach required new terms, such as Dirac fermions and Dirac cones, that turned graphene physics into quasirelativistic physics from the very beginning.

The standard approximation for describing the electronic band spectrum of graphene disregards both SOC and correlation of its odd p_z-electrons and thereby supports continuous symmetry conservation by analogy with the RHF approximation for molecules. The spectrum has a standard shape of adjoining Dirac cones at selected points of the Brillouin zone, the position of which is determined by spatial symmetry. The consideration is based on the fact that a crystal primitive cell is very simple and contains two atoms. At the same time, the cells are packed in a hexagonal configuration that, on the one hand, corresponds to the honeycomb structure and, on the other hand, ensures the flat and hexagonal configuration of the first Brillouin zone. A characteristic feature of the Brillouin zone structure is two nonequivalent sets of points, each including three K and K′ type vertices, respectively. The reference point in the wave vector space at point Γ is located in the center of the hexagon.

Typical of the TB approximation is separation of the electronic Hamiltonian into two parts related to π- (odd p_z-) and σ-electrons, respectively. In this approximation, the complete band structure of a graphene crystal has the characteristic shape illustrated in Fig. 11a. Because reference to relativistic analogy usually concerns π-bands [60], the authors used to confine themselves to considering only this part of the spectrum. The corresponding low-energy states of quasi-particles at the Fermi level denoted by the darkened strip in Fig. 11a make up six pairs of adjoining cones with vertices at K (K′) (two pairs are shown in Fig. 11b).

The complete low-energy electronic spectrum of graphene in the region of six pairs was described in paper [60] as

$$E_1(k_0 + k) = E^0 - \left(\frac{\eta p_0}{m}\right) k\,,$$

$$E_2(k_0 + k) = E^0 + \left(\frac{\eta p_0}{m}\right) k\,. \qquad (4)$$

Here, E^0 and k_0 are the Fermi energy and wave vector of the quasiparticle at points K (K′). E_1 and E_2 spectra are related to the conduction and valence bands, respectively. A detailed description of parameter $\eta p_0/m$ is presented in paper [60]. Equations (4) are analogous to equations for Dirac massless fermions; therefore, the low-energy part of the quasiparticle spectrum in the immediate vicinity of points K (K′) (hereinafter, Dirac points) can be formally described by a Hamiltonian similar to the Dirac-like Hamiltonian:

$$\hat{H} = \eta v_F \begin{pmatrix} 0 & k_x - \mathrm{i}k_y \\ k_x + \mathrm{i}k_y & 0 \end{pmatrix} = \eta v_F \boldsymbol{\sigma}\mathbf{k}\,, \qquad (5)$$

where $\mathbf{k}$ is the quasiparticle wave vector, and $\boldsymbol{\sigma}$ is the two-dimensional Pauli matrix for spins; the k-dependent Fermi velocity v_F plays the role of the speed of light. Equation (5) is a direct consequence of the spatial symmetry of the graphene crystal comprising a honeycomb hexagonal lattice [61]. This specific band structure gave graphene the name *Dirac material* that thus far remains a 'solid-state toy' for relativistic quantum mechanics [62–64].

Because Dirac fermions move at Fermi velocity $v_F \sim 10^6$ m s^{-1}, much lower than the speed of light (which accounts for the small v_F/c ratio), it is possible to imitate and observe in table-top experiments at lower energies those quantum relativistic phenomena that are difficult or impossible to see in high-energy physics. At the same time, excellent agreement between predicted and experimental findings allows Dirac fermions in graphene to be regarded as a physical reality. Concrete engineering tools have been proposed for their management by modulating Fermi velocity. The proposal was implemented experimentally by placing graphene on different substrates [65]. Figure 12 indicates that substituting quartz for an SiC (000$\bar{1}$) substrate results in a two-fold change in v_F, from 1.15×10^6 to 2.46×10^6 m s^{-1}. The presented electronic spectrum of graphene crystal shows for the moment no emergent phenomena.

2.7 Characteristic features of Dirac cone spectra

As was mentioned in the foregoing, Dirac cones in the band spectrum of a crystal represent a specific effect of its spatial symmetry characteristic of any flat (even quasiflat)

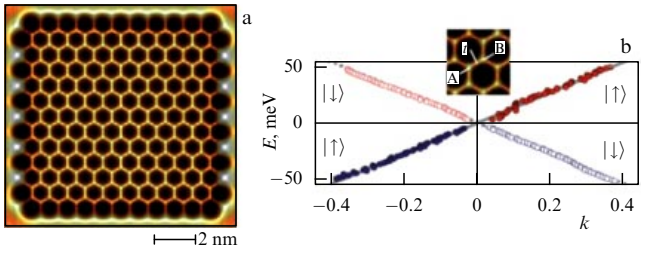

Figure 13. 'Molecular graphene'. (a). Topography at a constant current of a graphene-like lattice consisting of 1549 carbon monoxide (CO) molecules. (b) Linearly dependent conductivity spectra of sublattice A (dots: pseudospin $S_z = +1/2$) and sublattice B (open circles: pseudospin $S_z = -1/2$) measured at t (shown in the inset). (Adapted from Ref. [69].)

atomic hexagonal configurations, similar to the honeycomb lattice responsible, in turn, for the hexagonal structure of the Brillouin zone. Indeed, the behavior of electronic states is reminiscent of the Dirac fermion spectrum for silicon atom monolayers on the Ag(111) surface (arbitrarily associated with a new substance called 'silicene') [66]. A detailed discussion of the reality and virtuality of silicene can be found in Ref. [67]. A similar behavior was predicted for crystals of other monatomic tetrels composed of group 14 elements of the Periodic Table, germanene and stanene [68].

However, Dirac cones occur not only in monatomic structures. Specifically, a new class of artificial 'molecular graphenes' appeared with a honeycomb structure built from different atoms or molecular groups. One of the first structures of this type was obtained by deposition of carbon monoxide molecules onto a Cu(111) surface [69]. A topographic image of a flake of molecular graphene is presented in Fig. 13a. It demonstrates the perfectly ordered internal honeycomb lattice and edge effects at the boundaries, analogous to those in graphene (cf. Fig. 3a). Despite the finite size of this structure, the cone-shaped conductivity spectra (Fig. 13b) suggest the presence of Dirac cones in the energy band structure near the Fermi level. It was shown that these structures exhibit a stable crystal-like behavior, given that the size of the 'crystal' is 20 nm or more.

There is an impressive amount of purely theoretical research on 'molecular graphenes' having band spectra reminiscent of the Dirac graphene spectrum. They encompass virtual silicene, germanene, and stanene crystals (see paper [70] and references cited therein), hydrogenated borophene [71], arsenene, and antimonene [72]. These Dirac materials are described by the hexagonal package of biatomic primitive cells. Quite recently, experimental preparation of hexagonal borophene [73] and antimonene [74] has been reported. However, the 'primitive cell' can have a much more complicated structure, as is the case with s-triazine primitive cells composed of C_6N_6, $C_{12}N_6$, or $C_{24}N_6H_{12}$ molecular compositions [75], graphitic carbon nitride (GCN) with $C_{14}N_{10}$ as a primitive cell [76], and the beautiful hexagonal lace of $NiC_8S_2H_4$ molecules [77]. FeB_2 monolayers with a graphene-like boron sheet [78] and a large set of 2D early transition metal carbides (MXenes) [79] (see review [80] and references cited therein) further extend the list of substances with Dirac cones whose existence is due to hexagonally packed primitive cells. The last to be obtained were zirconium telluride $ZrTe_2$ [81] and gallene (adsorbed gallium monatomic layers) [82].

The wide assortment of structures having cone-shaped electronic spectra near the Fermi level stimulated the development of an algorithm for the search for 2D graphene-like compounds among the innumerable number of organic and inorganic substances. The work proved successful, and the proposed algorithm [83] made possible thorough structural analysis of 100,000 bulk materials, making use of information from external databases. At first, the search was reduced to 5600 potential 2D materials, then 1800 structures tending to be exfoliated were chosen, including 1036 with especially weak interlayer couplings. Finally, the 258 most promising candidates were selected based on their magnetic, electrical, mechanical, thermal, and topological characteristics. This unprecedented crystallographic physicochemical study has demonstrated the unique role of graphene as a stimulating factor.

Practically all the considered Dirac spectra of 'molecular graphenes' were calculated with the use of restricted computational formalisms taking no account of whether the systems of interest had open or closed electron shells, with the exception of calculations for GCN $C_{14}N_{10}$ crystals [76] and the metalorganic lace-like skeleton with a $Ni_2C_{24}S_6H_{12}$ primitive cell [77], in which the correlation among electrons with different spins was taken into consideration. This approach immediately revealed splitting or spin polarization of electronic spectra, resulting in a doubling of the number of bands and their possible uniting in the form of sets α and β, as is well apparent for GCN and the aforementioned lace skeleton in Fig. 14. Configurations of the respective primitive cells are shown under the spectra. Both primitive cells contain an even number of valence electrons, which accounts for the absence of free spins as a result of zero total spin density. The authors do not associate the observed effect with emergentness of the electronic structures, attributing the observed spectrum splitting to the reduction in numerical characteristics of antibonding with respect to chemical bonds responsible for the appearance of a peculiarity in the density of states at the Fermi level [76]. At the same time, the data obtained show that both cells have open-shell electronic systems due to correlation between odd electrons, leading to spin symmetry breaking and splitting of electronic bands as a manifestation of emergentness of these systems. Indeed, the UHF analysis of a $C_{14}N_{10}H_4$ molecule ideally imitating the GCN primitive cell (Fig. 14e) suggests its open-shell nature with the total number of effectively unpaired electrons $N_D = 5.34$, which are distributed over nitrogen and carbon atoms with average N_{DA} values of 0.285 ± 0.001 and 0.145 ± 0.003, respectively (Fig. 14f) [19].

The spin-polarized split band structure of crystals of the graphitic nitride carbon and the metalorganic lace skeleton shown in Fig. 14 represents the first emergent stimulated by spin symmetry breaking and belonging to band spectra of two-dimensional solids. It follows from Fig. 14 that spin splitting is fairly well manifested in a wide range of both Brillouin zones. However, Dirac spectra remain gapless at points K (see inset to Fig. 14a). Evidently, this feature relates to the hexagonal packing of molecules and is stable with respect to the emergent in question.

The calculation of band emergents of the graphene crystal is still a long way off. Nevertheless, the reality of spin splitting of graphene energy levels gives hope that such emergents will be found. Figure 15 presents the energy spectrum of a set of spin-orbitals of the (5,5)NGr molecule [84]. A comparison between results of RHF and UHF calculations suggests its

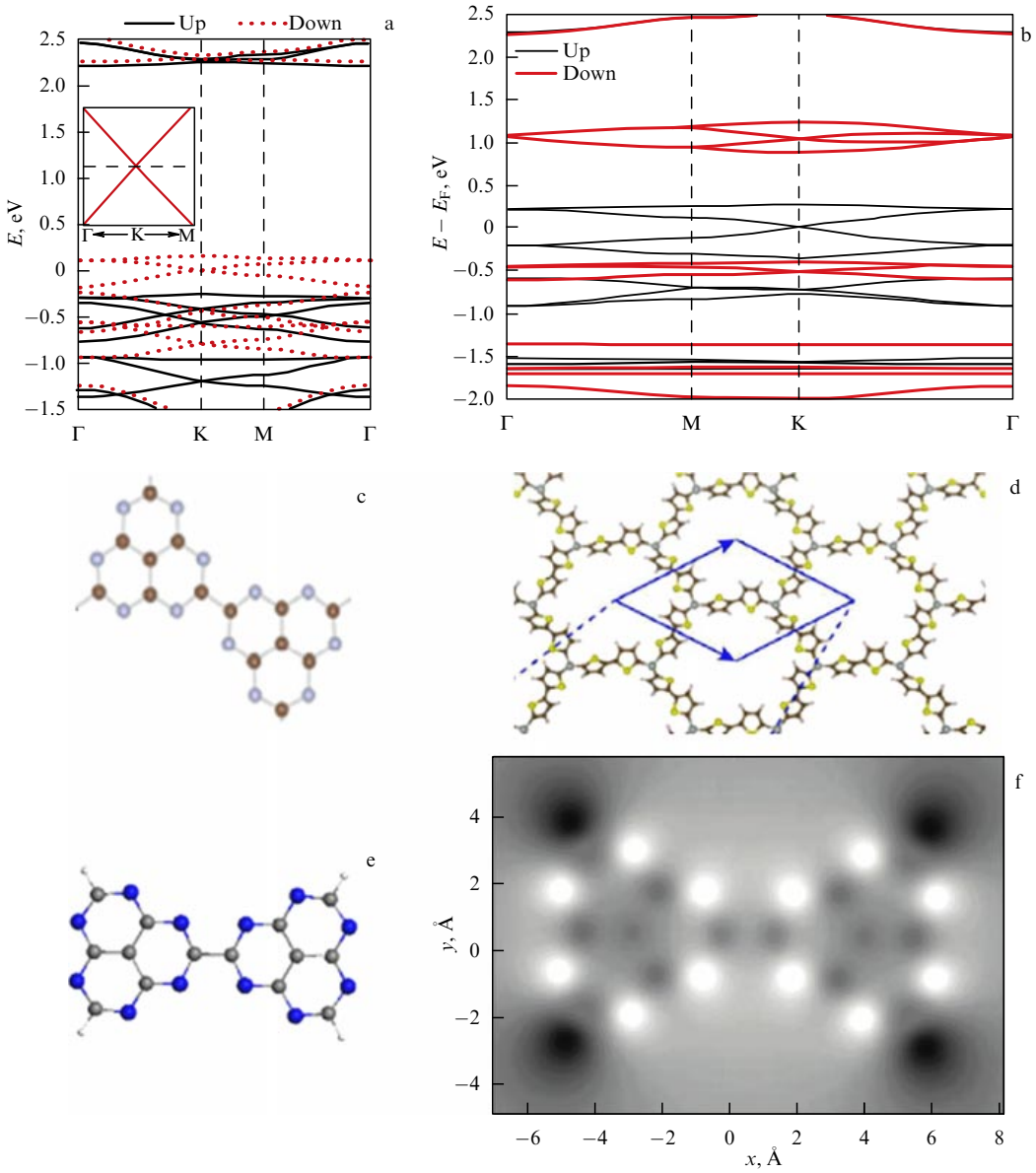

Figure 14. Split (spin-polarized) band structure (a, b) and primitive cell (c, d) of a GCN $C_{14}N_{10}$ crystal and $Ni_2C_{24}S_6H_{12}$ lace skeleton, respectively. (Adapted from Refs [76, 77].) Equilibrium structure (e) and ACS–N_{DA} map of local spin distribution (f) of a $C_{14}N_{10}H_4$ molecule. (Adapted from Ref. [19].)

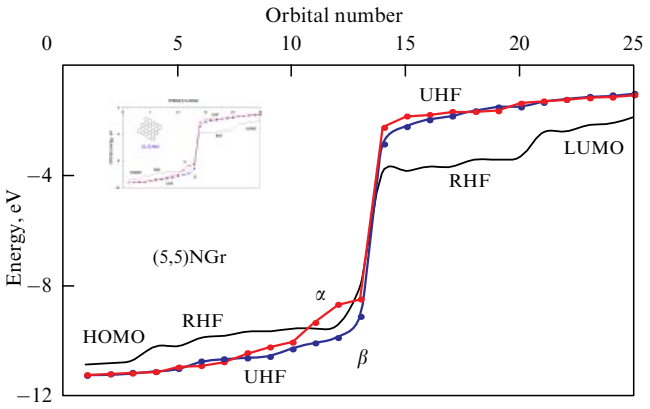

Figure 15. Energies of 25 spin-orbitals in the vicinity of the HOMO–LUMO gap of a bare (5, 5)NGr molecule (HOMO — highest occupied molecular orbital, and LUMO — lowest unoccupied molecular orbital). (Adapted from Ref. [84].)

spin-polarization as a consequence of correlation effects. Degeneracy of RHF solutions is due to both high spatial (D_{2h}) and spin symmetries of the molecule. Figure 15 shows that a passage from RHF to UHF divides orbitals into two well-differentiated families belonging to α and β spins. The character of splitting differs for two orbitals within a range between 0.02 and 1.12 eV, which determines the scope of values expected for the splitting of graphene crystal band states due to a spin symmetry breaking.

2.8 Dirac fermions and topological nontriviality of graphene

As shown in Section 2.7, the above spin polarization does not remove the Dirac cone degeneracy at Dirac points. A thorough study has demonstrated that the gapless spectrum structure can be broken only by taking account of SOC [61]. At the same time, intrinsic SOC of light-atom graphene is known to be insignificant, which makes unlikely the appearance of an energy gap in the region of its Dirac cones.

However, well-apparent electron correlation in graphene can generate dynamic SOC (see paper [85] and references cited therein). This makes possible relativistic effects owing to strong electron correlation despite insignificant intrinsic SOC. The former effect relates to the gap opening in the Dirac spectrum. A team of researchers headed by K Novoselov and A Geim checked for the presence of the gap to learn how closely it is possible to approach the Dirac point in experiment [86]. It was shown that the error in measuring energy δE depends on many external factors, such as sample quality and homogeneity, resolving power of measuring devices, and temperature. The best δE value obtained for a free sample was ~ 1 meV at 4 K, which means that there is no bandgap in graphene larger than 0.5 meV and that the overall SOC effect is below this level. Nevertheless, it does not disprove the existence of SOC itself, which may be of significance in the case of other effects more sensitive to weak SOC. One such effect relates to the topological nontriviality of graphene.

Electron correlation and SOC are key characteristics of topological nontriviality in 2D solids. It became clear after the Dirac topological insulator (TI) had been discovered [87]. In the case of graphene, the insignificance of vectorial SOC and disregard of electron correlations in calculations performed on a restricted basis were serious obstacles to the discussion of this issue. However, topological nontriviality encompasses a variety of topological states and phases whose existence is determined by the relationship between correlation effects and SOC.

Figure 16 presents a phase diagram of topological states characteristic of a 2D graphene-like honeycomb structure, known as the Kane–Mele model [61], in relative correlation energy coordinates (U) and SOC (λ_{SO}) used in the Habbard model [85]. The figure indicates that in the limiting case ($\lambda_{SO} = 0$) and depending on correlation energy, the above 2D structures can be regarded as semimetals (SMs), quantum spin liquids (QSLs), and antiferromagnetic Mott insulators (AFMIs) with the Heisenberg order (xyz). At the same time, SOC increasing transforms solid state SM and QSL into a QSHI (quantum spin Hall insulator) in a wide range of correlation energy variation. When energy U reaches critical values shown by the solid line, the QSHI transforms into an AFMI with an easy plane order (xy). In the limiting case, $U = 0$, the solid should behave like a QSHI at all λ_{SO}.

The estimated value of parameter U/t for graphene is 1.6 [88], which allows placing graphene well below the boundary with QSL and AFM phases and including it among semimetals at $\lambda_{SO} = 0$. However, the indisputable correlation of p_z-electrons in graphene inevitably causes degeneracy of Kramers pairs of the respective spinors [56], which breaks time-reversal symmetry and stimulates the formation of dynamic SOC [85]. As a result, nonzero λ_{SO}/t values shift graphene into the depth of the QSHI phase and thereby ensure its explicit topological nontriviality. Energy gap splitting between Dirac cones is not the sole manifestation of such nontriviality; it is also evidenced by such peculiar properties of matter as magnetism and conductivity.

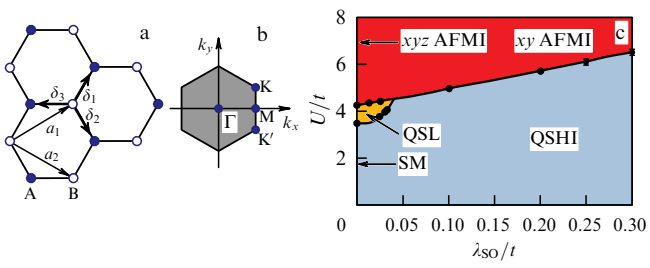

Figure 16. (a) Kane–Mele model of honeycomb lattice consisting of two sublattices A and B. (b) Hexagonal first Brillouin zone contains two nonequivalent Dirac points K and K′. (c) Phase diagram of Kane–Mele–Hubbard model at half filling calculated by the Monte Carlo method. (Adapted from Ref. [85].)

It can be reasonably supposed, with reference to symmetry concepts of emergent physics [1–5], that magnetism and superconductivity, on the one hand, and topological nontriviality, on the other hand, should be ranked among emergent phenomena. However, this aspect of graphene physics remains virtually unexplored, even if problems related to continuous symmetry breaking have been considered in Refs [89, 90]. It appears that the limited character of the TB formalism used in the overwhelming majority of theoretical studies can be a factor slowing down the development of such research. At the same time, the emergent phenomena documented thus far in graphene chemistry are in themselves convincing evidence that events of this type must be just as well inherent in graphene physics. We shall try to confirm these expectations by analyzing the magnetic and superconducting behavior of graphene and its response to mechanical impacts considered in Sections 3 and 4. The said phenomena provide a very clear illustration of the common basis of chemical (molecular) and physical (crystalline) emergents of graphene.

2.9 Comments on graphene conversion from a semimetal to a semiconductor

The detailed consideration of graphene emergent physics should be preceded by the discussion of one more aspect of great importance in the context of high-performance utilization of graphene crystals. Notwithstanding their numerous extraordinary properties and enormous potential for various applications, the exploitation of graphene as an electronic material is hampered by the lack of a sizable bandgap. Graphene is essentially a gapless QSHI, but most researchers treat it as a semimetal. This significantly limits many graphene applications, where semiconducting materials with a suitable bandgap are required. A great deal of effort was made to develop efficient methods for obtaining semiconducting graphenes and generating a proper bandgap. Nevertheless, the production of such materials still encounters great difficulties. Their detailed description with the analysis of the related problems and proposals for their solution are included in review [91]. Let us address this problem, bearing in mind major traps and pitfalls ensuing from the emergent character of graphene chemistry.

Classification of methods needed to produce superconducting graphenes yielded three main groups of techniques: (1) morphological patterning of graphene sheets into nanoribbons, nanomeshes, or quantum dots to induce quantum confinement and edge effects; (2) chemical modification, doping or surface functionalization to intentionally interrupt connectivity of the π (p_z)-electron network, and (3) other methods, e.g., use of Bernal stacking bilayers (AB stacking) to break lattice symmetry and import mechanical deformation or strain to graphene (see schematic representation in Fig. 17). Methods of the first group are intended to solve problems concerning the basic edge property of the graphene molecule, which is obviously the dangling bond effect. Indeed, cutting

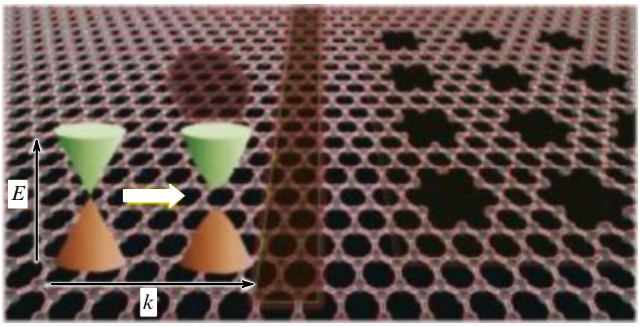

Figure 17. Schematic view of morphological patterning of a graphene sheet. (Adapted from Ref. [91].)

graphene sheets into nanoribbons increases the number of dangling bonds and consequently the number of effectively unpaired electrons N_D, thus enhancing the ribbon's radical properties. In turn, extra radicalization greatly promotes various chemical reactions in the ribbon circumference, which sometimes leads to drastic reorganization of the pristine graphene structure. Insertion of nanoholes has an analogous effect due to the highly active periphery of the formed holes. Deposition of nano-sized quantum dots markedly disturbs the graphene substrate structure, changing the C = C bond length distribution and thus causing N_D growth, even if this is not done by its own effectively unpaired electrons. Therefore, cutting and drilling create a serious 'edge problem' and do not seem to be adequate technologies for the desired transformation in the graphene electron system.

The chemical modification of graphene not only is a subject of interesting chemistry but has been many times suggested as an efficient tool for the semimetal–semiconductor transformation needed for high-performance electronics [16]. It should be noted that the suggestions are mainly based on results of computational studies that concern pencil-drawn pictures of graphene fragments, including various chemical modifiers arbitrarily chosen and artificially spread over graphene sheets (see, for example, Refs [92, 93]). These and many other virtual structures, regularly distributed in space by using periodic boundary conditions, exhibit electronic properties that are so badly needed for applications. However, the empirical reality is much less promising, since the number of regularly chemically modified graphene structures known thus far is negligible, and the collective behavior of unpaired electrons underlying graphene emergentness and suppressing its local response to any external impact is the main cause of the failure. Beyond that point, it was shown in Section 2.3 that reactions at the periphery of a graphene sheet/ribbon/molecule always precede those in the basal plane. Moreover, the latter cannot begin until the former are terminated. In the overwhelming majority of studied cases, the completion of peripheral reactions implies termination of the framing of graphene molecules/sheets.

A thorough study of circumference reactions has disclosed a very exciting feature: the framing of graphene molecule leads to cracking of the initial sample. Figure 18 presents a set of ACS–N_{DA} maps showing NGr molecules of various sizes terminated with single hydrogen atoms (H1 end atoms). ACS maps of all the pristine bare molecules have an identical pattern characteristic of the (11, 11)NGr molecule shown in Fig. 4 but scaled according to the molecular size.

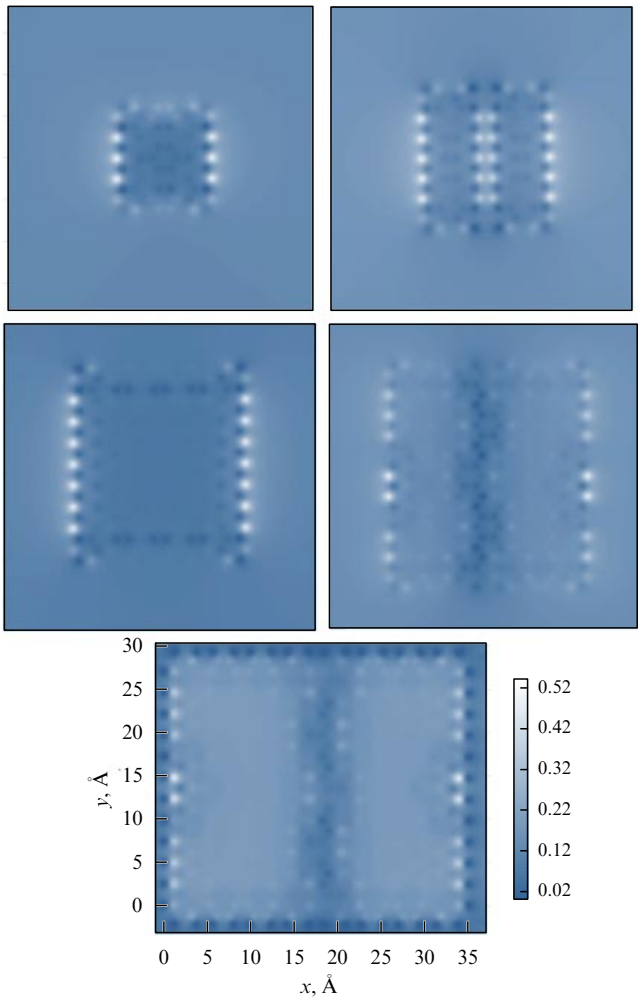

Figure 18. ACS–N_{DA} maps of (5, 5)NGr, (7, 7)NGr, (9, 9)NGr, (11, 11)NGr, and (15, 12)NGr molecules with the ends terminated by single hydrogen atoms. Spatial and N_{DA} (see at the bottom panel) scales are identical. (Adapted from Ref. [19].)

As seen in the figure, the ACS maps reveal a tendency of H1-terminated polyderivatives toward a peculiar two-part division affecting (15, 12)NGR (3.275 × 2.957 nm) and (11, 11)NGr (2.698 × 2.404 nm) molecules, in contrast to the maps of (9, 9)NGr (1.994 × 2.214 nm), (7, 7)NGr (1.574 × 1.721 nm), and (5, 5)NGr (1.121 × 1.219 nm) molecules. Apparently, the finding demonstrates the ability of graphene molecules to be divided, when their linear size exceeds 1–2 nm. The cracking of pristine graphene sheets in the course of chemical reactions has been observed in many experiments. A peculiar size effect was shown to occur in graphene oxidation [94] and fluorination [95]. During 900 s of continuous oxidation, a micrometer graphene sheet transformed into a set of ~ 1-nm pieces of graphene oxide. Obviously, the cracking rate depends on concrete reaction conditions (main and auxiliary reactants, solvents, temperature, and so forth) (see Refs [96, 97]). Cracking can probably be avoided in certain cases, e.g., when the conditions of the inhibition of edge atom reactivity allow. However, the tendency toward cracking arising from the intrinsic correlation of odd p_z-electrons is a direct threat to the stability and integrity of the final product.

Cracking is not observed in some instances if graphene specimens are membranes fixed over a perimeter on solid

substrates. Then, the reactivity of peripheral membrane atoms is inhibited and the basal plane becomes the main battlefield for chemical modification. Nevertheless, ACS retains its role as a pointer of the target carbon atoms for the sequence of reaction steps, as in the case of peripheral reactions considered earlier. However, the situation is much more complicated from the structural viewpoint. The addition of any modifier to the carbon atom in the basal plane is accompanied by the $sp^2 \rightarrow sp^3$ transformation of valence electron hybridization, so that for regularly packed chemical derivatives the benzenoid skeleton of pristine graphene should be substituted by the cyclohexanoid one corresponding to the polyderivatives formed. When benzene molecules and, consequently, benzenoid cycles are monomorphic, cyclohexanes (and, therefore, cyclohexanoid units) are highly heteromorphic.

The insignificant difference in the free energy of conformers allows the co-existence of cyclohexanoids with different structures, thus making the formation of a regular structure a rare event. For example, the regular crystalline structure of graphene polyhydride, known as graphane (see Fig. 9), was obtained in experiment under specific conditions when fixed graphene membranes were accessible for hydrogenation by hydrogen atoms from both sides [48]. In the same experiment, fixed membranes (ripple above substrate) accessible to hydrogen atoms only on one side showed an irregular amorphous structure. The empirical findings were supported by computations based on the consideration of stepwise hydrogenation of fixed and free graphene membranes accessible to the hydrogen atom from either one or two sides [46].

As shown above, it is possible to proceed to chemical modification of graphene in the basal plane only after complete inhibition of the high chemical activity of edge atoms. Although N_{DA} values in this domain are much smaller than on the bare circumference (Fig. 2b), they are still $\sim 0.3-0.1$, i.e., quite sufficient to maintain active chemical modification. However, the reality drastically differs from the desired chemical pattern of graphene sheets, whose virtual image presents the final product reminiscent of flowerbed carpets in French parks. The real pattern is more like the design characteristic of English parks. The point is that the set of effectively unpaired electrons which strictly controls each step of the chemical process has no means needed to predict the modifier deposition sites many steps forward, because each deposition event causes an unavoidable collective structural deformation due to local $sp^2 \rightarrow sp^3$ transformation at the site of contact with graphene. Relaxation of deformation accompanied by redistribution of C=C bond lengths extends over a large area (Fig. 8). Trying to continue the patterning, it is impossible, without calculations, to guess on exactly what carbon atom the maximum reactivity will be concentrated, thus distinguishing this atom as a target for the next deposition.

Therefore, even two simultaneous depositions cannot be predicted. That is why the desired regular chemical modification of a graphene basal plane exists only in virtuality. The real situation studied in detail for the case of graphene hydrogenation [98] revealed random gradual filling of the basal plane with hydrogen atoms. The final products of addition reactions on basal planes of graphene strongly depend on the reactants used. Thus far, none of the regular motives was invariably observed in all stepwise reactions.

To overcome difficulties and reach the desired goal of forming a regularly patterned modifier on the graphene basal plane, the graphene sheet should be transformed into a sort of chemical template reactor with the orderly distributed regioselectivity of atoms. This can be achieved by regularly distributed swelling of the carbon backbone (see Section 4.2.4 for details). Indeed, due to the predominant role of the interatomic distance in the correlation of odd p_z-electrons (as regards C=C bonds), any deformation leading to stretching (compression) of these bonds greatly affects the behavior of the electrons. As a result, bend apices (interbeds) become sites of enhanced (diminished) ACS [27]. Such a reactor with regularly distributed regioselective domains is easy to generate by placing a graphene sheet over the substrate with regular pattern formed, for instance, by nano-sized pyramids or metal nanoparticles. A similar template is obtained when a single-layer graphene is deposited on metallic surfaces. Due to the incompatibility of lattice constants of graphene and the metal surface, the sheets form an incommensurate phase showing the moire pattern responsible for graphene swelling. Swelling tops become the sites of priority binding with any reactants, which contributes to the regular chemical modification of graphene.

Such a possibility was realized by L Hornekaer's group, who demonstrated controlled opening of the gap in the electronic spectrum by means of graphene hydrogenation at the Ir(111) surface [99]. The graphene/Ir(111) interface has a moire structure with a hexagonal superlattice. Hydrogen clusters bind only to specific sites of the graphene superlattice and thereby contribute to the conservation and lowering of the Dirac cone spectrum in intact graphene (Fig. 19) and bandgap opening. This method allows a number of various combinations that, if supplemented by adsorption of bi- and multilayers with the application of mechanical deformation, correlate the gap opening problem with the remarkable emergent spin mechanochemistry of graphene.

2.10 *A posteriori* considerations

It follows from the above that the emergent physical properties of graphene, unlike its molecular properties, are difficult to implement in technological applications, bearing in mind the challenging problem of preparing graphene micrometer layers with stable properties, despite recent impressive progress in producing large high-quality graphene films [101]. This situation stimulated the search for technologically stable materials resembling Dirac topological insulators. After this review had been submitted for publication, *Science Advances* reported the possibility of substituting 2D graphene by a 3D sodium bismutide (Na_3Bi) crystal whose 3D electronic spectrum is described by the Dirac fermion spectrum, as a 2D graphene crystal spectrum [102]. The authors believe that the availability and high technological characteristics of this 3D Dirac material taken together will allow 'new physics' to be realized, which so spectacularly manifested itself in 2D graphene. A distinctive feature of this physics is emergentness. It is this fact that gave rise to one more new avenue in graphene research related to 'artificial graphenes'.

Molecular graphenes realized in the form of graphene-like atomic structures with modified primitive cells were discussed in Section 2.7. The main purpose of creating such structures was to obtain and control the spectrum of 2D Dirac fermions. Researchers developing artificial analogs work toward the same goal but trying to attain it based on elementary particles and quasiparticles instead of atoms. This implies the forma-

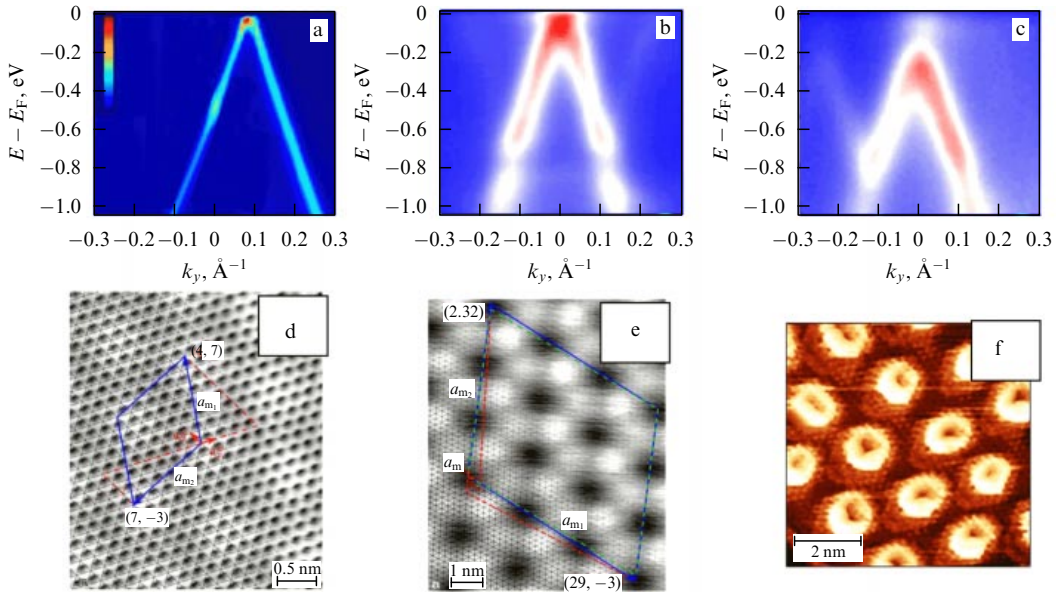

Figure 19. (Color online.) ARPES Dirac cones of graphene (top) (ARPES — angle-resolved photoelectron spectroscopy) and STM periodic patterned structures of interfaces (bottom). (a, d) Graphene/6H SiC interface at $T = 6$ K. (Adapted from Ref. [98].) (b, e) Graphene/Ir(111) interface: [Adapted from Ref. [99] (b) and [100] (e).] Blue and red lines in figures d, e denote vectors of the graphene lattice and moire superlattice, respectively. (c, f) Graphene/Ir(111) interface saturated with atomic hydrogen at 645 K. (Adapted from Ref. [99].)

tion of an artificial honeycomb lattice giving rise to phenomena analogous to those generated by Dirac 2D fermions in terms of behavior. Photonic band structures [103], photonic crystals [104], and topological photonics [105] were the first research areas to meet this challenge. Creation of optical honeycomb lattice to capture ultracold potassium atoms [106, 107] made it possible to study factors influencing the Dirac cone structure. Thus, the Dirac point location can be altered by changing the lattice anisotropy. Photons and polaritons [108] were followed by electrons. 2D electron gas in a quantum well of nanostructured GaAs [109] was shown to form an artificial honeycomb lattice and obey the laws that govern Dirac fermion behavior. Analysis of conditions under which these phenomena occur again reveals familiar time-reversal and spin symmetry breaking and underscores graphene emergentness as a connecting link between graphene and its 'molecular' or 'artificial' analogs.

3. Magnetism as an emergent property of graphene

3.1 Unexpected peculiarities and distinctive features of experimental results

In accordance with the Butterfield principle [9] considered in Section 2.1, emergent phenomena are characterized as 'weak'. This term is fundamentally important because it specifies weak interactions in an electron system. In fact, the above UHF emergents are a set of differences between the solutions of RHF and UHF approximations and can be represented as resulting from the contribution of the second-order approximation of the perturbation theory to the initial RHF solution [110]. Due to this, physical effects resulting from weak interactions become the first objects of emergent manifestations. In solid state physics, these are, first and foremost, magnetism and superconductivity [1–5], which will be considered below with respect to graphene.

Repeatedly tested large graphene sheets are diamagnetic specimens. The magnetic response from them could be obtained empirically after their intense irradiation by proton beams or chemical modification (hydrogenation, oxidation, etc.) of graphite and/or graphene (see review [111] and references cited therein). A thorough analysis of each case allowed excluding the impurity origin of magnetism and attributing it either to graphite/graphene itself, although it is caused either by micro- or/and nanostructuring of the specimens, or to defects of a different topology created during chemical modification (see Refs [112–115] for related examples). Importantly, the authors described the magnetic response as ferromagnetic and observed it practically in all experiments, including those at room temperature for graphene species with zero total spin density in the ground state.

Another scenario of observing the graphene magnetism, namely its paramagnetism as a consequence of fluorination or bombardment by protons of graphite-like columns consisting of 10–50 nm graphene flakes, was described in Refs [114–116]. The treatment broke C=C double bonds and thereby induced 'spin-half paramagnetism'. In both cases, magnetization was weak and corresponded to roughly one spin per 1,000 carbon atoms. This ratio gave evidence that the post-treatment magnetic crystalline structure of the specimen differed from the initial one with its unit cell being $\sim 33/2$ times larger than the spatial one and containing an additional spin, which lifted the spin multiplicity to doublet. Adatoms and point defects thus introduced cause magnetic nanostructuring of the initial crystal with nonzero total spin density.

Nanostructuring, the chemical–technological pre-history of graphene specimens, and the role of these two factors in high-temperature ferromagnetism of graphene remain to date the main subjects of empirical magnetism studies. One of the first publications concerning this issue [117] reported the close relationship between these factors. Figure 20a, b illustrates the magnetization curves of two graphene powders at two different temperatures. Graphene specimens were final

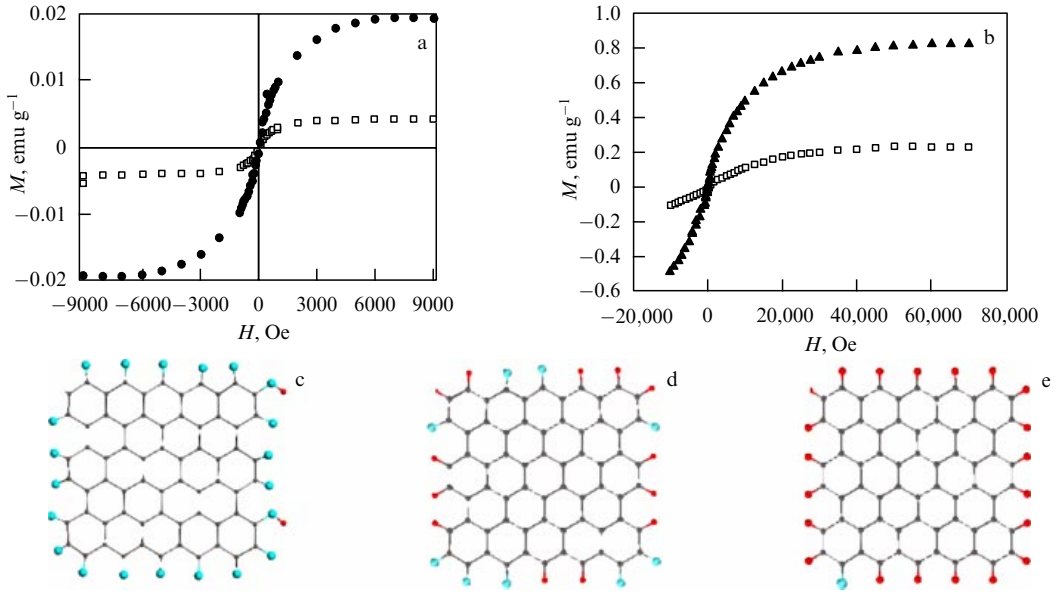

Figure 20. Magnetic hysteresis loop of graphene-400 and graphene-600 specimens (filled and empty symbols, respectively) at 300 K (a) and 2 K (b) (adapted from Ref. [117]). (c–e) Models of nano-sized technical graphene corresponding to natural shungite carbon. (Adapted from Ref. [118].)

products of the complex chemical–technological cycle, viz. nanodispersion (of pristine graphite)–oxidation–reduction accompanied by thermal treatment at 400–600 °C after terminating reactions (graphene-400 and -600 samples, respectively, in Fig. 20). The ferromagnetic character of magnetization is obviously detected in both cases at low temperature and at room temperature alike, but it is somewhat less pronounced in the latter case.

The central result of this investigation, apart from magnetism itself, was a marked difference in the behavior of the two samples. The authors failed to explain this effect and confined themselves to merely mentioning differences in the general conditions of the thermal treatment of the study samples. It has now been reliably established, however, that the end product of a nanodispersion–oxidation–reduction cycle is technical graphene representing the so-called framed graphene oxyhydrides with the edge atoms terminated by oxygen-containing groups and/or hydrogen atoms. Both the composition and the number of groups and atoms vary in a wide range, depending on the concrete protocol of the chemical–technological cycle and the size of the starting graphene oxide sheets [19, 118]. The thermal treatment of oxyhydrides is accompanied by alteration of the chemical composition of the framing groups. Figures 20c–e show from left to right such changes from primary reduced graphene oxide to final technical graphene comprising an almost 100% graphene hydride.

These models, related to a real object, were designed taking into consideration its chemical composition and size empirically found for the starting, intermediate, and end products of the nanodispersion–oxidation–reduction cycle. The chemical composition and size of technical graphene fragments used in the magnetic experiment are unknown. Only the facts are certain that this graphene does not contain unterminated fragments of ideal graphene, and the composition of the framing groups changes with treatment temperature. Moreover, the thermal treatment not only alters the chemical composition but also leads (with high probability) to cracking of the fragments (see Section 2.9), meaning that the result presented in Fig. 20a, b can be due to both chemical and size effects.

Convincing evidence of the key role played by the size of graphene samples was obtained in specially designed experiments [119–121]. In one case, the specimen looked like a peculiar continuous sackcloth linen formed by entangled graphene nanoribbons with round cells at the intersections representing spots of completely hydrogenated or oxidized graphene. In another case, a specimen of similar structure was prepared by layering a continuous graphene linen over a regular composition of similarly sized MgO nanoparticles. The graphene blanket was fixed by chemical bonds with the substrate at the sites (spots) of graphene contact with particle vertices. In the third case, ferromagnetic ordering of spins on zigzag edge atoms of 3–10-nm wide graphene nanoribbons at room temperature was deduced from the dependence of the width of the open energy gap on the ribbon width.

A general view of the sample and the results obtained in the first case are presented in Fig. 21. Graphene linen was overlayered on an aluminum oxide template with a regular porous pattern (Fig. 21b). Then, the sample was subjected to one-side hydrogenation or oxidation through the pores to form spots of chemically modified graphene separated by crosspieces made of pristine graphene ribbons. The ribbons thus obtained formed a regular sackcloth mesh, with graphene fibers retaining intact basal planes unaffected by chemical treatment but terminated on the ends consisting of carbon atoms arrayed along the template perimeter. The width W of the ribbons in the set of templates ranged from 10 to 50 nm. The magnetic responses of the graphene mesh obtained in this way at room temperature are shown in Fig. 21c, d for ribbons of various widths W; the inset demonstrates the W-dependence of sample magnetization. In the second case, the chemically modified dark disks in Fig. 21b are replaced by extended sites of contact with MgO nanoparticles [120]. The ribbon width between such contact sites in the mesh was ~ 10 nm.

Chemical termination of the ribbon edge atoms along the contact region perimeter was ensured by binding carbon

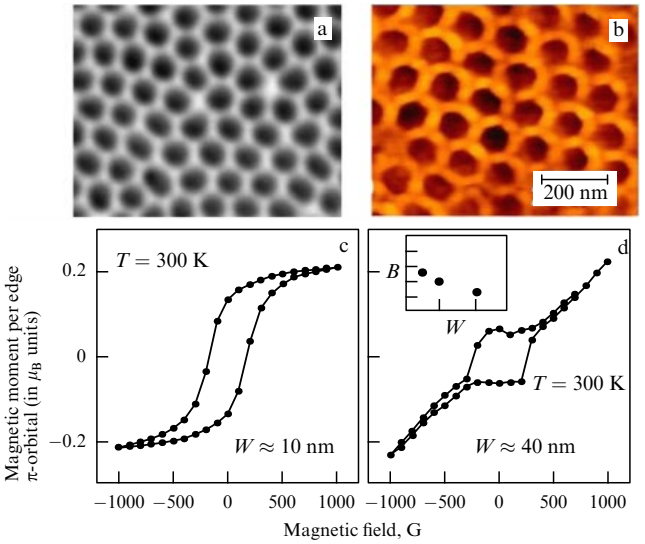

Figure 21. (a) SEM image of a nanoporous aluminum oxide template with mean pore diameter of ~ 80 nm and mean interpore distance $W \sim 20$ nm. (b) AFM image of nanoporous graphene linen formed with the use of (a) a template as an etching mask for one-side hydrogenation of the sample. (c, d) Magnetization of monolayer graphene linens at $W \sim 10$ and 40 nm. Inset shows dependence of residual magnetization of graphene ribbons on their width W. (Adapted from Ref. [119].)

atoms of graphene mesh to a surface of MgO particles. The magnetic response of the specimen is analogous to that shown in Fig. 21c. The ribbon-width dependence of magnetization could be deduced only qualitatively by a comparison with the reference signal from technical graphene sheets (reduced graphene oxide) [118] having a minimal linear size of about 100 nm, which was several-fold weaker. In both cases, the authors of the study described their results as the observation of graphene ferromagnetism at room temperature.

Thus, the nanostructuring of the sample carried out and size dependence of its magnetization, on the one hand, and the high-temperature ferromagnetic character of the phenomenon, on the other hand, are two peculiar features of graphene magnetic behavior characterized by zero total spin density. Clearly, the former determines the very existence and magnitude of the magnetic response of a graphene molecule, whereas the latter is relevant to the nature of the magnetism of a nanostructured graphene crystal. Let us consider separately these two aspects of graphene's magnetic behavior.

3.2 Magnetic behavior of graphene molecules

It has been repeatedly emphasized in the preceding sections that graphene is a material for which $N_\alpha = N_\beta$, and its zero spin density implies the absence of free spins. Such magnetic species are usually called 'singlet magnets', and their magnetization is attributed to various effects resulting in a mixture of the singlet ground state with states of a higher spin multiplicity [122]. As a rule, magnetization of singlet magnets is insignificant, and the spin mixture of their states is considered in the framework of the second-order perturbation theory (PT). If the mixture is caused by a magnetic field, such induced magnetization is referred to as van Fleck magnetization [123]. However, the electron system of graphene is an open-shell system; therefore, its singlet ground state is intrinsically spin-mixed due to the correlation of odd p_z-electrons. Since the difference between RHF and UHF formalisms is also described as the second-order PT effect, spin mixing as a consequence of spin symmetry breaking is entirely analogous to that associated with the van Fleck effect.

Among other factors, the observation of contributions described by the second-order PT is essentially dependent on the energy denominator. For singlet substances, triplet states serve as the main contributors; therefore, the energy denominator equals $2|J|$, where J is the exchange integral defining the energy dependence of the sequence of pure spin states in terms of Heisenberg Hamiltonian $H_{ex} = JS(S+1)$. This integral is usually termed the magnetic coupling constant [124] and is difficult to calculate. Fortunately, L Noodleman derived some forty years ago a simple expression for defining this parameter for open-shell molecules [125]. Moreover, he coined the term 'broken spin symmetry approximation', which implies in the context of the present discussion consideration of the magnetic behavior of these molecules as an emergent phenomenon. According to the Noodleman approximation, one has

$$J = \frac{E^{U}(0) - E^{U}(S_{max})}{S_{max}^2} . \qquad (6)$$

Here, $E^{U}(0)$ and $E^{U}(S_{max})$ are the energies of the UHF singlet and the states with the highest spin multiplicity S_{max}, which refers to a purely spin state. The J values thus obtained are widely used to estimate the magnetic susceptibility of molecules. It was shown in Ref. [126] in application to molecular magnetism that the measurable magnetization response can be recorded if $|J| \leqslant |J_{cr}|$, where the empirically evaluated $|J_{cr}|$ ranges $10^{-2}-10^{-3}$ kcal mol^{-1}. Let us see which J values can be expected for graphene molecules in the light of molecular magnetism.

The calculated J values for certain graphene molecules are collated in Table 1. Evidently, the magnetic constant depends on the molecular size; it lowers slowly with increasing size. This dependence can be interpreted as a result of strengthening the electron correlation, thereby suggesting the collective character of the event. Indeed, the diamagnetic behavior of graphene molecules is provided by their σ-electrons, whereas the ferromagnetic contribution should be related to odd p_z-electrons. As mentioned above, the primitive cell of a graphene crystal, determining the magnetic properties of the ideal crystal, contains two atoms linked by a single C=C bond of the benzenoid unit. Estimation of $|J|$ values for ethylene and benzene molecules with C=C bonds stretched up to 1.42 Å, as is typical, on average, of graphene, leads to 13 and 16 kcal mol^{-1}, respectively. Although ethylene and benzene molecules do not reproduce exactly a graphene unit cell, similar values for the cell magnetic constant are self-evident. Therefore, any magnetization, besides diamagnetism, is negligibly small, which explains why crystalline graphene demonstrates only diamagnetic behavior.

To ensure appreciable magnetization over the diamagnetism level, the magnetic constant must be sharply decreased. Table 1 shows that the minimum value of $|J|$ is 0.3 kcal mol^{-1} for (15, 12)NGr. However, this is still too high to maintain magnetization of the graphene molecular magnet. Nonetheless, the tendency apparent from the table is rather optimistic. Assuming $|J|$ to be inversely proportional to the number of odd p_z-electrons, one can deduce their number needed for approaching the range of $10^{-2}-10^{-3}$ kcal mol^{-1}, which gives $N \sim 10^5$. For NGr molecules that are rectangular compositions of benzenoid rings, the required number N of

p_z-electrons is provided by $\mathcal{N}$ carbon atoms equaling, in accordance with Ref. [127],

$$\mathcal{N} = 2(n_a n_z + n_a + n_z)\,. \quad (7)$$

To fit the needed N value of $\sim 10^5$, indices n_a and n_z should be of order a few hundred, which implies a linear size of NGr molecules from a few units to a few dozen nanometers. This rough estimate fairly well agrees with the observed ferromagnetism of activated carbon fibers consisting of nanographite domains ~ 2 nm in size [128], and with the data on ribbon-shaped sackcloth graphene [119, 120], discussed in Section 3.1. To recall, the maximum magnetization effect was documented for samples with the ribbon width $W = 20$ nm in a graphene mesh [119], after which the signal gradually attenuated with increasing W. Such a behavior of graphene magnetization is analogous to that of fullerene oligomers [129] on the assumption of the scaly mechanism of the magnetism emergence in the nanostructured solid-state polymerized fullerene C_{60}, which was confirmed in experiment.

The data in Table 1 indicate that framing ideal graphene flakes with chemical reactants typical of a technical graphene composition not only decreases the magnetic constant but, on the contrary, increases it. Thus, the 'two-sample effect' [117] illustrated in Fig. 20a, b is, in all probability, indicative of the size effect caused by cracking of technical graphene samples into fragments of various sizes at different temperatures.

These observations demonstrate one more noticeable aspect of graphene magnetism allowing it to be defined as a size-dependent phenomenon. Thus, graphene ferromagnetism was observed only for nano-sized specimens, more than that for samples whose linear dimensions fit a definite interval, while neither smaller nor bigger samples outside the critical region exhibit magnetic behavior. Actually, an individual benzenoid unit (and benzene molecule) is only diamagnetic. When the units are joined to form a honeycomb-like benzenoid cluster, effectively unpaired electrons appear due to the weakening of interactions among odd p_z-electrons in consequence of stretching the C = C bonds, which strengthens correlation between these electrons. Correlation becomes even stronger as cluster size (the number of lengthened C = C bonds) increases, with the magnetic constant $|J|$ decreasing until it reaches a critical value $|J_{cr}|$ needed to ensure the necessary spin contamination of the cluster ground state. Magnetization will continue to grow till further enlargement of the cluster size disturbs the molecular (cluster-like) behavior of odd electrons. However, as soon as the electron behavior becomes spatially quantized, the molecular character of magnetization is broken and substituted by a solid-state one determined by the electronic properties of the primitive cell characterized by a large magnetic constant.

Critical size parameters controlling quantization of molecular properties depend on the type of quasiparticles to be considered. As far as graphene ferromagnetism is concerned, this role is played by Dirac fermions, with their mean free path l_{fm} determining the critical size parameter: when the cluster size exceeds l_{fm}, spatial quantization quenches cluster magnetization. Recent experiments have demonstrated the dependence of low-energy fermion band linearity of $E_{fm}(k)$ inside Dirac cones near the Fermi level and the spectrum shape on the size of graphene samples.

Figure 22 presents a set of $E_{fm}(k)$ spectra related to a polycrystalline graphene sample composed of differently sized grains [130]. The figure shows that quantization is fairly well realized in 150-nm grains, but begins to be distorted in 100-nm grains, and is markedly impaired in 50-nm grains. A considerable broadening of the spectrum in the last case allows putting the upper bound for l_{fm} at around 50 nm. A comparable l_{fm} value of ~ 20 nm follows from the analysis of molecular graphene in the form of hexagonal packing of CO molecules [69] in Fig. 13.

Obviously, the transition from a localized to quantized state is not abrupt. At the ribbon width of meshed graphene $W = 40$ nm, residual magnetization is only half its maximum value at $W = 20$ nm (see inset to Fig. 21d), and its continuous approach to zero may occur within a rather wide range of W values. Actually, in the second case of ribbon-cellular graphene [120], magnetization of the sample with the ribbon width $W = 10$ nm is only $\sim 20\%$ higher than for ~ 100-nm

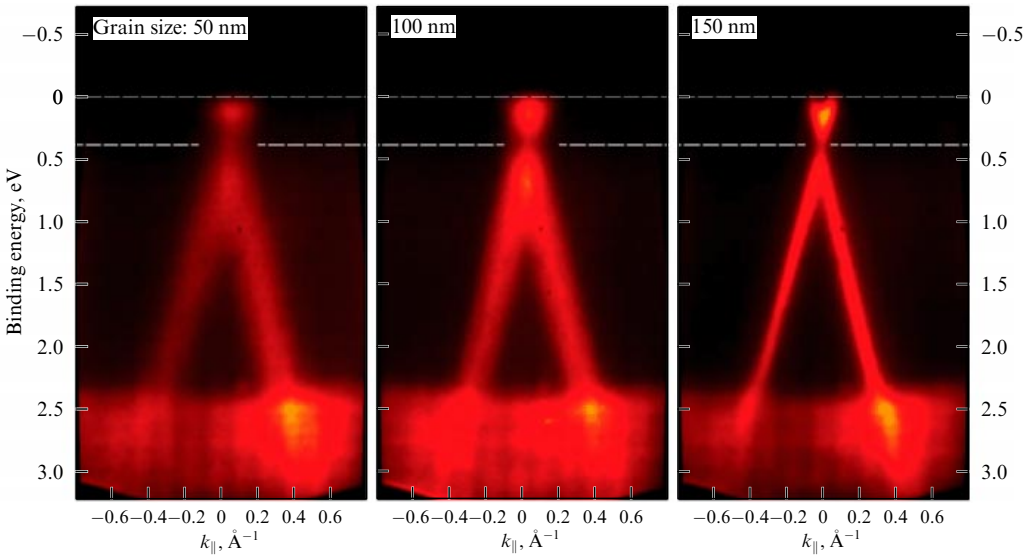

Figure 22. ARPES Dirac cones of continuous graphene film with average grain sizes of 50, 100, and150 nm. Fermi energy is zero. (Adapted from Ref. [130].)

technical graphene flakes. Nevertheless, the linear size of the molecules comparable to the fermion mean free path is the key factor governing the manifestation of ferromagnetism in graphene as confirmed in practice by observations of the magnetic response coming only from nanostructured graphene samples (see Section 3.1).

3.3 High-temperature magnetic topological phase of graphene

Although the discussion in the previous section allows us to understand when the magnetic behavior of graphene becomes measurable, it does not answer the question as to why ferromagnetism is the main form of its magnetic behavior and why this property manifests itself up to room and higher temperatures. As regards the ferromagnetic mode, the problem is even more complicated, because UHF calculations reveal the negative sign of the magnetic constant characteristic of antiferromagnetic behavior, in agreement with zero spin density in the ground state. This means that spin symmetry breaking does not lead to ferromagnetism and its appearance should be attributed to time-reversal symmetry breaking [131].

The notion of graphene ferromagnetism as an observable phenomenon was introduced into graphenics by experimentalists who studied characteristic hysteresis loops [112–121] similar to those shown in Fig. 21c. It follows from the figure that magnetization of a sample with ribbon width $W = 20$ nm is represented by a classical hysteresis loop characteristic of ferromagnetics and demonstrating the presence of nonzero magnetization of a specimen in a zero magnetic field. At the present time there is no explanation for the existence of residual magnetization of graphene ribbons. Theoretical and computational substantiations discussed in Refs [112–121] are based on model calculations of graphene ribbons in terms of the density functional theory with emphasis on peculiar states imported into electronic spectra of the ribbons by their edge atoms (see paper [121] and references cited therein, in addition to Refs [39–43]). Erroneous results of these calculations and an extremely narrow scope of applicability of DFT methods to substances with open electron shells are matters of thorough analysis in the literature [21, 22] and were discussed in Section 2.2 of this review.

As far as ferromagnetism of graphene ribbons is concerned, spin ferromagnetic ordering was frequently included in starting models. In contrast, the local spin model takes into consideration the open-shell structure of graphene, and representing the response of the molecule to spin symmetry breaking appears to be more optimistic, because the notion of time-reversal symmetry breaking, in addition to spin symmetry breaking, permits accepting complete or partial ferromagnetic ordering of these spins. Then, the observation of graphene ribbon ferromagnetism gives evidence that both breakages occur as intrinsically related to the respective contributions determined by the parameter ratio. Low levels of residual magnetization in available experiments [117, 119, 120] suggest that the advantage of parameters in favor of time-reversal symmetry in this ratio is insignificant. A strong argument supporting this conjecture is provided by the form of the hysteresis loop presented in Fig. 21d. Careful examination reveals that it is drastically different from the loop in Fig. 21c in that its main part takes the shape of a quadrangle with the sides parallel to the axes and saturation regions are replaced by a simple linear dependence. On the whole, the loop assumes the shape characteristic of antiferromagnetic hysteresis loops under conditions of possible 90° spin-flip in the magnetic field [132]. The sole factor inducing the change in the shape of the loop is the variation in ribbon width. This unusual size effect relating to the change in magnetic spin ordering awaits detailed theoretical analysis.

3.4 Ferromagnetism of magnetic impurities adsorbed on graphene

The issue of time-reversal symmetry breaking in graphene makes us turn to the results of theoretical studies [132–135] that demonstrate ferromagnetic ordering of magnetic impurities on the surface of the topological insulator. It has emerged that similar phenomena in graphene were observed in experiment. One effect is related to the behavior of a magnetic impurity deposited onto a graphene substrate [136]. Figure 23 shows a molecular magnetic complex Er(trensal) adsorbed at graphene/Ru(0001) and graphene/Ir(111) interfaces and on the bare Ru(0001) substrate. Clearly, the molecules at both interfaces are self-assembled into well-ordered islets with easy magnetization axes orthogonal to the solid substrate surface. In contrast, molecules on the Ru(0001) substrate remained disordered and showed only weak directional preference along the easy magnetization axis. Accordingly, the ferromagnetic response was spin-polarized in the former two cases but not in the third one, where it is half the magnitude. Substituting iridium for

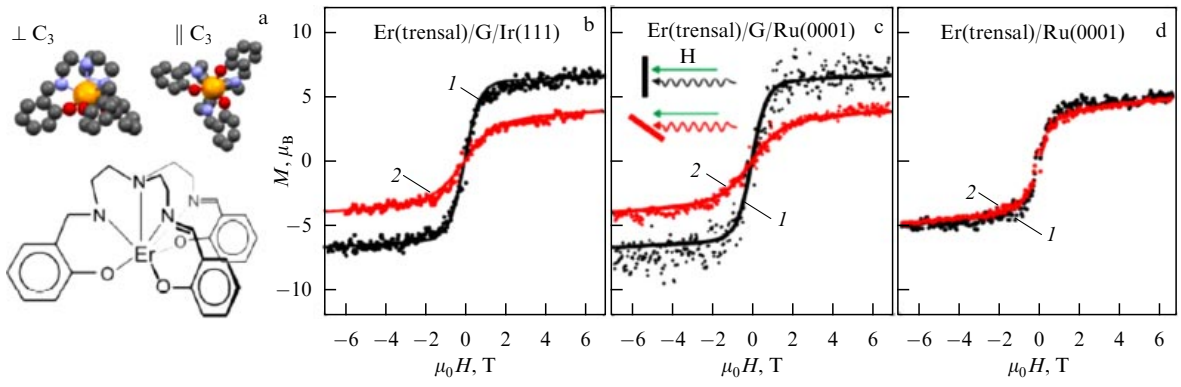

Figure 23. (Color online.) (a) Structure of an Er(trensal) molecular magnet. Coloring: orange: Er; blue: N; red: O; grey: C; H atoms are omitted for clarity. (b–d) Magnetization curves at normal (black curves *1*) and tilted (red curves *2*) orientation of the magnetic field with respect to the substrate surface. (Adapted from Ref. [136].)

ruthenium produced no additional effect on molecular impurity ordering, which allows attributing all the observed peculiarities to the graphene layer. In a word, the topologically trivial ruthenium surface does not influence the ordering of molecular impurities, whereas the addition of a graphene monolayer promotes ferromagnetic ordering of impurity spins.

Not only ordering but also enhancement of the ferromagnetic response suggest a topologically nontrivial character of the graphene constituent of interfaces. It is well known [137, 138] that in the presence of magnetic impurities the main Hamiltonian describing the band structure of the topological insulator in the form of equation (5) is substituted by a new one:

$$H = hv_{\mathrm{F}}(\mathbf{k} \times \hat{\mathbf{z}})\,\boldsymbol{\sigma} - H_{\mathrm{ex}}\,, \tag{8}$$

where v_{F} is the Fermi velocity, $\hat{\mathbf{z}}$ is the unit vector normal to the surface, $\boldsymbol{\sigma}$ is the electron spin, and

$$H_{\mathrm{ex}} = \sum_{r} J_z s_z(\mathbf{r})\, S_i(\mathbf{r}) + J_{xy}(s_x S_x + s_y S_y)\,. \tag{9}$$

Here, $S_i(\mathbf{r})$ is magnetic impurity spin at point $\mathbf{r}$, $s_i(\mathbf{r}) = \psi^*(\mathbf{r})\,\sigma^i\,\psi(\mathbf{r})$ is the surface electron spin, and J_z and J_{xy} are the coupling parameters. If impurity atom spins are polarized in the z-direction, the second term in Eqn (9) vanishes. Because each magnetic impurity opens a local gap in the immediate proximity to itself, one may expect the system to be gapped everywhere, at least at the mean-field level. However, this is not necessarily true in the case of nonuniform magnetization of magnetic impurities. Taking on the problem and comparing the formation of the magnetic domain wall and ferromagnetic packing, the authors of Refs [137, 138] came to the conclusion that magnetic impurities must be ferromagnetically coupled. Sharing this viewpoint, the authors of Ref. [139] suggested a similar Hamiltonian H_{ex} to describe Dirac fermion-mediated ferromagnetism of magnetic impurities in the topological insulator:

$$H_{\mathrm{ex}} = Jn_{\mathrm{s}}\bar{S}_z\sigma_z\,. \tag{10}$$

Here, σ_z is the z-component of the electron spin, and n_{s} is the local spin density with an averaged z-component $\bar{S}_z$. J describes the exchange coupling between the z-components of the Dirac electron spin $\boldsymbol{\sigma}$ and the local spin $\mathbf{S}$ determining the normal orientation of $\boldsymbol{\sigma}$ with respect to the wave vector $\mathbf{k}$.

As to enhancement of magnetization, $J_z s_z(\mathbf{r})$ on the right-hand side of Eqn (9) acts as an effective magnetic field that magnetizes magnetic impurities and polarizes local spins of topological insulator electrons. It can be speculated that such dual action of exchange coupling enhances the magnetic response. When magnetic impurities form a continuous adsorption layer, one can expect an additional enhancement of magnetization due to the magnetic proximity effect (see one of the last publications [140] and references cited therein).

Several interesting experiments reported recently dealt with graphene action on a system of external magnets [141–143]. These studies revealed spin filtration of electrons in complex interface contacts FM/Gr/FM composed by a sandwich of ferromagnetic metals (FMs) with one or a few graphene layers between them. The observed effect, common to both cases, is shown in Fig. 24. Monolayer (three-layer) graphene was placed on NiFe [139] (Ni [140]) ferromagnet and covered by the same ferromagnet from the other side. This sandwich structure was characterized by the transport of electrons with distinguished spin orientation. Such an effect is conceivable in the light of the unique properties of the topological insulator and implies the aforementioned electron spin locking with respect to momentum. Therefore, an evoked ferromagnetic order can be expected in the TI system or at sites of contact with the magnetically ordered adsorbate layer, as in the case of molecular magnet adsorption [136] (see Fig. 23) or due to the magnetic proximity effect [140].

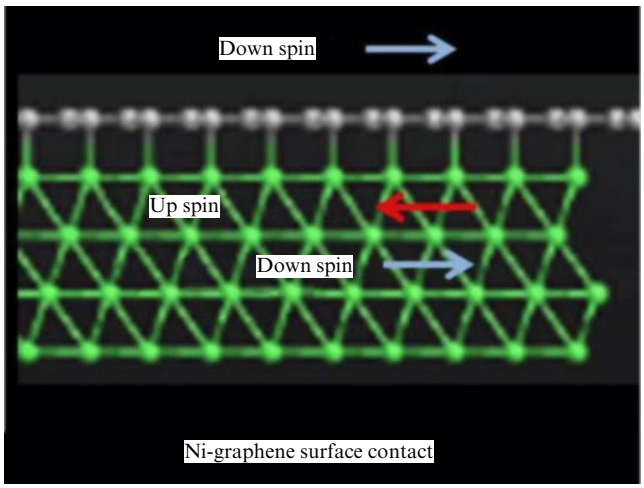

Figure 24. Schematic of a spin filtration at the ferromagnetic metal/graphene interface (adapted from Ref. [142]).

In both cases, interface ferromagnetism stands as an important property having a strong influence on the behavior of introduced spins. It certainly hampers spontaneous spin transport by creating conditions favoring concrete spin orientation and thereby maintaining the aforementioned spin filtration. Apart from peculiarities created by the graphene/magnetic substance interface, some interesting magnetic phenomena are predicted for graphene/TI interfaces [144–146].

3.5 Graphene superconductivity

The above description of the ferromagnetic behavior of magnetic impurities on the graphene surface removes last doubts that graphene behaves like a typical TI, on the one hand, and that it is characterized by spin and time-reversal symmetry breaking, on the other hand. Additional evidence of the break of a time-reversal symmetry is provided by experimental observation of graphene superconductivity. The first report of this phenomenon in Ref. [147] described peculiarities of the Josephson effect produced by sandwiching a graphene sheet between two superconducting contacts, which testified to the superconducting capacity of graphene and confirmed time-reversal symmetry breaking. Thereafter, the splitting of Cooper pairs was observed after they were introduced from the superconductor into two spatially constrained pieces of graphene (quantum dots) [148]. The placement of a graphene monolayer on the surface of an $Sr_{1.85}Ce_{0.15}TiO_4$ superconducting crystal gave rise to interfacial superconductivity [149] (Fig. 25a). Scanning the tunneling spectroscopy response $\mathrm{d}I/\mathrm{d}V$ revealed three unique interface 'fingerprints' characteristic of superconduc-

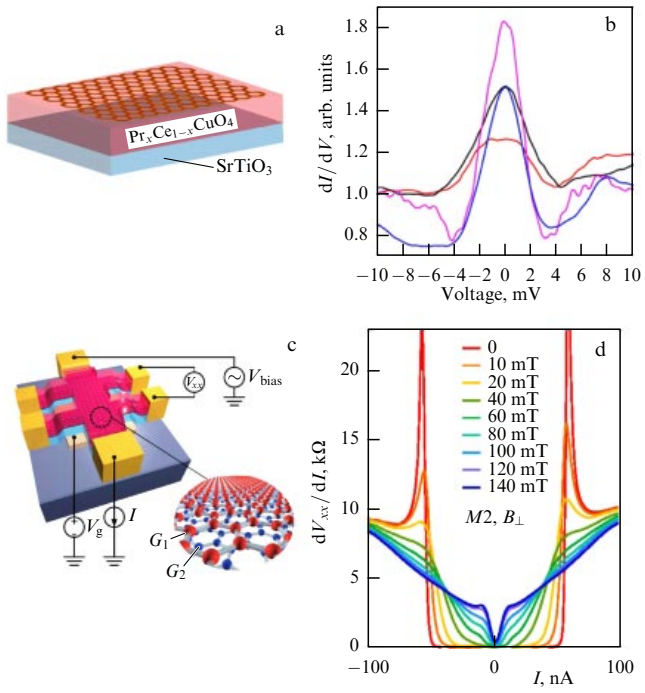

Figure 25. (a) Scheme of a superconductor/graphene interface. (b) Zero shift peaks scanned in different interface regions at $T = 4.2$ K (adapted from Ref. [149]). (c) Schematic representation of a device in the form of an h-BN/twisted bilayer graphene/h-BN sandwich. (d) Response of the superconducting state of bilayer graphene to a magnetic field applied normally to the device: differential resistance depending on bias DC at different strengths of the magnetic field (adapted from Ref. [150]).

tive behavior, viz. V-shaped gaps, zero shift peaks, and splitting of these peaks. Typical zero-shift scanning data are presented in Fig. 25b. Similar results were reported recently for bilayer graphene with a small 'twist' angle between different layers [150]. Figures 25c, d give a general view of the experimental device and the dependence of the dV/dI response on the strength of the applied magnetic field. In zero and weak fields, the response has a characteristic shape indicative of the superconducting capacity of the graphene sample.

The close inner relationship between TI and superconducting properties [88, 131] gives highly convincing evidence that high-temperature ferromagnetism and superconductivity of both graphene itself and graphene-related interfaces are provided by graphene topological nontriviality. Importantly, interfacial superconductivity is retained at a temperature much higher than that of the superconducting substrate. A similar rise in temperature above the Curie point of the respective ferromagnetic substrate occurs during interfacial ferromagnetism induced by magnetic proximity [141, 142]. Both temperature effects are characteristic of TI.

It follows from the foregoing that graphene magnetization and superconductivity are typical emergent phenomena [1–5]. In this context, the close relationship between equations of the UHF formalism and the Bardeen–Cooper–Schrieffer (BCS) theory [90] does not seem surprising. Since the two formalisms have common roots, substances in which emergentness manifests itself via UHF are inevitably prone to display superconductivity under the proper conditions, as convincingly exemplified by graphene.

4. Mechanophysics and mechanochemistry of graphene and graphane

4.1 Are the mechanical properties of graphene emergent?

If electronics, concerning the conductive, magnetic, and optical properties of matter, is recognized among the elite of quantum physics, mechanics was always somewhat ashamed of its nonelitism and tended to keep in the background of classical physics. No wonder that the deformation of continuous media is traditionally described by a set of classical physical parameters including mechanical strength of substances and their quantitative characteristics of stretching, bending, twisting, breakdown, rupture, etc. The mechanochemistry of covalent compounds (crystals and polymers) was the first to claim the right to study quantum effects in mechanics by relating the mechanical deformation of an object to stretching and breaking its chemical bonds. In the light of this fact, condensed sp^2-nanocarbons hold a special place among covalent media as the most distinctive representatives of structures formed by covalent C ∼ C (mostly C = C double) bonds, playing the key role in their unique properties and making these structures highly susceptible to deformation.

Mechanical loading inevitably changes both bond length and bond length distribution within a specimen. Because the length of C ∼ C bonds determines the open-shell character of sp^2-nanocarbons and their respective radicalization [17], mechanochemistry of sp^2-nanocarbon mechanical deformation acquires special importance. Moreover, the openness of the electron shells in these substances accounts for their local spins with zero total density [84]. As a result, deformation of sp^2-nanocarbons is accompanied by alteration of their spin structure and has a direct effect on spin peculiarities of these objects. Such terms as open electron shells, local spins of 'singlet' compounds, and their radicalization were extensively used in preceding sections when considering emergent features of graphene chemistry, magnetism, and superconductivity. Does this not mean that the mechanochemistry of graphene and its mechanics as well possess, in general, an emergent character? In this part of the review, we shall try to answer this question in the affirmative.

To facilitate the description of graphene's mechanical properties, we shall retain the arbitrary division of its mechanics into mechanophysics and mechanochemistry. The mechanophysics of graphene is a well-developed scientific discipline dominating in modern graphenics by virtue of the unique mechanical properties of this material. Difficulties in its experimental investigation left a specific imprint on the subject matter of graphene mechanophysics, making it a virtual scientific discipline mostly concerned with theoretical and computational studies. The modern view of this science is presented in a recent comprehensive review [151] published by a large group of authors. Graphene as a continuous medium, the theory of elasticity adapted to describe its peculiar properties, graphene strength and strengthening, viscosity, the formation of defects in terms of Young's modulus, and other standard (classical) parameters of the theory of continuous media, the effect of mechanical stress on electrical conductivity, and other electric characteristics are just a few of the problems facing modern graphene mechanophysics and attracting the attention of numerous researchers.

Moreover, graphene is a remarkable object exhibiting molecular-crystalline dualism. While the above problems

facing its mechanophysics are largely related to 2D crystal properties, the honeycomb structure of graphene formed by covalent C ~ C bonds is a source of its unique chemical properties also subjected to mechanical loading and responding to it by a variety of mechanochemical reactions. This part of the review 'covalently' integrates graphene mechanophysics and mechanochemistry to take a fresh view of the crystal physical properties resulting from various impacts on the system of covalent bonds in a molecule. The important virtual contribution to modern graphene mechanochemistry and the ever increasing amount of empirical evidence taken together make it possible to suggest a self-consistent picture of the physical and chemical properties exposed to external loading.

4.2 Static deformation of graphene

4.2.1 Graphene deformation as a mechanochemical reaction. The extraordinary mechanical properties of graphene form the basis of its widely recognized physical uniqueness for which the high strength of valent C=C bonds is largely responsible as a factor behind the high degree of compatibility between graphene physics and chemistry [17, 29]. However, this fact is frequently disregarded in the discussion of the mechanical properties of graphene and graphene-like materials. For example, the authors representing carbyne as an extremely strong material [152] 'forget' to emphasize the key role of triple C ~ C bonds and focus, instead, on large-scale computer simulation for reconstructing an equivalent elastic continuum to determine Young's modulus of the crystal under consideration. Such a physical approach is usually applied to analyze the mechanical properties of graphene and related materials. However, a chemical interpretation of the strength of molecules (and solid bodies) with chains of double =C=C=C= and triple −C≡C−C≡ carbon bonds allows it to be estimated without any calculations.

It was shown more than 45 years ago [153] that characteristics of the elastic component of deformation in objects with covalent bonds are related to the stretch of these bonds and therefore can be described by relevant force constants or valence oscillation frequencies squared. Due to this, elastic parameters, such as Young's modulus and stiffness, are proportional to the frequency squared of respective harmonic oscillations. Based on this rule, a very simple way to compare Young's moduli of covalent structures with single, double, and triple C ~ C bonds can be proposed. Assuming Young's modulus $E_{C=C}$ of graphene as a reference quantity yields simple expressions for graphane and carbyne moduli E_{C-C} and $E_{C\equiv C}$, respectively [29]:

$$E_{C-C} = \left(\frac{\nu_{C-C}}{\nu_{C=C}}\right)^2 E_{C=C} \approx 0.5 E_{C=C}\,, \tag{11}$$

$$E_{C\equiv C} = \left(\frac{\nu_{C\equiv C}}{\nu_{C=C}}\right)^2 E_{C=C} \approx 1.9 E_{C=C}\,. \tag{12}$$

The numerical coefficients correspond to valence vibration frequencies (ν) of C ~ C bonds, whose averaged values are 1100, 1600, and 2200 cm^{-1} in ethane, ethylene, and acetylene molecules, respectively. These relations are consistent with the more than 30% decrease in Young's moduli for hydrated graphene (see Section 4.4.4 for details) and fluorographene [154], as well as with the expected two-fold increase in Young's modulus for carbyne [152].

The chemical bonds of carbon-containing compounds not only govern the elastic properties but also determine the degree of correlation between valence odd p_z-electrons in carbon atoms. This is true of p_z-electrons in double bonds, and p_y- and p_z-electrons in triple C ~ C bonds. Due to this, any deformation resulting in bond stretching or contraction markedly affects the behavior of odd electrons involved in their formation [17], turning the mechanics of carbon-containing bodies with multiple bonds into a complicated mechano-chemical-physical phenomenon.

There are two types of this phenomenon in relation to graphene. One arises from a change in the length of initial C ~ C bonds during chemical modification of the carbon sp^2-backbone of the sample or the formation of bubble-like defects, ripples, or wrinkles on its initially flat surface. These changes, if localized, do not affect the entire sample. The second type is associated with deformation by an external load applied to the entire sample. In either case, deformation results in contraction or stretching of C ~ C bonds right up to their rupture. These changes in the sample structure under the effect of deformation underlie the mechanism of its destruction. Modern mechanophysics lacks adequate terms for the description of these two types of graphene deformation, representing the mechanochemical aspect of the phenomenon. To compensate for this disadvantage, we propose to extend the terms 'static' and 'dynamic' deformation used to describe mechanophysical processes at low and high loading rates to a representation of the structural aspect of mechanochemical processes in the presence and absence of an external load.

Modern graphene mechanophysics considers its deformation in general terms of solid state and continuous medium theory, subdividing it into elastic and inelastic with respect to dynamic and static deformation, respectively [151], leaving the behavior and structure of chemical bonds beyond the scope of discussion. At the same time, consideration of C ~ C bonds allows an alternative atomistic (chemical) approach to be implemented, since deformation of each individual bond is described well in the framework of a type-1 chemical reaction [155]. From the standpoint of such an approach, graphene deformation can be represented as a result of a complicated mechanochemical reaction involving a large number of bonds. The success of the application of both approaches depends on the development of the computational apparatus. Results of the physical approach available thus far are comprehensively presented in review [151]. The quantum mechanochemical coordinate (QMCRC) approach based on spin molecular chemistry of open-shell molecules proved the best tool for a detailed description of mechanochemical reactions [17, 19]. In what follows, we shall consider the main results of this approach to describe the mechanical properties of graphene, beginning with its static deformation. The UHF method underlying this approach not only makes possible an adequate description of the phenomenon but also brings us directly to emergent phenomena in mechanics.

4.2.2 Graphene deformation as a consequence of chemical modification. From here on, consideration will include the computational aspect of the problem and its physical reality in the form of available experimental data. The computational aspect is essentially a quantum-chemical one based, unless otherwise specified, on the consideration of various sides of the behavior of a model graphene flake. The majority

of the data obtained thus far concern flakes in the form of a nano-sized rectangular fragment, e.g., the (5, 5)NGr molecule. Chemical modification of graphene becomes a cause of its static deformation, since it stimulates sp^2-to-sp^3 conversion of the carbon atom configuration. As a result, the flat graphene structure of benzenoid units swells upon each chemical addition act, which leads to the formation of nonplanar cyclohexanoid units.

Such structural rearrangement is rather complicated and highly variable, which makes the structural alteration of the carbon skeleton sensitive to the chemical modification conditions. A set of end products of complete hydrogenation of a pristine (5, 5)NGr membrane molecule [46] is presented in Fig. 26. Graphene hydrogenation is a two-stage process (see Section 2.4 for a detailed description). First, single hydrogen atoms reside at edge atoms of the skeleton, then they join into pairs, thus giving rise to (5, 5)NGr-Hl molecules and thereafter to (5, 5)NGr-H2 molecules. At the second stage, hydrogenation continues in the basal plane, where major deformation of the initial graphene skeleton takes place.

It follows from Fig. 26 that the carbon skeleton of the starting (5, 5)NGr molecule is deformed differently depending on the accessibility of either one or two sides of the basal plane to hydrogen atoms (Figs 26b, d and 26a, c, respectively). The final result also depends on whether the initial membrane

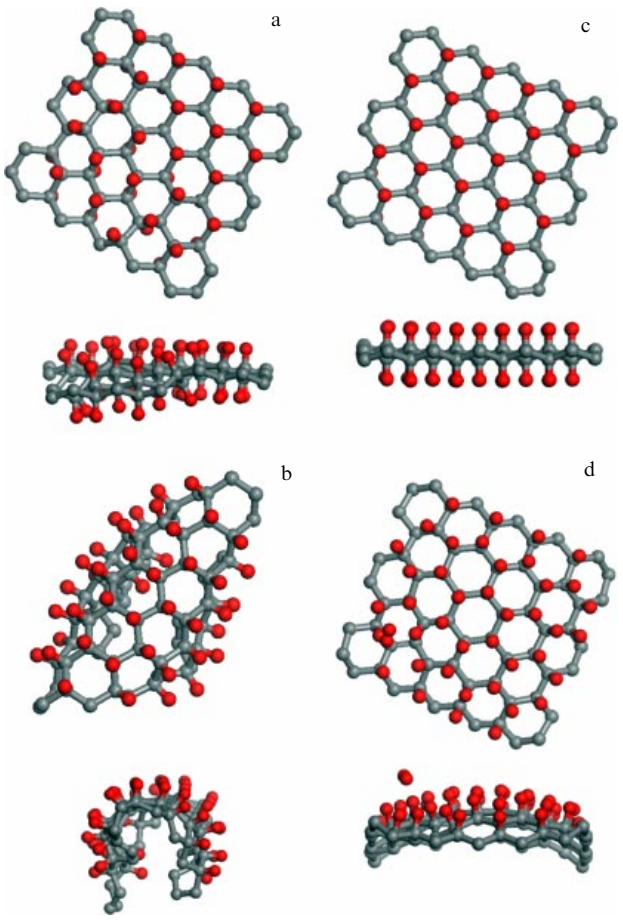

Figure 26. Equilibrium structures of graphene hydrides fully saturated with hydrogen (top and side views); they are formed by adsorption of hydrogen atoms on free (a, b) and fixed (c, d) (5, 5)NGr membrane accessible to hydrogen from two sides (a, c) and only one side (b, d) [46]. Hydrogen atoms terminating the edge atoms of honeycomb-like backbones are not shown to simplify the drawings.

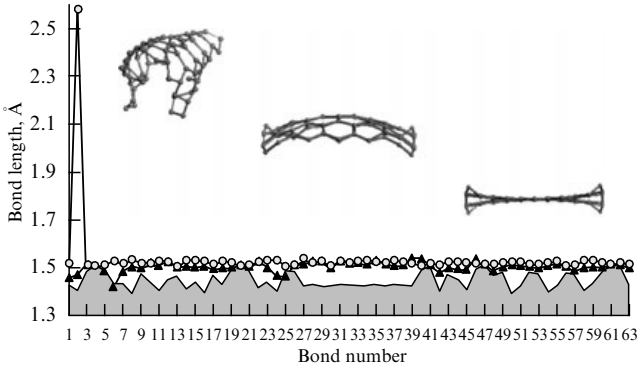

Figure 27. C ~ C bond length distribution over carbon skeletons of a (5, 5)NGr-H2 molecule (grey region), dome-shaped (Fig. 26d) (dark triangles), and basket-shaped (Fig. 26c) (grey balls) hydrides.

molecule is fixed along the perimeter (Fig. 26c, d) or is free standing (Fig. 26a, b). The causes behind such behavior (one being the high level of cyclohexane isomorphism) are described at greater length in paper [46]. In Fig. 27, it is additionally illustrated by variation of the C ~ C bond length characteristic of the carbon skeletons of dome- and basket-shaped structures resulting from unilateral adsorption of hydrogen on the fixed (Fig. 26d) and free (Fig. 26b) membranes and of the (5,5)NGr-H2 molecule. Figure 27 shows that C ~ C bonds of deformed skeletons are always lengthened, with the overall lengthening of the basket-shaped skeleton being much greater than that of the dome-shaped one. In general, the lengthening is limited to 1.53 Å to maintain the sp^3-configuration of equilibrium structures during hydrogenation. However, the accumulated strain energy sometimes cannot be distributed over all bonds, and some of them break down, as exemplified by two bonds of the basket-shaped skeleton.

4.2.3 Bubbles, wrinkles, and ripples on the graphene surface. Chemical modification of sp^2 bonds to sp^3 bonds is not the sole cause of C ~ C bonds stretching in the carbon skeleton. It can be observed in chemically unmodified graphene, too, as a result of accidental deformation with the formation of surface bubbles, wrinkles, and ripples. In what follows, graphene with such defects is referred to as corrugated graphene. In this case, the results presented in Fig. 27 have serious implications. Taking into account the influence of skeleton deformation on spin effects in open-shell molecules, including graphene, the change in C ~ C bond lengths shown in Fig. 27 must decrease the absolute value of magnetic constant J (see Section 3.2) from -1.43 kcal mol^{-1} for the (5, 5)NGr-H2 skeleton to -0.83 and -0.59 kcal mol^{-1} for the dome- and basket-shaped skeletons, respectively, with a simultaneous sharp rise in the total number of effectively unpaired electrons N_D in the skeletons from 31 to 46 and 54, respectively. Both effects result from the strengthening of p_z-electron correlation associated with enhanced deformation; they constitute a deformation emergent. Moreover, the presence of unpaired electrons markedly affects electron density distribution.

Figure 28 presents a 3D image of effectively unpaired electron density over atoms of the (5, 5)NGr carbon skeleton at different stages of deformation. Evidently, the image becomes brighter as deformation increases (note the

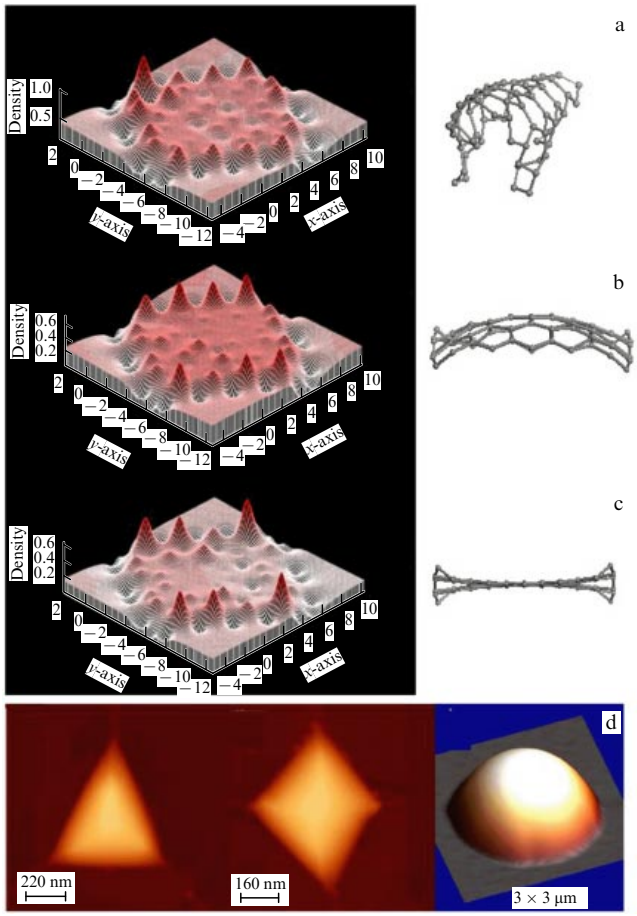

Figure 28. 3D images of effectively unpaired electron N_{DA} distribution over carbon atoms of skeletons of basket-shaped (a) and dome-shaped (b) hydrides and (5, 5)NGr-H2 (c). AFM topogram (d) of scanning triangular, quadratic, and round graphene bubbles on boron nitride (adapted from Ref. [156]).

enhanced vertical scale of the diagram in the upper part of the figure). It is clear that the basket-shaped skeleton seen in an atomic-force microscope is much brighter than the dome-shaped one, and both curved skeletons will be brighter than that of a (5, 5)NGr-H2 molecule. It is therefore natural to suggest that the deformed surfaces of graphene bubbles found in different forms on different substrates [156] and lifted over the substrate reveal the specific properties of electron density through tensile strain, which accounts for the significant enhancement of the electron density in curved structures.

Direct confirmation of the dependence of the electronic structure of corrugated graphene on the shape of the defective structure was obtained in the study of color variation of the light interference pattern on micrometer bilayer graphene drumhead membranes subjected to pressure for controling their up and down deflections that determined 'pixel' color due to variation in the number of Newton's rings [157]. The color change effect arises from interference between light waves reflected from the cavity bottom under the membrane and the membrane from above. These reflected waves interfere either additively or in antiphase, depending on membrane position and local structure. The result is either addition or subtraction of interfering wave intensities in different parts of the white color spectrum. The authors argue that such a colorimetric technique can be used in characterizing the mechanical properties of suspended materials under conditions of an adequate combination of the cavity depth and the wavelength. Parallelization of data collection by image processing instruments in combination with controlled membrane deformation allows rapidly characterizing large arrays of these mechanical systems with limitations imposed only by the resolving power of optical devices and realizing displays of a graphene interferometric modulator.

Certainly, it cannot be claimed that the picture of a small (5, 5)NGr molecule in Fig. 28 is a model of the observed micrometer ripples or bubbles, but it does demonstrate general trends that may have a place in bubbles, wrinkles, and other elements of the disturbed planar graphene structure. Simultaneously, the suggested explanation has a purely chemical character linking an enhanced correlation of p_z-electrons with C = C bond tension. But graphene is equally remarkable for the beautiful physical explanation of static deformations and the possibility of relating them to peculiarities in the band spectrum of its crystal. Happily, some 20 years ago, Kane and Mele [158] introduced a uniform gauge field in the effective mass band theory to describe homogeneous deformation of the crystal lattice.

Later on, the gauge invariance concept was extended to local deformations [159] and introduced into the quasirelativistic picture of the graphene electronic spectrum. Graphene deformation was described as a result of pseudospin polarization in the pseudomagnetic (gauge) field [159, 160]. Based on the graphene quasirelativistic theory and using the tight binding approximation, graphene static deformation can be described quantitatively to the best advantage as in a recent publication by K Novoselov's group [161]. Their results are presented in Fig. 29. The subject of this experimental study was monolayer graphene placed on a quartz substrate. Van der Waals forces arising between the tungsten needle of the scanning tunneling microscope (STM) and the graphene surface induced local Gaussian swelling of graphene at the contact site in the form of a bright spot. Theoretically, pseudospin polarization in a pseudomagnetic gauge field causes irregularities in the electron density distribution in the domain of deformation, represented by two three-sheet distributions shown on the graphene surface and calculated in the tight binding approximation. This three-flake distribution is quite apparent during scanning and fairly well agrees with calculated data.

At first site, the terminologies of the chemical and physical descriptions of graphene local static deformation seem different. Nonetheless, the descriptions are closely interrelated due to the common basic emergent elements of the two approaches; namely, pseudospins (physical approach) and effectively unpaired electrons (chemical approach). Virtual graphene pseudospins are actually quite real and represent local spins localized on carbon atoms and determining exclusive ferromagnetic properties of graphene (see Section 3.3). These local spins, in turn, are due to effectively unpaired electrons responsible for nonzero spin density on the carbon atoms of open-shell molecules, to which graphene belongs. In other words, both approaches to the description of static graphene deformations, viz. estranged virtual physical and atomistic chemical ones, are in excellent agreement and complement each other.

4.2.4 Enhancement of graphene magnetism and chemical activity in response to deformation. Continuing the descrip-

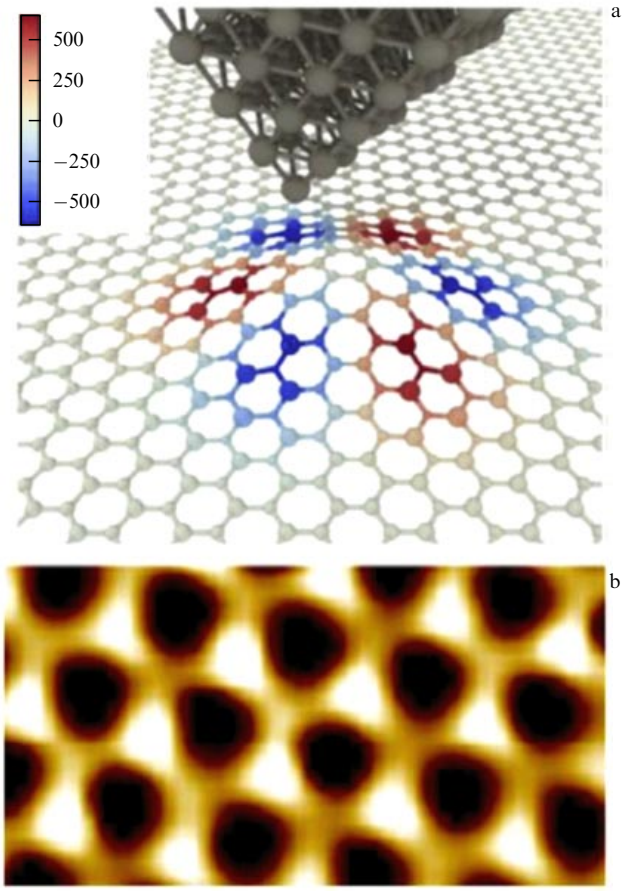

Figure 29. (a) Deformation in the form of Gaussian distribution induced on graphene by an STM tungsten needle under the effect of van der Waals forces (molecular dynamic calculations for a graphene layer on an SiO_2 substrate). (b) STM image of a graphene monolayer on SiO_2 in the direct current regime at $T = 6$ K (adapted from Ref. [161]).

tion of graphene deformation in terms of the atomistic approach, we call once again attention to the fact that the enhancement of graphene chemical activity and diminishing of the magnetic constant are characteristic emergent features of corrugated graphene. The former is related to the swelling of the planar structure due to an increased number of effectively unpaired electrons and, accordingly, of electron density at sites of maximum C=C bond stretching, such as the vertices of the circular and prismatic bubble domes present on STM, TEM (transmission electron microscope), and AFM images similar to those in Fig. 28, or ripples in Fig. 30a. The marked reduction in magnetic constants caused by deformation suggests a peculiar magnetic behavior of deformed graphene segments, depending on their size and curvature; this behavior contributes to the generation of a magnetic response localized in the corrugated region. Such a response has recently been reported in paper [162].

Figure 30b shows molecular magnets $[Fe_4(L)_2(dpm)_6]$ engrafted in ripple vertices on a graphene sheet. 'Rippling' causes a very apparent opening of the bandgap in the electronic spectrum of graphene and a sharp decrease in spin relaxation. The authors attribute this effect to the quantum spin dynamics of the magnets modulated by the graphene medium due to association of magnet spins with graphene phonons and/or quasispins of Dirac fermions. Nevertheless, stretched C=C bonds in the ripples markedly increase local

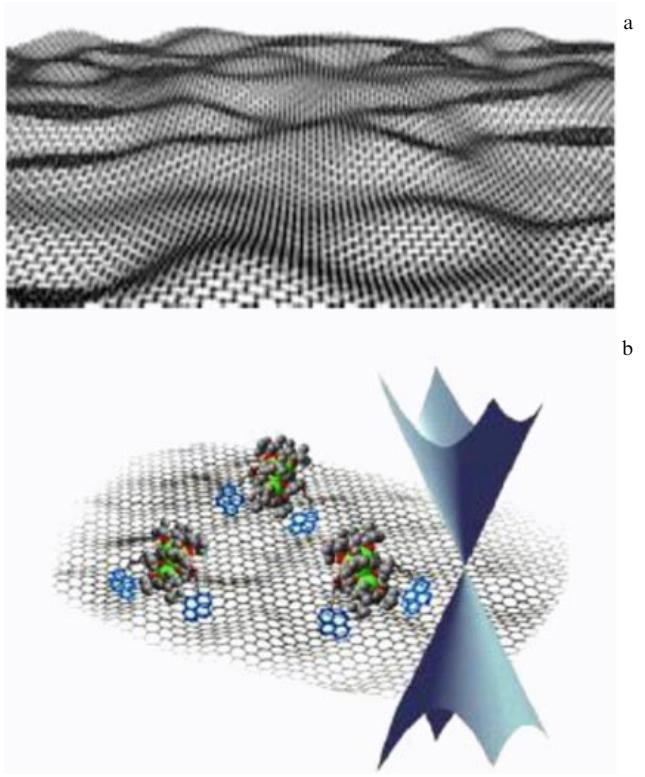

Figure 30. (a) Picture of a sheet of corrugated graphene (drawn by J C Meyer; see paper [157]). (b) View of a graphene sheet with engrafted molecular complexes $[Fe_4(L)_2(dpm)_6]$ [162]. (Adapted from Ref. [162].)

spin density (local spins), thereby contributing to effective spin–spin interaction between the magnets and graphene. The role of local spins of sp^2 nanocarbons in magnetic phenomena has been discussed many times with reference to diaparamagnetism of a C_{60} molecule in the crystalline matrix [84], and diaferromagnetism of graphene (see Section 3.3).

Today, the specific chemistry of rippled graphene sheets is being fairly well explored. The problem can be divided into two parts embracing either irregular or regular rippled structures, depending on swelling type. The former case deals with a random distribution of the swellings over a freely suspended graphene sheet or over a sheet placed on a substrate with previously deposited and irregularly distributed nanoparticles. Numerous experiments demonstrated that the local density of electronic states in graphene is modulated in conformity with a swelling shape. Thus, Fig. 31 shows a typical nonuniform distribution of gold nanoparticles underneath a graphene overlayer [163]. Figure 31a presents an SiO_2 substrate coated with particles (below) partly covered with a graphene sheet (above). The zone marked by the white square in Fig. 31a is presented in Fig. 31b at a higher magnification. Scanning contours along lines *1* and *2* are plotted in Fig. 31c. A comparison of the contours with scanning directions shows that the peak of contour *1* corresponds to a gold nanoparticle, whereas the analogous peaks of contour *2* indicate the presence of nanoparticles under the graphene sheet. The dip between the peaks in contour *2* is the region between two nanoparticles on a graphene sheet suspended more than 10 nm above the SiO_2 substrate. Thus, contour *2* is actually the distribution diagram of graphene stretched on gold nanoparticles. This picture is characteristic of graphene on a substrate with preliminarily deposited nanoparticles of any type [164].

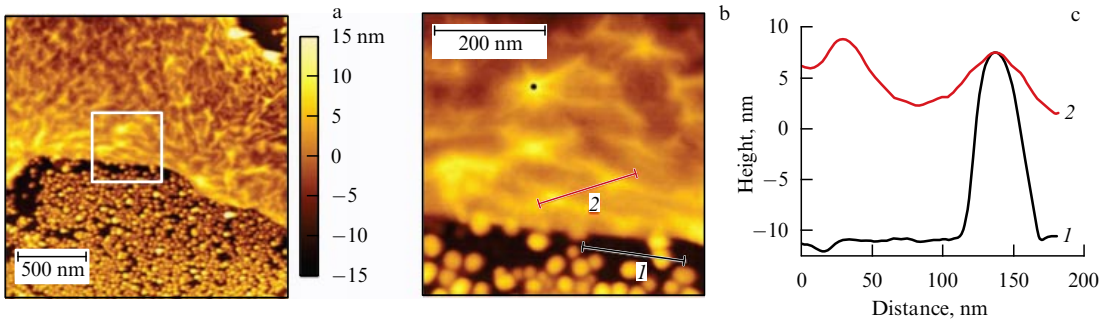

Figure 31. AFM image of graphene lying on Au nanoparticles covering a silicon dioxide substrate. (Adapted from Ref. [163].)

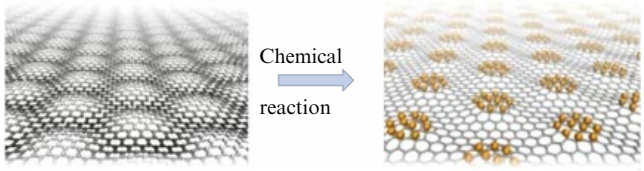

Figure 32. Schematic of a template chemical reactor on a regularly rippled graphene sheet.

Swellings of the second type in the form of a regular rippled structure of graphene can be obtained by at least two methods. One is the placement of graphene sheets on a matrix of regular structures, such as monoscale triangular pyramids formed in polydimethylsiloxane (PDMS) [165]. The other is based on moire structures characteristic of the monolayer adsorption of carbon atoms on metallic surfaces (see paper [100] and references cited therein). Due to the discrepancy between graphene and metal lattice constants, graphene sheets form an incommensurate phase which gives rise to a moire pattern and distorts the flat structure of initial graphene. Convex vertices become sites of enhanced chemical activity or preferable attachment of various chemical addends, turning moire graphene into a specific template reactor with spatially distributed chemical activity, as illustrated in Fig. 32. Another scenario for modeling such a reactor implies the regular distribution of metallic particles obtained by preliminary nanolithography or otherwise and covered by a graphene sheet.

Template graphene chemical reactors based on moire structures on Ru, Ir, Pt, or Ni substrates find wide applications. Figure 33 presents impressive results from L Hornekaer's group obtained in studies of the patterned hydrogenation of monolayer graphene grown on an Ir(111) substrate [98]. The figure shows that hydrogen clusters are adsorbed at prominences of the moire structure. The periodic character of this structure becomes increasingly more pronounced with prolongation of adsorption time. The Fourier transform of the image in Fig. 33e demonstrates conservation of moire

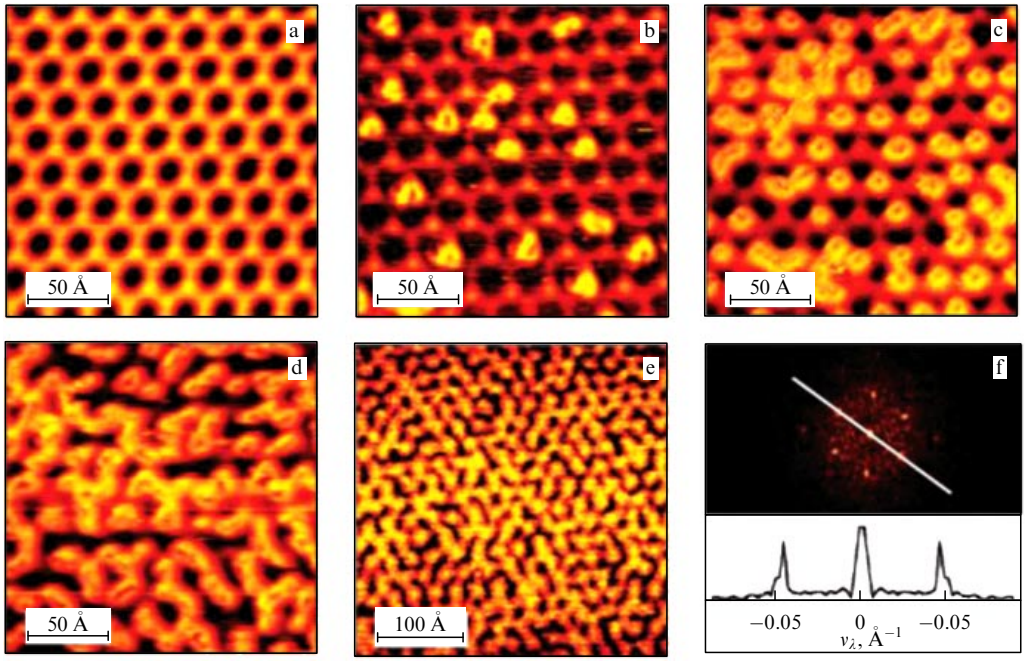

Figure 33. STM image of adsorbed hydrogen clusters reproducing and retaining the graphene moire structure on Ir(111). (a) Moire structure of pristine graphene on Ir(111). (b–e) The images of graphene treated with small amounts of atomic hydrogen for 15, 30, and 50 seconds, respectively. (f) Fourier transform of the image in figure (e). Inset to figure (f) shows the result of Fourier transformation along the specified line. Peaks are separated by a 21.5-Å distance in real space, confirming the periodicity of the moire supercell [98].

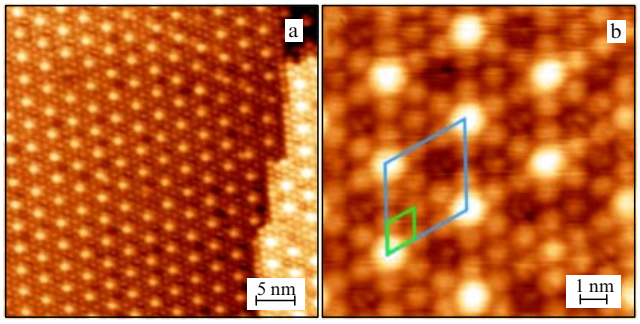

Figure 34. (a) Large-scale STM topography of C_{60} molecule layer growth on a graphene/Ru(0001) interface (STM — scanning tunneling microscope). The right panel shows a high terrace on the Ru(0001) surface. (b) Magnified image of a supramolecular structure. Unit cells of the substrate and molecular lattice are denoted by large and small diamonds, respectively. (Adapted from Ref. [167].)

periodicity of hydrogen adsorption in the case of its total saturation. Oxidation of graphene samples on Ir(111) and Pt(111) substrates [166] is, on the whole, analogous to hydrogenation described above, with minor differences in details due to a more complicated mechanism underlying the associated chemical reactions (see paper [47]).

There is little doubt that regularly corrugated graphene will be frequently used in the future as a template reactor, putting into effect the deformational emergentness of graphene and providing a basis for an in-depth investigation into its specific chemical properties. Promising characteristics of this material manifest themselves not only in the above hydrogenation and oxidation reactions, but also in such complicated process as the assembly of a C_{60} monolayer. Figure 34 presents monolayer graphene epitaxially grown on an Ru(0001) surface [167]. It indicates that deposition of C_{60} molecules on the interface obeys a certain growth regime giving rise to a supramolecular structure with a practically ideal periodic moire pattern with only a few defects. Weak interaction between the layer of C_{60} molecules and the substrate is nevertheless sufficient to control C_{60} adsorption. Conversely, the interaction of molecules with a flat graphene sheet is so weak that it does not prevent the molecules being adsorbed from sliding freely over its surface [168] (see Ref. [169] for a detailed discussion). This fact reveals the increasing role of the corrugated structure of template reactors.

Certainly, C_{60} is not the only example of control of the formation of supramolecular structures by the template graphene/5d-metal interface, which opens up the possibility of producing analogous structures based on other molecules. As this review was being prepared for submission to publishers, the first attempt was reported to quantitatively describe a template interface composed of a corrugated flat graphene sheet and underlying mono-sized silicon dioxide nanoparticles [170]. Figure 35 presents the results obtained by computation in the molecular dynamics approximation. The main conclusion from this work is that both stress and the force applied to graphene/particle contacts depend on the particle size (see Fig. 35a).

The results of these and many other experiments are, as a rule, subjected to computational treatment. This part of the work has an essentially general character [171, 172] as a calculation of model configurations in the framework of the reductionist concept with the employment of DFT computational schemes related to the adsorbate–graphene–substrate

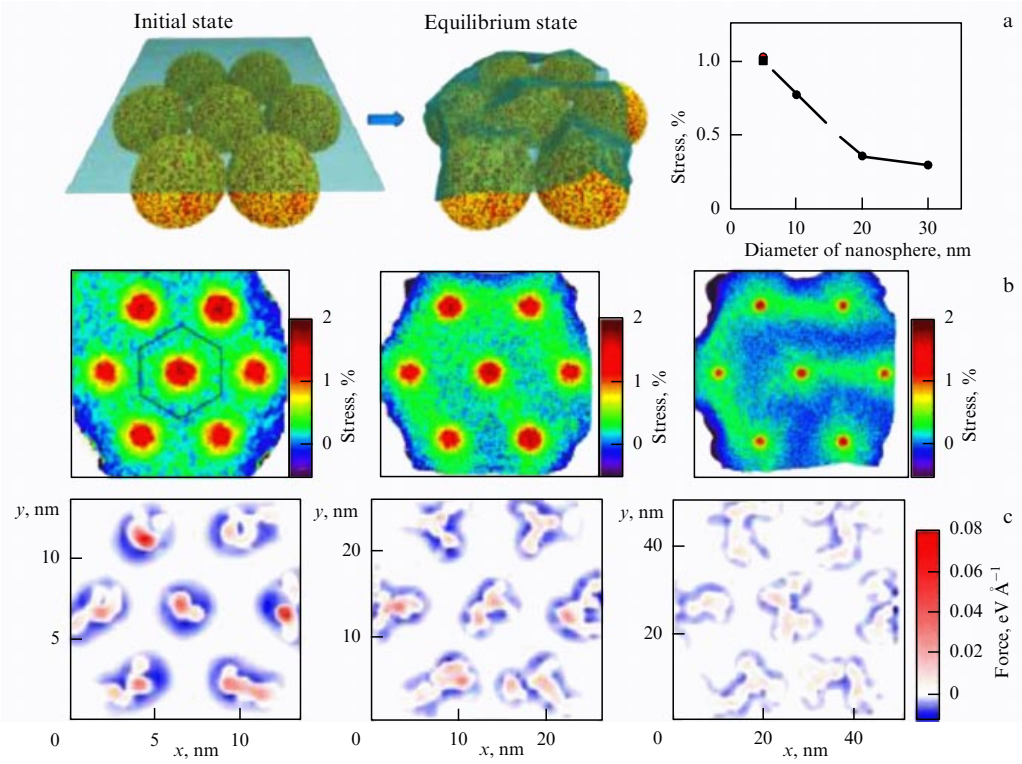

Figure 35. (a) Diagrammatic representation of the formation of corrugated graphene on the population of mono-sized quartz particles and the dependence of averaged tensile stress on nanoparticle diameter. Profiles of stress (b) and applied force (c) in corrugated graphene on a set of particles 5, 10, and 20 nm in diameter (from left to right). Calculations were done in molecular dynamics approximation. (Adapted from Ref. [170].)

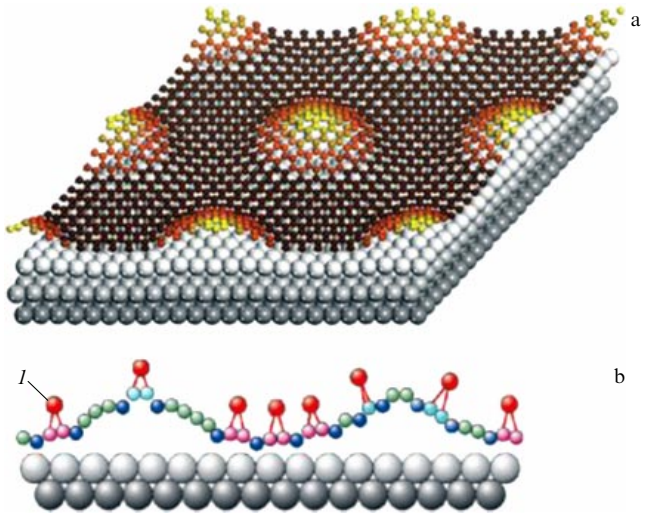

Figure 36. (Color online.) (a) Model of the 3D graphene unit cell structure on Ru(0001). For a clearer picture, vertical shifts in C and Ru atoms are magnified 3 and 7 times, respectively [173]. (b) Formation scheme of an epoxy cell in the course of oxidation of a graphene convex moire structure. Red balls (*1*) mark oxygen atoms. (Adapted from Refs [174] (a) and [173] (b), respectively.)

system of interest. The procedure for such a calculation is described in detail in paper [173] and illustrated by Fig. 36. The primary task covers modeling of a corrugated graphene monolayer. That presented in Fig. 36a shows graphene grown on an Ru(0001) substrate [174]. The model is chosen so as to ensure the best reproduction of the available structural data derived in this case from low-energy electron diffraction (LEED).

Modeling is a time-consuming procedure, but the relatively low computational cost for calculating model systems due to the application of standard DFT instruments makes it possible to evaluate the stability and electron properties of graphene objects differing in the degree of stretching and corrugation. Once this stage is completed, it is time to model the chemical modification of corrugated graphene. Most typical structures are obtained by gradual hydrogenation, oxidation, fullerenation, etc., imitating the effects of a respective adsorbate. This stage is usually considered in terms of DFT theory, too. Chemical adsorbates (oxygen atoms in the case presented in Fig. 36b) are manually disposed at different sites, with stability and structural and electronic properties being estimated based on the available experimental data [166].

As a rule, the dependence of adsorbate binding energy on the position of a given point in the graphene structure is explained in terms of carbon site pyramidalization at swellings, which enhances chemical activity [175, 176]). However, this is not necessarily true. To recall, corrugated graphene is an intrinsically open-shell object undergoing further radicalization with respect to pristine graphene due to the stretching of its C=C bonds at the sites occupied by swellings (see Fig. 28). For this reason, DFT-based computational instruments disregarding the specific character of graphene electronic states are not quite suitable for describing its interaction with chemical addends (see Section 2.3 for a detailed discussion of this issue). Therefore, the spin molecular theory of graphene appears to be a more adequate approximation for the purpose.

4.3 Uniaxial stretching of graphene

4.3.1 Background. Apart from bubbles, wrinkles, ripples, dimples, and other stable solid-state defects in which static deformation manifests itself, graphene can undergo deformation in a dynamic regime imposed by an external load. Usually, the mechanical properties of graphene are investigated in the dynamic deformation regime by fixing the sample response to an external impact. The examination of graphene's mechanical properties encounters difficulties and is usually reduced to a limited number of attempts (see reviews [151, 177–183] and references cited therein). The primary procedure covers nanoindented deflection of the sample in the air. Graphene can also be loaded by transferring axial thrust in polymeric rods onto intrinsic or introduced flakes. In several experiments, graphene deposited on various substrates was subjected to stretching (including uniaxial stretching). In all cases, the deformation picture was fairly complicated and highly depended on loading and environmental conditions.

Computational studies, unlike empirical investigations, are published in the hundreds [151]. Two solid-state approaches (continual and atomistic) have been formulated. The former is based on the elasticity theory of solids applied to macroscopic objects in the form of carcasses, plates, beams, rods, bars, and other structural elements of the continual description model. In this approach, the honeycomb structure of graphene is presented in terms of the above elements.

The primary objective of computations is to represent the total energy of the atomic–molecular nanocarbon system undergoing shape changes in terms of the above structural elements. In essence, this procedure includes adaptation of the elasticity theory of solids to nano-sized objects to enable a description of the mechanical properties of nano-objects with reference to such macroscopic mechanical parameters as Young's modulus (E), the Poisson coefficient (ν), and potential deformation energy (E_S). Because the energy of such objects is usually calculated with the use of modern computational methods, taking into consideration the atomic structure of an object (Monte Carlo method, molecular dynamics, quantum chemistry), the main challenge for the continual approach consists in the elucidation of the relationship between the unit cell molecular structure of a graphene crystal and its continual structural elements. Nanoscale continual methods (see papers [184–188] and references cited therein), including the most thoroughly developed ones based on the structural mechanics concept [189], proved rather efficient for modeling nanostructured materials. From the standpoint of structural mechanics, nanographenes are carcass structures with chemical C $\sim$ C bonds in the form of load-bearing rods and their junction points modelled by individual atoms [190–192].

The basic concept behind the atomistic approach is elucidation of the mechanical parameters of the object of interest by the direct solution of Newton's equations of motion [193] or the Schrödinger equation [194–196] in relation to the unit cell changing its shape in accordance with a given algorithm determining the relevant type of deformation. In this case, the forces acting on the atoms, rather than energy, make up the main target of computations. These forces are then introduced into relations of macroscopic linear theory of elasticity and provide a basis for calculating micro- and macroscopic parameters, such as Young's modulus (E^*) and the Poisson coefficient (ν^*). To recall, parameters E and ν in the atomistic approach differ

from E^* and v^* in the continual one, and their coincidence, if any, is merely accidental. From the practical standpoint, the time-consuming atomistic approach is inferior to the continual one and finds limited application to small objects. Nonetheless, it has some unquestionable advantages allowing a comprehensive description to be obtained of both the object's mechanical behavior under a given load (shape alteration) and the deformation/destruction picture of the object at the atomic level [178].

A conceptually important component in the development of the atomistic approach, whose physical aspect is described in a preceding paragraph, is representation of graphene deformation as a mechanochemical reaction [197–200]. As shown in Section 4.2.1, the similarity between a mechanically induced reaction and the standard chemical reaction was noticed for the first time by Tobolsky and Eyring over 60 years ago [155]. Their observation has recently been revised by Morokuma et al. [201]. As a result, it was proposed away back in 1995 to use the well-developed quantum-mechanochemical reaction coordinate (QMCRC) approach [202] to study transformation of the atomic structure under the effect of deformation of molecular compounds with covalent bonds [203]. This approach, representing the molecular aspect of general atomistic consideration of mechanical deformation, was applied for the first time to quantitatively describe deformation of polydimethylsiloxane oligomers [204]; it proved highly efficient and allowed elucidating the mechanism of disintegration and rupture of the polymers at the atomic level. When applied to graphene, the QMCRC approach demonstrated new possibilities for its implementation due to the involvement of spin molecular theory [19]. This approach implies the abandonment of the unit cell concept with the imposed periodic boundary conditions and the passage to nanographene as a molecule with covalent bonds. Comprehensive analysis of the results presented in the following sections reveals new aspects of the theoretical consideration of graphene deformation, remaining in the shadow of its continual and atomistic mechanophysics.

4.3.2 Mechanochemical internal coordinates and basic mechanical parameters. The QMCRC approach is intended for the quantitative description of deformation, destruction, and rupture of a molecule with covalent bonds. It is implemented based on the introduction of mechanochemical internal (MCI) coordinates as the reaction coordinates. The choice of the necessary MCI coordinate system depends on the general architectonics of the standard quantum-chemical programming support for which calculation of the force, namely total energy gradient, is the main procedure. Therefore, MCI coordinates must meet the following requirements.

(1) Each MCI coordinate is a classification characteristic of the deformation mode in terms of internal molecular coordinates: uniaxial stretching and contraction are described by linear MCI coordinates analogous to valence bonds, bending by the MCI coordinate analogous to the valence angle, and twisting by the MCI coordinate analogous to the torsion angle. MCI coordinates thus introduced are microscopic analogs of macroscopic beam elements in structural mechanics [189].

(2) In the course of quantum-chemical calculations, MCI coordinates related to a certain deformation mode are excluded from the optimization procedure in determining total energy minimum.

(3) The response strength is defined as the sum of residual total energy gradients (partial forces) over all other MCI coordinates.

Partial forces F_i found in this way can be used at a later time in calculating necessary micro- and macroscopic mechanical parameters, among which the following ones characterize uniaxial stretching:

$$\text{response strength } F\text{:}\quad F=\sum_i F_i\,, \tag{13}$$

$$\text{stress } \sigma\text{:}\quad \sigma=\frac{F}{S}=\frac{\sum_i F_i}{S}\,, \tag{14}$$

$$\text{Young's modulus } E^*\text{:}\quad E^*=\frac{\sigma}{\varepsilon}\,, \tag{15}$$

$$\text{Stiffness coefficient } k^*\text{:}\quad k^*=\frac{F}{\Delta L_i}\,. \tag{16}$$

Here, S is the loaded area, $\varepsilon=\Delta L_i/L_0$ is the relative lengthening, and ΔL_i is the lengthening of the ith MCI coordinate, equal for all MCI coordinates in a given experiment. The completed computational cycle provides the researcher with *microscopic characteristics* that include such data:

(1) Equilibrium atomic structures of the loaded sheet at each deformation step, including of C ~ C-bond lengthening and breaking, as well as post-breaking relaxation.

(2) Deformation energy

$$E_{\rm S}(\varepsilon)=E_{\rm tot}(\varepsilon)-E_{\rm tot}(0)\,, \tag{17}$$

where $E_{\rm tot}(0)$ and $E_{\rm tot}(\varepsilon)$ are total energies of unloaded and stretched specimens, respectively.

(3) Partial F_i and total F [Eqn (13)] strengths of response.

(4) Molecular and atomic chemical susceptibility of the sample, expressed in terms of the total $N_{\rm D}$ and partial $N_{\rm DA}$ numbers of effectively unpaired electrons (see Ref. [17] for a detailed description of these parameters).

The dependences of energy, strength, stress, $N_{\rm D}$, and $N_{\rm DA}$ on the total and relative lengthening characterize the mechanical behavior of an object at each stage of deformation at the atomic level. The last two parameters are chemical emergents showing changes in the chemical activity of the sample's spin properties during deformation.

Micro- and macroscopic characteristics include elastic mechanical parameters E^* and k^* [Eqns (15) and (16)] analogous to the respective parameters in the theory of elasticity; they are determined in the linear region of the relative lengthening dependence of stress.

4.3.3 Graphene as an object of dynamic deformation. From the physical (and mechanophysical) point of view, graphene is a two-dimensional crystal with a two-atom unit cell. The role of hexagonal packing in the graphene honeycomb structure arises from the peculiar properties of its electronic spectrum similar to the Dirac fermion spectrum with its Dirac cones and zero bandgap [62]. From the chemical (molecular) standpoint, graphene is a set of condensed benzenoid units formed by carbon atoms in the sp^2 electron configuration. Graphene mechanophysics usually considers benzenoid elements as totally isotropic by virtue of their high D_{6h} symmetry and confines itself in determining their mechanical properties to a description of the unit cell [184–193].

Graphene mechanochemistry was from the very beginning focused on benzenoid units and formulated the problem of graphene mechanical properties taking account of its benzenoid structure.

This poses two questions: What are the mechanical properties of the benzenoid unit of a honeycomb structure, and Does the packing of benzenoid structural elements influence the mechanical properties of graphene as a condensed structure? These questions arise from the fact that mechanical isotropicity is not a direct consequence of the structural symmetry of the benzenoid unit, because destruction of an object is associated with the breaking of concrete chemical bonds, the choice of which is determined by the geometry of the applied load. Evidently, the sets of chemical bonds thus chosen for an individual benzenoid unit and the set of the units on the honeycomb structure network are substantially different for deformation in different directions. Therefore, a well-pronounced anisotropy of graphene mechanical properties should be expected. It is convenient to begin a detailed consideration with the uniaxial stretching of a benzene molecule.

4.3.4 Tensile strain and rupture of the benzene molecule. Considering the mechanochemical reaction of deformation of a benzene molecule subjected to uniaxial stretching allows not only answering the above questions but also demonstrating the practical application of the QMCRC algorithm [197–199]. The upper panel of Fig. 37 represents two pairs of orthogonal MCI coordinates restricting the region of possible angles of mutual orientation of coordinates or directions of load application. Two chosen orientations correspond to deformation along C ~ C bonds (zg-mode) and normally to them (ach-mode). In accordance with the QMCRC algorithm, deformation of a molecule occurs as a stepwise lengthening of each pair of MCI coordinates with the increment $\Delta L = 0.05$ Å at each step; as a result, the length of the MCI coordinates is $L = L_0 + n\Delta L$, where L_0 is their initial length, and n is the number of deformation steps.

Figure 37a, b presents graphical dependences $(F - \Delta L)$ (a) and $(N_D - \Delta L)$ (b) related to two deformation modes: ach and zg. The total response strength and the total number of effectively unpaired electrons N_D are the main microscopic characteristics of a mechanochemical reaction, deduced directly from calculations and providing the quantitative characteristic of deformation and destruction of a benzene molecule [197, 199]. Figure 37 gives evidence that the mechanical behavior of the molecule is strongly anisotropic. Graphs $(F - \Delta L)$ in Fig. 37a are different for the two modes at both the initial and concluding steps of deformation. The linear elastic behavior is apparent only at the first steps. The $(N_D - \Delta L)$ dependence in Fig. 37b illustrates an even more radical difference, suggesting different electronic processes accompanying molecular destruction. It means that zg- and ach-modes of benzene molecule stretching occur as different mechanochemical reactions. These peculiarities appear to be related to the difference between MCI coordinates, depending on the load direction responsible for the formation of different molecular fragments after destruction. The structural transformations in a benzene molecule will be considered in Section 4.4.5.

Apart from the differences in the microscopic behavior, the two above modes are characterized by different mechanical parameters, shown in Table 2, giving evidence of high mechanical anisotropy of benzene molecules with respect to the direction of load application. Of special interest are the large values of both (related to ach and zg modes) Young's moduli (on the order of 1 TPa). It is hardly appropriate to apply this term to an individual molecule. However, it formally characterizes the linear part of the $(\sigma - \varepsilon)$ dependence and suggests an extremely high strength of the molecule. Clearly, the values of E^* obtained are directly related to Young's modulus of graphene crystals.

4.3.5 Tensile strain and rupture of the nanographene (5, 5)NGr molecule. It can be assumed, taking into consideration the mechanical anisotropy of benzenoid units, that deformation

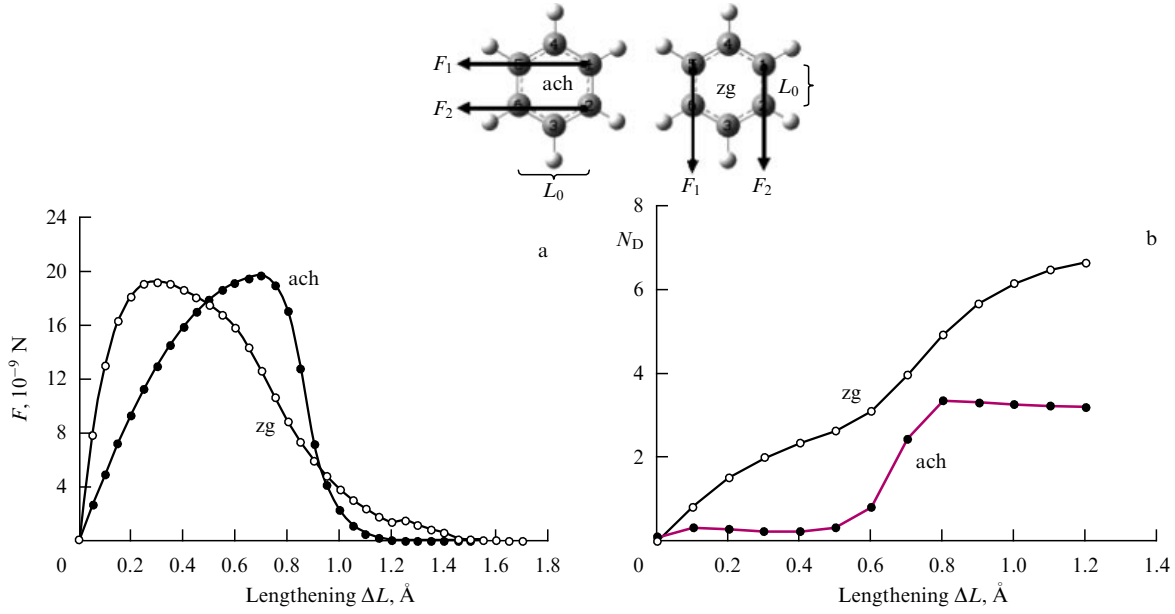

Figure 37. Set of two pairs of mechanochemical internal coordinates of uniaxial stretching of a benzene molecule for deformation modes ach and zg. F_1 and F_2 are the respective response strengths. Graphical dependences $(F - \Delta L)$ (a) and $(N_D - \Delta L)$ (b) for ach- and zg-deformation modes of a benzene molecule [197, 199].

Table 2. Micro(macro)scopic mechanical characteristics of benzene and (5, 5) nanographene molecules obtained in the QMCRC approximation [197–199].

Molecules	Modes	ε_{cr}	F_{cr}, 10^{-9} N	σ_{cr}, 10^{9} N m^{-2}	E^{*}, TPa
Benzene	ach	0.29	19.62	120.47	0.76
	zg	0.22	19.18	97.13	0.99
ach-cyclohexane	ach	0.44	15.69	93.76	0.4
	zg	0.36	14.99	74.57	0.74
(5, 5)NGr	ach	0.16	5.09	110.04	1.05
	zg	0.15	45.53	101.20	1.06
(5, 5)NGr-H1	ach	0.18	54.56	119.85	1.09
	zg	0.14	47.99	106.66	1.15
(5, 5)NGr-H2	ach	0.20	50.35	111.17	0.92
	zg	0.14	47.07	103.12	0.95
(5, 5)NGra	ach	0.3	43.41	74.37	0.61
	zg	0.23	36.09	63.24	0.57

* Experimental values of Young's moduli are ~ 1 TPa [180, 205].

of the regular honeycomb structure also depends on load orientation, for which the directions along zg and ach edges determine the limits of possible changes in load orientation with respect to C ~ C bond chains. These two limiting cases of a (5, 5)NGr molecule deformation are considered below [197, 198]. Configurations of MCI coordinates during molecule stretching for deformation ach and zg modes are depicted in Fig. 38a.

Tensile deformation mode ach. Figure 38b shows equilibrium structures of the (5, 5)NGr molecule for a sequence of deformation steps. The molecule is uniformly stretched during the first 14 steps, and breaks at the 15th step. The destruction is completed at step 17, and the final structure is analogous to that resulting from benzene deformation in the same mode; namely, the molecule divides into two fragments, one of which is a truncated (4, 5)NGr molecule, while the other is a polymerized chain of acetylene molecules transformed into a carbyne C ≡ C chain.

Tensile deformation mode zg. Notwithstanding the anticipated mechanical anisotropy, the results surpassed all expectations. Figure 39a presents a set of equilibrium structures of a deformed molecule, obtained at respective deformation steps and showing a surprising picture of unusual destruction of a nano-sized graphene sheet markedly different from its behavior in ach-mode deformation. The observed picture is described based on a simple analogy with the bursting of textile tricotage [197–199]. Indeed, the strength of a textile material and the manner of its rupture are known to depend on the direction of the applied stress and spatial loop packing configuration. In terms of this analogy, each benzenoid unit is a loop. In the case of the ach-mode, sheet disintegration begins from and ends in the destruction of a single loop row. In the zg-mode, destruction of one loop initiates destruction of others, giving rise to a lengthening monatomic chain of carbon atoms. Clearly, this difference in the mechanical behavior originates in benzenoid unit packing. Loop destruction in the ach-mode results from breaking

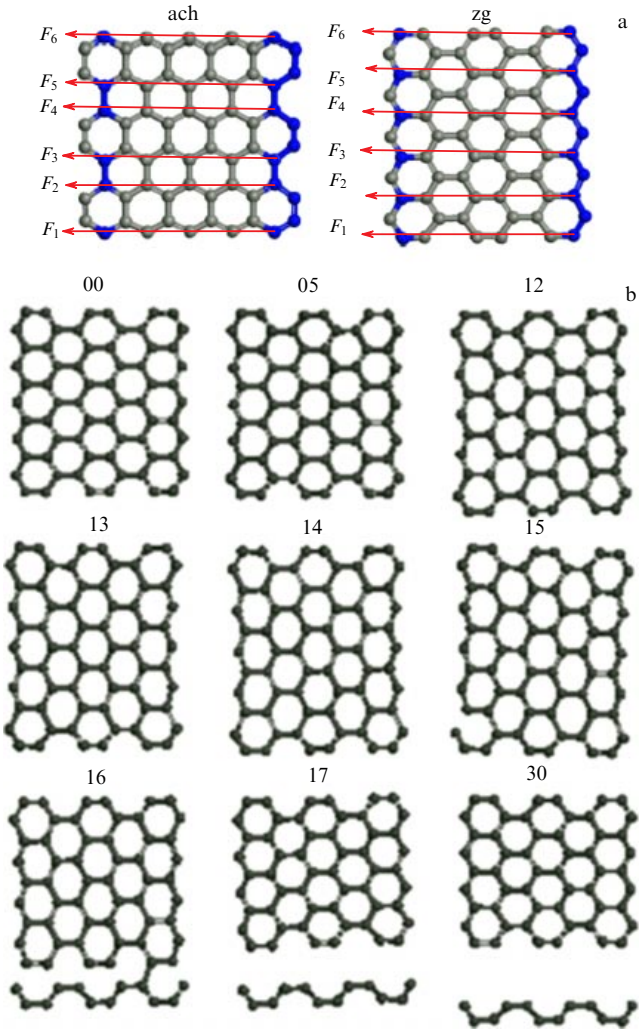

Figure 38. (a) Sets of six MCI coordinates of uniaxial stretching of the (5, 5)NGr molecule for deformation ach and zg modes; $F_{6\to1}$ are the respective response strengths. (b) Equilibrium structures of the molecule at stepwise ach-mode deformation. Numbers indicate deformation steps [197].

two C ~ C bonds within one benzenoid cycle, whereas the breaking of each of three C ~ C bonds in the zg-mode affects three cycles and thereby causes the destruction of a number of loops.

The difference between the structural patterns of two deformation modes naturally leads to a difference in quantitative microscopic characteristics of the mechanical behavior. Figures 40a, b plot $(F - \Delta L)$ dependences for the two deformation modes. In both cases, the behavior of the molecule at the first deformation step is analogous to that of a benzene molecule, because it is associated with the break of the first C = C bond. It follows from Table 2 that mechanical characteristics deduced from the data for the first deformation step are similar to those of the benzene molecule, which suggests the close relationship between the behaviors of a nano-sized graphene sheet and an individual benzenoid unit. At the same time, all micro- and macroscopic characteristics differ from those of benzene, which gives direct evidence of the influence exerted by the packing of benzenoid units in the sheet. Whereas ach-mode deformation proceeds as one-step and is completed at the 20th step, zg-mode deformation is multistep and continues up to the 250th step. The $(F - \Delta L)$

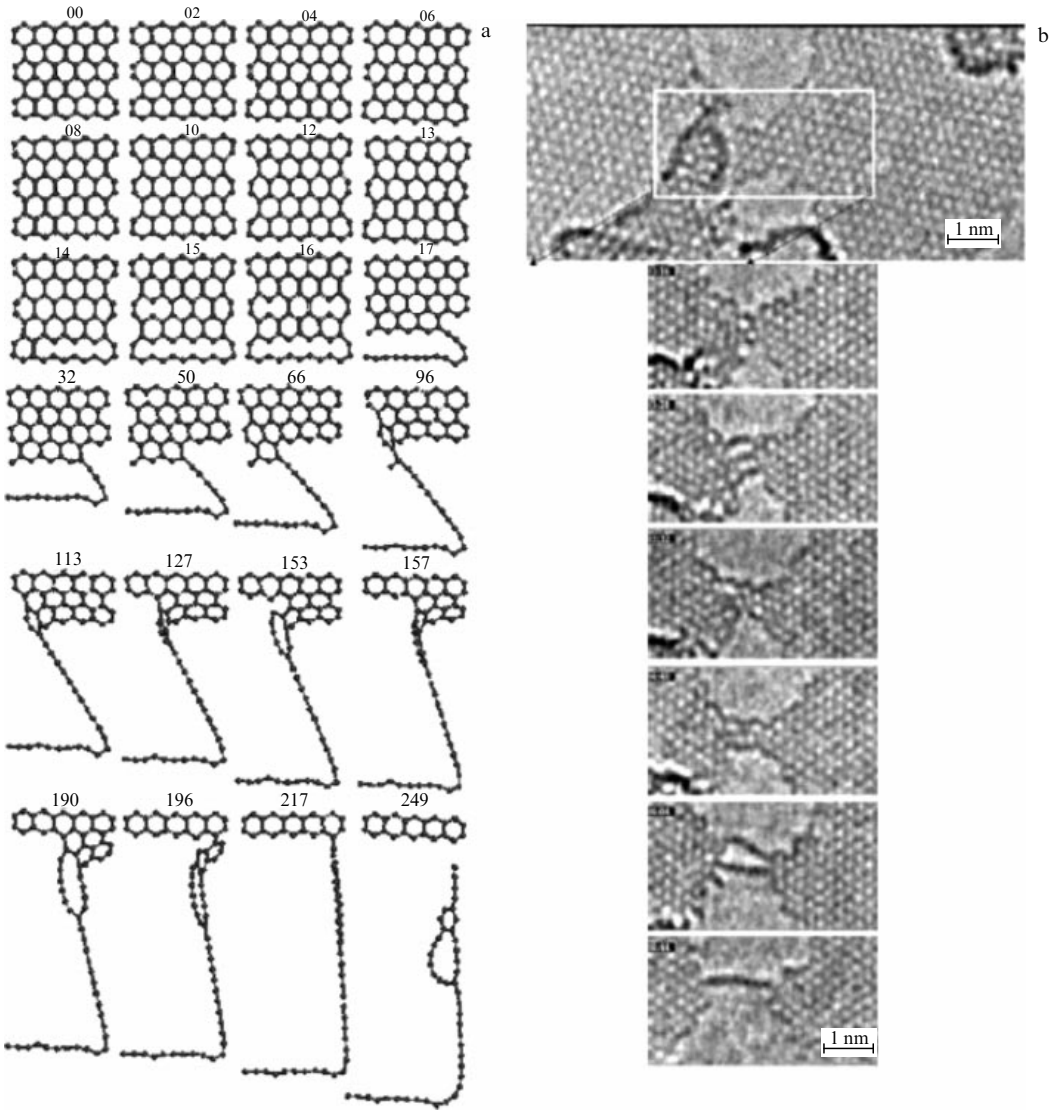

Figure 39. (a) Equilibrium structures of the (5, 5)NGr molecule during stepwise zg-mode deformation [197]. Figures enumerate deformation steps. (b) Formation of a chain of carbon atoms. (Adapted from Ref. [206].)

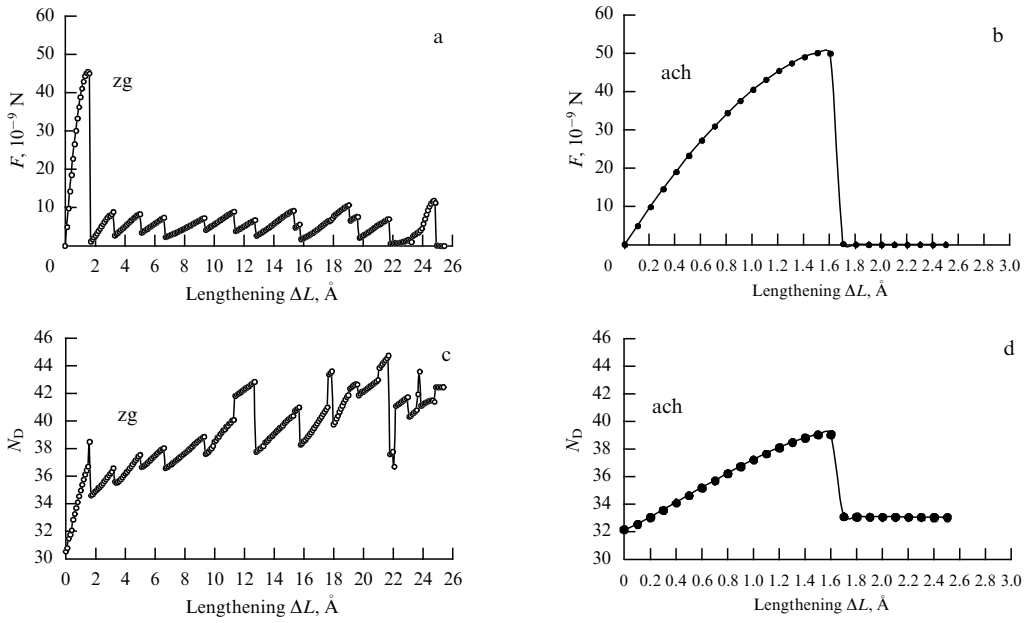

Figure 40. Graphical dependences ($F - \Delta L$) (a, b) and ($N_D - \Delta L$) (c, d) of a (5, 5)NGr molecule in the case of ach- and zg-mode deformation [197, 199].

dependence has a saw-tooth configuration, reflecting the consecutive loop destruction clearly seen in Fig. 39, which presents structures formed at deformation steps corresponding to the teeth maxima plotted in the $(F - \Delta L)$ graph. The rupture of nanographene is completed only after abstraction of a single-atom chain at the 249th step.

A similar formation of a characteristic monatomic chain in the zg-deformation mode was demonstrated by DFT calculations of a large supercell in the form of a graphene nanoribbon [193, 196]. Also, the marked anisotropy in the mechanical behavior of the graphene sheet was revealed by molecular dynamic calculations with the application of uniaxial stress gradually changing its direction from ach to zg of a honeycomb crystalline structure of graphene [207]. The tendency specific for the zg mode was observed in experiment [206].

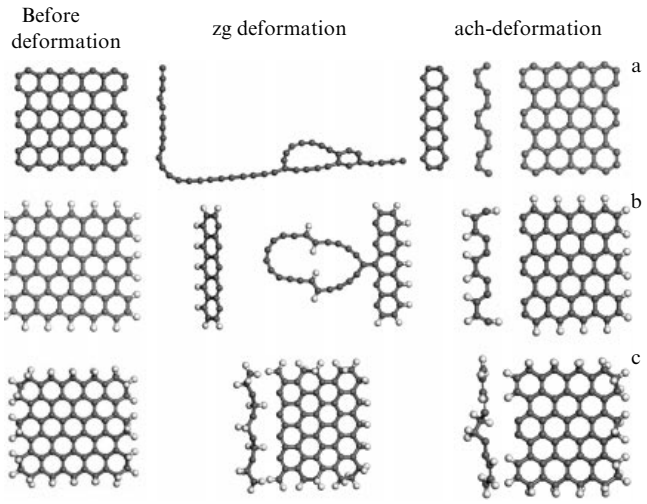

Figure 41. Equilibrium structures of (5, 5) nanographene before and after complete tensile strain in two deformation modes: (5, 5)NGr molecule (a); (5, 5)NGr-Hl molecule (b), and (5, 5)NGr-H2 molecule (c) [200].

Unlike an intact benzene molecule for which $N_D = 0$, the unstrained (5, 5)NGr molecule has a rather large initial N_D value amounting to 31 (see Table 1). Figures 40c, d reveal the additional influence of C ~ C bond lengthening caused by tensile strain on the number of effectively unpaired electrons. $(N_D - \Delta L)$ dependences give convincing evidence of the difference between mechanochemical reactions corresponding to ach and zg modes at the first deformation step. In the former case, the reaction stops after the 21st step, while it continues in the latter case, and the dependence $(N_D - \Delta L)$ assumes a saw-tooth shape similar to that of the $(F - \Delta L)$ dependence in Fig. 40a. Importantly, $(N_D - \Delta L)$ dependences reflect quantitative changes in emergent characteristics of the chemical reactivity of a nanographene sheet undergoing tensile strain.

4.3.6 Tensile strain of hydrogen-terminated (5, 5)NGr molecules. Figure 41 shows equilibrium structures of (5, 5)NGr, (5, 5)NGr-Hl, and (5, 5)NGr-H2 molecules differing in the state of edge atoms before and after uniaxial stretching, which ends in the break of the last C ~ C bond connecting two fragments of the molecule [200]. Two main peculiarities of molecular deformation are apparent. One is deformation anisotropy with respect to the two deformation modes. The other manifests itself as the strong dependence of deformation on the chemical composition of edge atoms in the molecule.

It follows from Fig. 41 that (5, 5)NGr exhibits the most complicated deformation behavior. Hydrogen atom attachment to each edge atom of (5, 5)NGr-Hl does not alter the general character of deformation; it remains tricotage-like and retains a significant difference between the behaviors in zg and ach deformation modes. The mechanical characteristics of the hydrogen-saturated molecule in Table 2 are similar to those of (5, 5)NGr, but the character of structural changes alters noticeably, and the number of steps in the zg deformation mode falls to 121 (see Fig. 42).

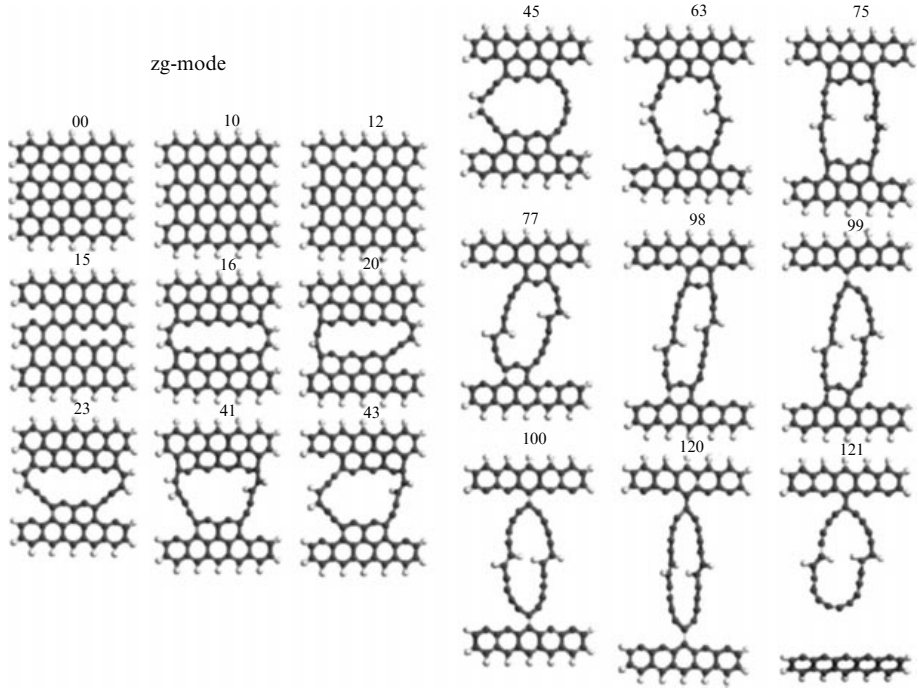

Figure 42. Equilibrium structures of a (5, 5)NGr-HI molecule forming in the course of stepwise zg-mode deformation [197]. Numbers indicate deformation steps.

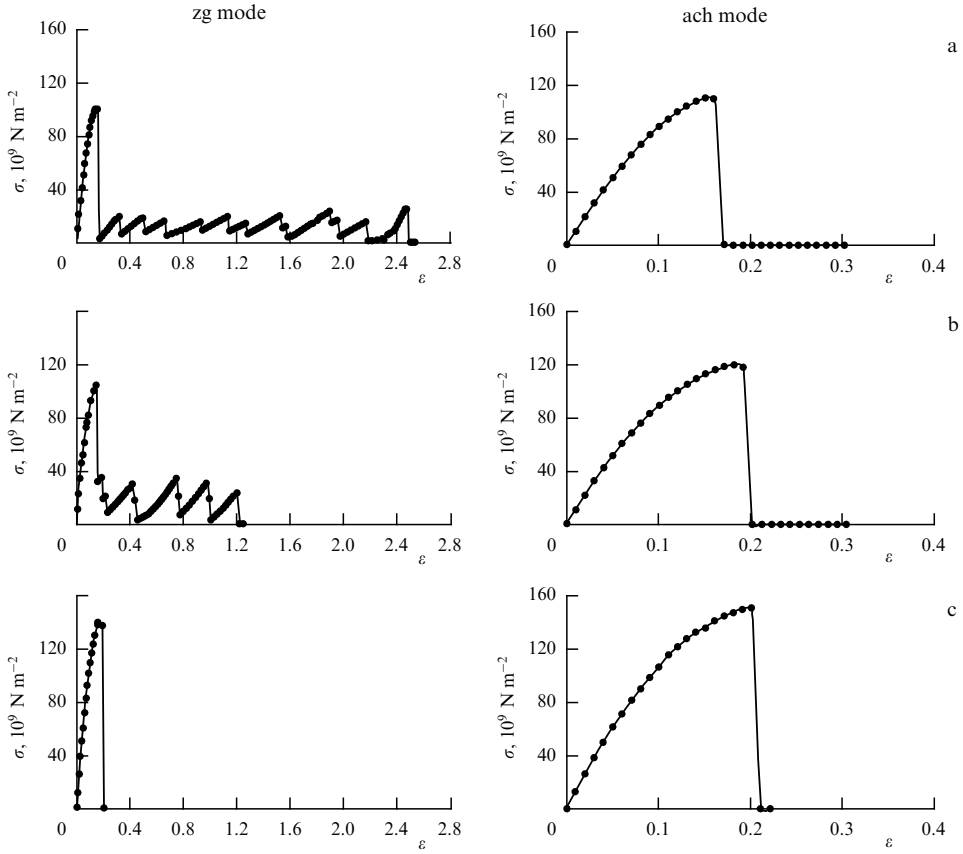

Figure 43. Graphical dependences ($\sigma - \varepsilon$) illustrating tensile strain of (5, 5) nanographene: (5, 5)NGr molecule (a), (5, 5)NGr-Hl molecule (b), and (5, 5)NGr-H2 molecule (c).

The addition of the second hydrogen atom to the edge atoms of (5, 5)NGr-H2 makes things utterly different: the ach mode remains quite traditional, whereas the zg mode becomes practically identical to the former one. The tricotage-like character of deformation totally disappears, and destruction occurs at the 20th step. Young's moduli decrease to 0.95 and 0.92 TPA for ach and zg modes, respectively. Figure 43 presents a set of ($\sigma - \varepsilon$) dependences emphasizing the differences among the mechanical behaviors of the three molecules. Table 2 summarizes these and experimental data.

Because deformation-induced distortion of molecules first and foremost affects basal plane atoms, such conspicuous alteration of their behavior under the effect of deformation suggests a strong influence of the chemical state of edge atoms on the electronic properties of their basal plane counterparts. This phenomenon is understandable under the assumptions that

(1) molecule deformation and destruction are a collective phenomenon involving the entire electron system;

(2) electron system of a graphene molecule is delocalized due to the strong correlation of odd p_z-electrons, as confirmed by the very high sensitivity of the behavior of unpaired electrons undergoing deformation to the chemical state of edge atoms, which is described by ($N_D - \Delta L$) dependences in Fig. 44;

(3) these two circumstances taken together arise from the emergent character of the mechanical process in graphene.

4.4 Uniaxial stretching of graphane

4.4.1 Introduction. The term 'graphane' refers to the only configuration with a regular structure [49] among fully hydrogenated graphenes, whose incomplete set of modifications is presented in Fig. 26c. This makes graphane one of the most intriguing representatives of the family of graphene polyderivatives and explains the great interest shown in it by the graphene community (see reviews [208, 209] and references cited therein). What is it that makes graphane so attractive to researchers? First, it is a product of the complete chemical modification of two-dimensional graphene, retaining the regular structure of the carbon skeleton in the form of a honeycomb network consisting of nonplanar cyclohexane cycles in the ach conformation, instead of flat benzenoid units. Second, there are experimental data suggesting the reality of graphane [48, 210], besides theoretical considerations prevalent in graphenics. Third, graphane is expected to show specific electronic, vibrational, and mechanical properties, such as bandgap opening and unique mechanical strength comparable with that of graphene.

An analysis of graphane's mechanical characteristics mainly focuses on the evaluation of the elastic properties of a 2D crystal in the framework of the isotropic continual elastic shell model [211–214]. Only authors of Refs [215–218] investigated the dependence of crystal behavior on its spatial configuration. Calculations in Refs [211–215] were performed using several versions of the DFT method in the unit cell approximation with periodic boundary conditions. The elastic parameters of solid-state graphane thus obtained agree with one another, but none of the computational techniques gave the answer as to how graphane deformation occurs and what the mechanism underlying its destruction is. The only source of information about the behavior of graphane upon destruction is molecular dynamics calculations made for a large graphane sheet [216].

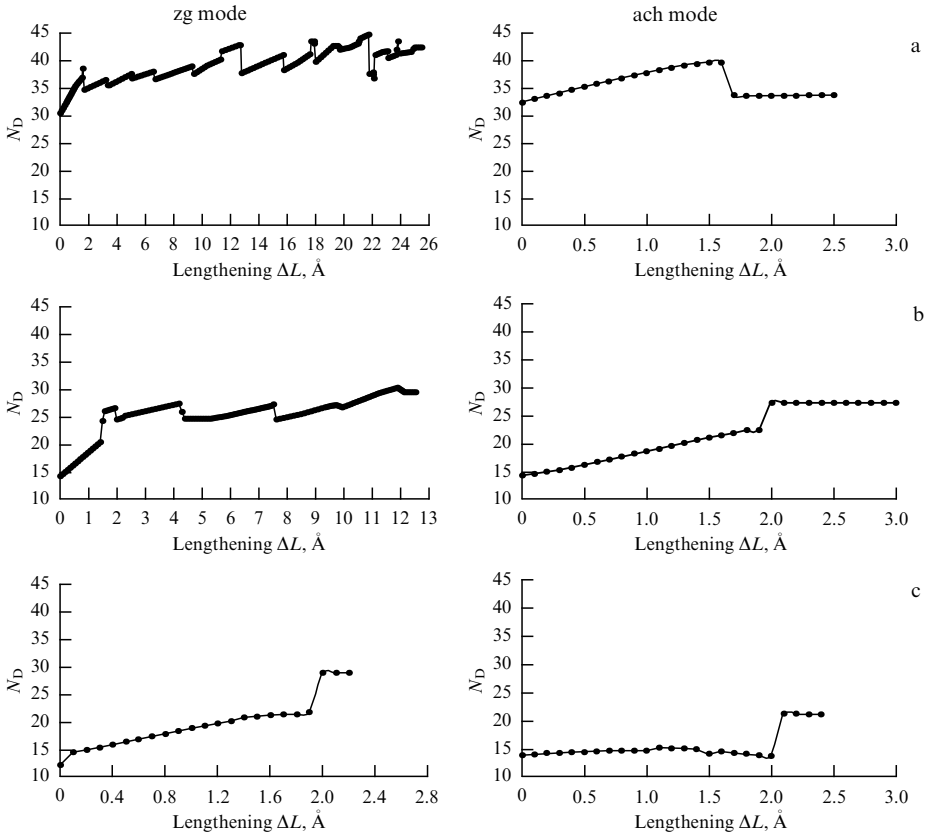

Figure 44. Evolution of atomic chemical activity during tensile strain of (5, 5)-nanographene in two deformation modes: (5, 5)NGr molecule (a), (5, 5)NGr-Hl molecule (b), and (5, 5)NGr-H2 molecule (c) [200].

These calculations demonstrated crack nucleation in the graphane sheet bulk, its gradual growth, and eventual disintegration suggesting an unusual mode of graphane destruction and the necessity of studying it in more detail in the framework of the atomistic theory. In this context, it is only natural that researchers gave special attention to the QMCRC approach based on the concept of the mechanochemical reaction as the main driving force of graphane tensile strain and destruction [197, 199]. As expected, the application of this approach in graphane research proved successful [217]. It was established that hydrogenation exerts a strong influence on the mechanical properties of graphene during its transformation into graphane. Its micro- and macroscopic characteristics, such as tensile strength, relative lengthening upon rupture, and Young's modulus, exhibited high sensitivity not only to chemical modification but also to structural deformation, the character of which changed dramatically as graphene benzenoid units were substituted by cyclohexanoid cycles of graphane. Results obtained in the framework of the QMCRC approach are overviewed below.

4.4.2 Graphane as an object of computational studies. A detailed study of stepwise graphene hydrogenation [46] showed that the ordered configuration of cyclohexanoids is not only retained after complete hydrogenation $(C_1H_1)_n$ but also energetically and topologically preferred in its graphane isomer formed by cyclohexanoids in the ach conformation. A (5, 5) nanographane molecule [hereinafter, (5, 5)NGra] representing this isomer is shown in Fig. 26c. It is this molecule that constituted the basic component of the QMCRC approach, which allowed its behavior under uniaxial stretching conditions to be studied [217].

It should be noted that the (5, 5)NGra molecule was obtained by stepwise hydrogenation of a (5, 5)NGr molecule [46], the mechanical properties of which are described in Section 4.3. Both the initial and hydrogenated molecules have a regular honeycomb structure formed by the equal number of carbon atoms. In other words, the two molecules are isostructural. However, sp^2 or sp^3 hybridization of the electronic structure of carbon atoms results in their different spatial disposition inside (5, 5)NGr and (5, 5)NGra skeletons. The identity of the carbon skeletons of the two molecules in terms of the number of constituent atoms and the difference in the structure of their basic elements create ideal conditions for a comparative study of the mechanical behavior of intact and modified graphene. In addition, it is possible to evaluate the influence of hydrogenation on the mechanical behavior of the objects, when it affects not only edge graphene atoms but also atoms localized in the basal plane. To avoid repetition of the discussion on the influence of hydrogenation on edge graphene atoms already presented in Section 4.3.6, further consideration will be confined to effects associated with basal plane atom hydrogenation in the (5, 5)NGr-H2 molecule that completes the formation of graphane (5, 5)NGra molecule [46].

4.4.3 Tensile strain and rupture of graphane (5, 5)NGra molecule. As in the case of graphene, work in the framework of the QMCRC approach begins with the introduction of MCI coordinates, two sets of which are presented for (5, 5)NGra in the upper panel of Fig. 45. Similar to the case of nanographene molecule, the MCI coordinates are directed

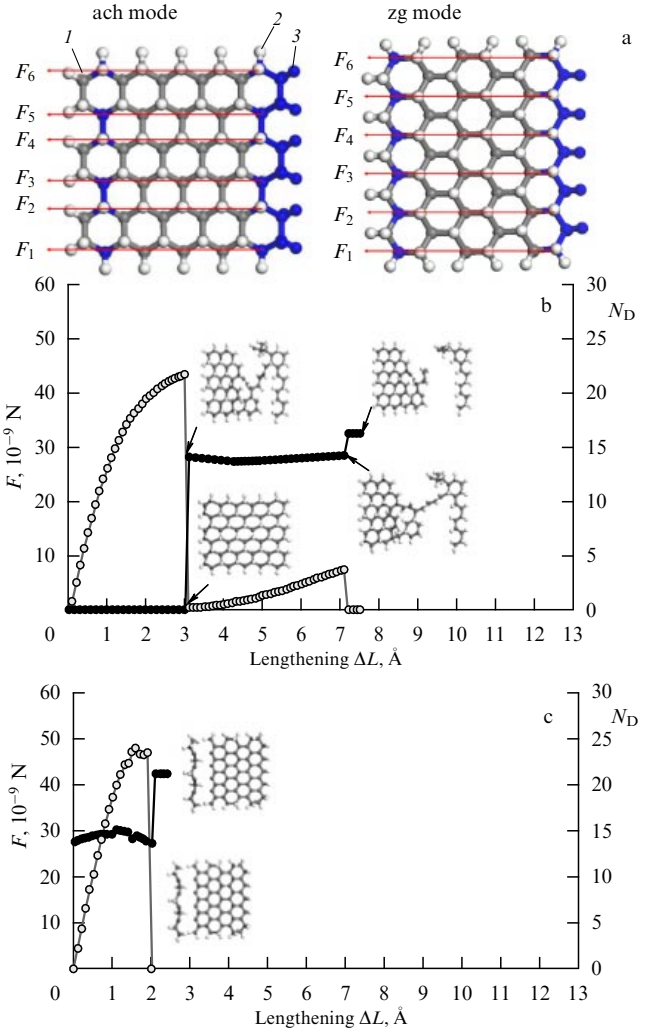

Figure 45. (Color online.) (a) Sets of six MCI coordinates of uniaxial (5, 5)NGra stretching in deformation ach and zg modes. Grey (*1*) and white (*2*) balls mark carbon and hydrogen atoms of the equilibrium molecule, respectively [185]. Edge carbon atoms are terminated by two hydrogen atoms. Blue color (*3*) marks atoms excluded from optimization process. Graphs $(F - \Delta L)$ (grey curves with dots, left axis) and $(N_D - \Delta L)$ (black curves with dots, right axis) correspond to deformation ach mode of (5, 5)NGra (structures at deformation steps 30, 31, 70, and 71) (b) and (5, 5)NGr-H2 (structures at deformation steps 20 and 30) (c). Arrows indicate points corresponding to the above structures on graph $(N_D - \Delta L)$. (Adapted from Ref. [217].)

either along or normally to C ∼ C bonds to define deformation modes zg and ach.

Tensile deformation mode ach. Since the carbon skeletons of (5, 5)NGr-H2 and (5, 5)NGra molecules are isostructural, details of the deformation process presented in Sections 4.3.5 and 4.3.6 can be omitted and the description is focused on the difference between their behaviors. Graphical dependences $(F - \Delta L)$ and $(N_D - \Delta L)$ characterizing (5, 5)NGra deformation and destruction corresponding to the ach deformation mode are presented in Fig. 45b. For comparison, Fig. 45c demonstrates the analogous dependences for (5, 5)NGr-H2. As discussed in Section 4.3.6, the behavior of (5, 5)NGr-H2 in this deformation mode is traditional for a series of (5, 5)NGr, (5, 5)NGr-Hl, and (5, 5)NGr-H2 molecules.

In all three cases, graphs $(F - \Delta L)$ reveal single-step deformation and destruction processes unrelated to hydrogenation and resulting in uniform molecule stretching during the first 19 steps and C ∼ C bond breaking at the 20th step. [3] The molecule divides by this time into two fragments: a shortened equilibrium one ((5,4)-analog of the molecule) and a sequence of alternating acetylene and carbene chains. Unlike $(F-\Delta L)$ graphs, $(N_D-\Delta L)$ graphs depend on the chemical state of edge atoms (see Fig. 44) and, in the case of (5, 5)NGr-H2, demonstrate weak growth in molecular chemical activity due to gradual C ∼ C lengthening till step 19, after which the activity sharply increases at the 20th step owing to the simultaneous fracture of six C = C bonds. The N_D value thus achieved remains constant, irrespective of the distance between the two fragments of the destroyed molecule.

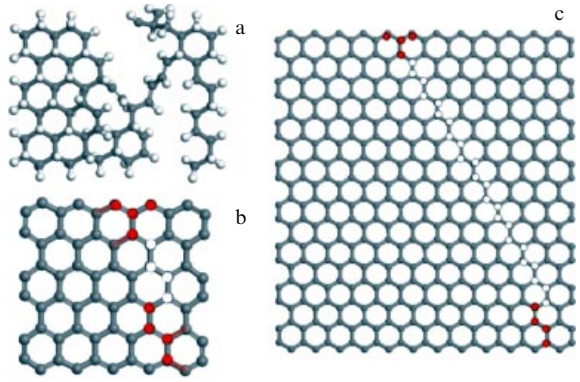

Figure 46. Alkene chain of carbon atoms based on graphane in the ach deformation mode. (a) Equilibrium structures of the (5, 5)NGra molecule at the 31th deformation step. (b, c) Schemes of chain formation in (5, 5)NGra and (15, 12)NGra molecules, respectively; hydrogen atoms are not shown.

As follows from Fig. 45b, deformation and destruction of a (5, 5)NGra molecule occur in quite different ways. Graph $(F - \Delta L)$ illustrates a two-step deformation reminiscent of the tricotage-like process that is totally quenched in (5, 5)NGr-H2 in both deformation modes (see Fig. 43). Note that the two-step behavior holds for the ach mode, whereas such a deformation of graphene occurs in the zg mode. At the first stage, the (5, 5)NGra molecule is uniformly stretched, similar to (5, 5)NGr-H2, but stretching prolongs till step 31. It is not accompanied by breaking C ∼ C single bonds, due to which the number N_D of effectively unpaired electrons remains zero up to the 30th step, as expected for the sp^3 electron system without odd electrons. N_D sharply increases to 14 at step 31, which makes the deformed molecule highly active. The rise in N_D is caused by the fracture of the set of C ∼ C bonds and the formation of a linear alkene-like chain linking the two fragments of the molecule. Further lengthening results in the straightening of the chain over another 40 steps. Thereafter, the chain breaks down, giving rise to two separate loose fragments. The break is associated with a new sharp rise in N_D, which thereafter remains unaltered despite further lengthening.

Clearly, both the chain length and the number of steps needed for the straightening and breaking to proceed depend on the molecular size. The authors of Ref. [217] proposed a

[3] According to study [17], the single C ∼ C bond is regarded as broken if the atoms are spaced 2.15 Å apart. This implies the possibility, in principle, of rather 'long' C–C bonds (longer than 1.53 ± 0.02 Å). Naturally, such cases are rare; in fact, only one 1.65 – 1.66-Å bond was found by the end of study [17]. However, the most recent publication reports a C–C bond as long as 1.8 Å [219].

feasible algorithm of alkene chain formation based on the structural analysis of deformed (5, 5)NGra molecules (Fig. 46). It can be seen that breaking begins from a fracture of two C ~ C bonds in the right bottom corner of the molecule. The adjoining four carbon atoms fasten and strengthen the chain formed from the white atoms arrayed along alkyl configurations of carbon atoms in pristine graphane. Dissociation of two C ~ C bonds in the upper part of the molecule in Fig. 46b liberates the four CH groups that finalize the formation of the cyclohexanoid unit in the undeformed specimen, but create a $(CH)_4$ cluster in the right top corner of the molecule upon formation of the alkene chain. Application of this algorithm to a larger (15, 12)NGra molecule shown in Fig. 46c revealed a trajectory of formation of a long alkene chain that serves as a criterial sign of graphane destruction in the ach deformation mode [217]. It can be speculated that the tendency toward alkene chain formation in the graphane sheet body in the course of stretching results in cracking discovered by molecular dynamics computations [216].

Tensile deformation mode zg. In the case of the zg deformation mode, (5, 5)NGra molecules behave like (5, 5)NGr-H2, i.e., deformation and destruction begin and end at the first stage. Graph ($N_D - \Delta L$) shows that (5, 5)NGra stretching occurs without the C ~ C bond break, so that the number N_D of effectively unpaired electrons remains zero until the 24th step, as expected for the sp^3 electron system without odd electrons. At the 25th step, N_D sharply increases to 11 as a result of molecular rupture.

Comparative analysis. The graphical dependences in Figs 43–45 represent the set of effects accompanying hydrogenation of the initial (5, 5)NGr molecule and allow formulating major differences in the mechanical behavior of graphene and graphane. It follows from the above data that hydrogenation not only strongly suppresses but also alters the character of the multistep deformation and destruction of graphene. The contributions to these processes from edge and basal carbon atoms are essentially different. For example (see Fig. 41), hydrogenation of edge atoms is largely responsible for the suppression of multistep deformation in the zg mode characteristic of graphene. On the contrary, basal atoms control changes in the character of the multistep behavior as a whole, switching it into the ach mode. In the case of graphene, such a behavior appears to indicate that its honeycomb structure is more deformable along C ~ C bonds, including the formation of the linear carbyne chain (see Fig. 41). In contrast to graphene, the multistep (two-step) process is associated with the ach deformation mode (see Fig. 45) more favorable for the formation of the alkene C–C–C chain. This difference is doubtless attributable to the difference between basic structural units of carbon skeletons represented by benzenoid and ach-cyclohexane cycles related to manifestations of the sp^2/sp^3 change in the electronic configuration of carbon atoms in these two cases.

Turning now to the physical reality dealing with macroscopic specimens of graphene and graphane, it is necessary to find the answer to an important question: What peculiar features in the mechanical behavior of the above nanoscale molecules should be expected to occur in real physical objects? In the case of graphene, the answer depends on the role which the edge atoms with truncated valences play in a concrete experiment. Given that such atoms are completely chemically terminated like those fixed over the perimeter of graphene membranes in nanoindentation experiments [187, 205], deformation and destruction of the graphene sheet will be a one-step reaction with characteristics similar to those for (5, 5)NGr-H2. Conversely, if the graphene sample is a nanoribbon with unterminated edge atoms, as in experiment [206], its behavior can be described by the results of a (5, 5)NGr molecule stretching, depending on the type of realizable deformation mode.

In real experiment [206], induced stretching corresponded to the zg deformation mode, which resulted in the formation of a carbyne chain during stretching. Edge atoms of graphane are intrinsically inhibited; therefore, its deformation is totally determined by the behavior of basal plane atoms, meaning that the results obtained for (5, 5)NGra should be just as well expected for a macroscopic sample. In all probability, the formation of alkene chains of carbon atoms stimulated by mechanical loading can result in cracking, which initiates sample disintegration as revealed in molecular dynamics experiment [214].

4.4.4 Energy characteristics of graphane during tensile strain. The difference between graphene and graphane is not reduced to the peculiarities discussed above; it has deeper roots and manifests itself in the specific elastic properties of the two. The dependence of the total energy of a (5, 5)NGra molecule undergoing stretching on the length of the MCI coordinate is shown in Fig. 47a. At first sight, the picture is typical of condensed media and seems to allow resorting to the theory of elasticity in the range of stretches close to the initial length of MCI coordinates for determining elastic properties of the materials in question. However, a detailed

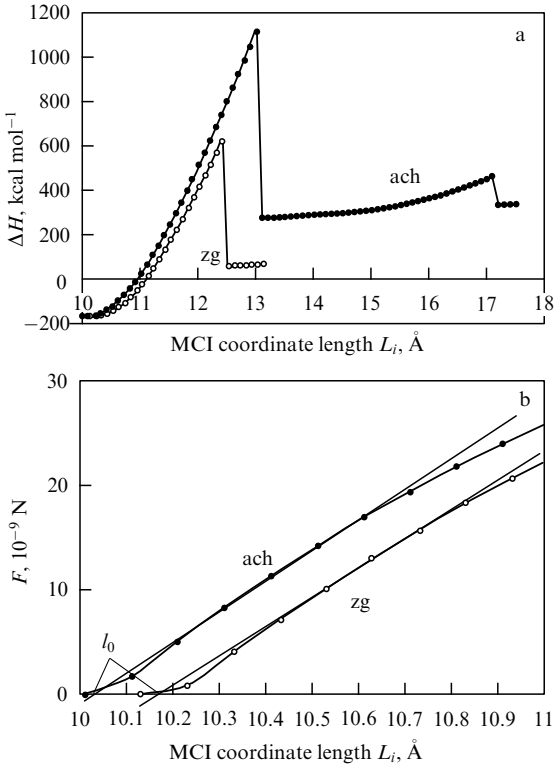

Figure 47. Total energy (a) and response strength (b) depending on the length of the MCI coordinate of the (5, 5)NGra molecule. Dots and circles denote deformation ach and zg modes [217].

analysis of Fig. 47b reveals an explicit conflict with the elasticity theory within this range. The graphs show that the first two points in both curves do not obey the linear dependence and mark the region called the superelastic rubber state in polymer chemistry, where such a situation is rather common [153, 204]. A small region of linear dependence is confined between points 4 and 8. Its approximation up to the intersection point between the linear dependence and the abscissa axis permits determining the initial length l_0 of MCI coordinates corresponding to the beginning of the linear dependence, i.e., elastic deformation. The l_0 values thus derived were used to estimate relative lengthening ε for the construction of dependences of deformation energy $E_s(\varepsilon)$ and stress on the relative lengthening and, finally, for finding Young's moduli [204]. The critical values of the response strength F_{cr}, tension σ_{cr}, relative lengthening ε_{cr}, and Young's modulus E are presented in Table 2. The analysis of energy characteristics allowed the conclusion that graphane deformation is essentially inelastic [superelastic at the onset, and plastic after the relative lengthening reaches 4% (ach-mode) and 2 % (zg-mode)].

Analyzing the energetic mechanical characteristics of (5, 5)NGr and (5, 5)NGra molecules and extending the conclusions to graphene and graphane as real objects of mechanics made it possible to distinguish the following common and different features in the mechanical behavior of these objects as follows [217]:

• The initial stage of graphane deformation is described by the superelastic rubber state, whereas deformation of graphene in this region is characterized as elastic and l_0 value coincident with the starting length L_0 of MCI coordinates.

• The elasticity of graphane in the elastic deformation region is much lower than graphene elasticity.

• The deformation of both graphene and graphane largely occurs in the plastic region.

• Graphene begins to disintegrate at a significantly smaller lengthening than graphane.

These characteristics should be supplemented by one more feature for comparison, namely emergentness which strongly distinguishes graphene from graphane. Emergentness is intrinsic in graphene deformation, whereas graphane lacks this property till rupture. These characteristics, together with peculiarities discussed earlier in this review, provide broad insight into the influence of hydrogenation on the mechanical properties of graphene. The answer to the natural question about the causes of the observed peculiarities should be sought in the consideration of the molecular aspect of the deformation process.

4.4.5 Molecular aspect of graphane deformation. It was shown in Section 4.3.4 that the unique mechanical properties of graphene are associated with the mechanical strength of its benzenoid units. Using the benzene molecule as an image of these units in the framework of the QMCRC approach allowed the explicit mechanical anisotropy of the molecule determining the difference between graphene behavior in ach- and zg deformation modes to be revealed. Table 2 contains the principal mechanical characteristics of a molecule consistent with graphene characteristics, thereby demonstrating their molecular origin. In this context, it is natural to refer to the mechanical properties of the molecule that can reproduce the cyclohexane unit in the ach conformation in graphane. Evidently, the ach isomer of cyclohexane molecule is an adequate model for the purpose. Figure 48 presents a set of

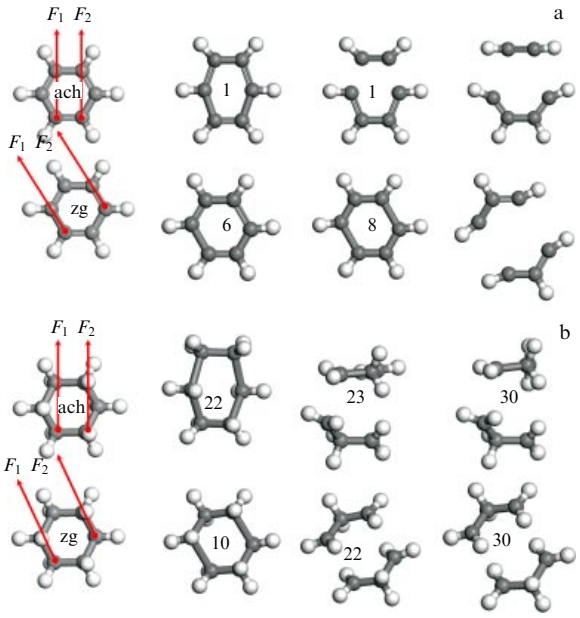

Figure 48. Equilibrium structures of benzene (a) and ach-cyclohexane (b) molecules subjected to stepwise uniaxial stretching. MCI coordinate configuration is shown by the arrows on the left. Numbers indicate deformation steps [217].

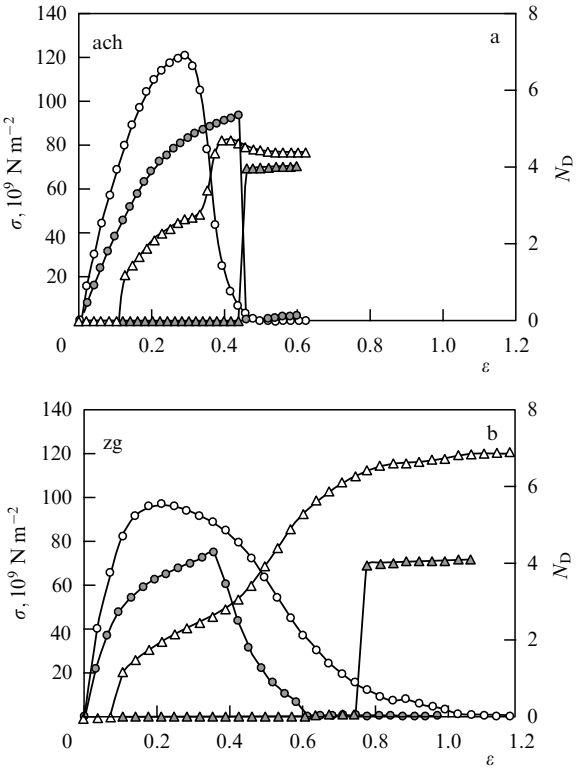

Figure 49. Graphical dependences ($\sigma - \varepsilon$) (curves with circles, left axis) and ($N_D - \varepsilon$) (curves with triangles, right axis) corresponding to ach (a) and zg (b) deformation modes of benzene (unfilled symbols) and ach-cyclohexane (filled symbols) molecules [217].

structures of benzene and ach-cyclohexane molecules subjected to uniaxial stretching described by two pairs of MCI coordinates. Each pair corresponds to either ach- or zg-deformation mode.

Quantitative characteristics of the mechanical behavior of both molecules are compared in Fig. 49. Graphical depen-

dences ($\sigma - \varepsilon$) describe the mechanical behavior, whereas ($N_D - \varepsilon$) graphs demonstrate changes in molecule chemical activity in the course of deformation. Graphs ($\sigma - \varepsilon$) indicate that the high mechanical anisotropy of benzene is much less pronounced in the case of ach-cyclohexane, which is clearly less elastic and disintegrates at lower tension but greater lengthening in both deformation modes. The chemical activity of these two molecules also changes differently. The benzene molecule with its sp^2-electron structure has zero N_D in the absence of deformation due to coincidence of molecule bond lengths and the critical C=C length $R_{cr} = 1.395$ Å. N_D grows gradually to $\varepsilon \sim 0.4$ with C=C lengthening in the course of deformation; it then sharply increases as C=C bonds break down. In a cyclohexane molecule having the sp^3-electronic structure, N_D remains zero till C ~ C bonds break down at deformation steps 23 and 22 in the ach and zg modes, respectively, when N_D rises abruptly to ~ 4.

Mechanical characteristics of both molecules are presented in Table 2, together with analogous characteristics of (5, 5)NGr and (5, 5)NGra. Analyses of these data reveal an explicit similarity among properties of benzene and ach-cyclohexane molecules and of honeycomb structures built by them. These molecular characteristics also explain why graphane is less elastic than graphene and why critical lengthening in graphane is greater and the critical stress smaller. Taken together, these characteristics account for the decrease in graphane's Young's moduli in both deformation modes. Certainly, total coincidence between the properties of molecules and honeycomb associates is hardly possible, because the packing of structural units inevitably affects the mechanical characteristics of the samples considered.

4.5 Mechanical deformation and dynamic properties

As mentioned above, deformation of covalent media is believed to result from the vibrational motion of atoms [153], which implies a close association between the mechanical properties of an object and its vibrational and/or phonon spectra. Thus, in the case of polymers, the elastic region of tensile strain due to chemical bond stretching is determined by valence vibrations of the atoms forming these bonds. Accordingly, parameters of elasticity theory, such as Young's modulus and stiffness, must be proportional to force constants or squares of the frequency of fundamental harmonic vibrations. The superelastic rubber state, unlike elastic deformation, is usually due to the high conformational diversity of polymers originating from low-frequency torsional and deformational vibrations [204].

Deformation of both benzene and cyclohexane molecules, as well as graphene/graphane molecules, depends on double (C=C) and single (C–C) bonds, respectively. The valence self-oscillation frequency of C=C bonds in benzene is $\nu_{C-C}^{BNZ} = 1599$ cm^{-1} [220]. Taking ν_{C-C}^{BNZ} as the reference point permits calculating the respective vibrational frequency of cyclohexane ν_{C-C}^{CHXN}, which must ensure the decrease in Young's modulus, the values of which are presented in Table 2. Let us use the relationship

$$\nu_{C-C}^{CHXN} = \eta \nu_{C-C}^{BNZ}, \tag{18}$$

where

$$\eta = \sqrt{\frac{E^{CHXN}}{E^{BNZ}}}. \tag{19}$$

Here, E^{CHXN} and E^{BNZ} are Young's moduli of the molecules presented in Table 2. The ratio of Young's moduli E^{CHXN}/E^{BNZ} together with η values and frequencies ν_{C-C}^{CHXN} are included in Table 3. The last agree with two molecular frequencies of C–C valence vibrations in cyclohexane, theoretically predicted in monograph [221]. These vibrations are different in shape, which may account for the fact that the elastic deformation of cyclohexane is determined by different oscillation processes associated with two different deformation modes. Column η_{exp} presents expected η ratios derived from Eqn (19) using calculated vibrational frequencies (ν_{C-C}-column).

It is difficult to distinguish regions corresponding to optical phonons in the calculated broadband phonon spectra of graphene [222, 223] and graphane [224] based on C–C valence vibrations. In the case of graphene, however, some evidence of optical phonons corresponding to C–C bond streaching is available for point Γ of the Brillouin zone. The characteristic 1564-cm^{-1} G-band in the Raman scattering spectrum corresponds to these phonons [225]. Using frequency $\nu_{C-C}^{graphene}$, it is possible to determine, based on Eqn (18), the respective frequency for graphane, $\nu_{C-C}^{graphane}$, that must ensure the decrease in Young's modulus presented in Table 2. The corresponding frequencies must fall within a 1095–1170-cm^{-1} range. The calculated phonon spectrum of graphane [224] is produced by pure and mixed (carbon atom-bound) inner phonons lying within the 1000–1330 cm^{-1} range. Hence, the expected range of values from 0.41 to 0.73 for η_{exp} is in excellent agreement with the data in Table 3. Taken together, these observations indicate that the decrease in Young's moduli of graphane compared with that for graphene has a dynamic character and is related to inner

Table 3. Young's moduli and valence oscillation frequencies of C–C bonds.

Objects	Deformation modes	E_σ	η	ν_{C-C}^{CHXN}, cm^{-1}	ν_{C-C}, cm^{-1}	η_{exp}	$\nu_{C-C}^{graphane}$, cm^{-1}	References
Benzene	ach	0.76			1599			[220]
	zg	0.99						
Cyclohexane	ach	0.40	0.72	1159 – 1378	1070 – 1388	0.82 – 0.93		[221]
	zg	0.74	0.86					
Graphene	ach	1.09			1564			[223]
	zg	1.15						
Graphane	ach	0.61	0.75		1000 – 1330	0.41 – 0.73	1095 – 1170	[224]
	zg	0.57	0.70					

phonon softening upon transition from sp^2 to sp^3 electron configuration. Phonon softening is associated with the weakening of the respective C ~ C bonds confirmed in experiment [225].

The hydrogenation of benzene molecules and graphene is accompanied by low-frequency torsional and deformational vibrations [221, 224]. They have no effect on the deformation of individual molecules but may strongly influence the behavior of their linked chains. It can be conjectured that the superelastic rubber state at the early stages of graphane deformation is due to the quite apparent softening of the low-frequency part of the graphane phonon spectrum [224], as opposed to that of graphene.

The dynamic origin of the decrease in Young's modulus provides an opportunity to look narrowly at the elastic parameters of fluorographene $(C_1F_1)_n$ [154], whose phonon spectrum was computed in [224]. Calculations show that inner phonons corresponding to C ~ C valence vibrations occupy the 1100–1330 cm^{-1} region, which allows the expectation of a decrease in Young's modulus for graphene fluoride from 0.71 to 0.50, similar to that for graphane. The first observations in Ref. [154] showed that the fluorographene Young's modulus is ~ 0.3 that of graphene's. These values are in reasonable agreement with predicted ones, despite technical difficulties encountered in obtaining this material.

4.6 Emergent mechanics of graphene: its present and future

The above results of computational and empirical investigations of mechanical properties of graphene and its derivatives give convincing evidence that their deformation at the atomic level is a complicated emergent phenomenon depending on a variety of factors, among which the chemical composition and load orientation relative to chemical bonds most strikingly manifest themselves under the experimental conditions. Naturally, sample size and shape exert a strong influence, too. Nonetheless, self-consistent conceptually substantiated emergent mechanics are a matter of the future. At present, it is still in its infancy and just gaining momentum.

The currently adopted graphene deformation concept provides a powerful tool to speed up this process. The concept has two aspects. The dominant macroscopic continual aspect is a formal corollary of graphene's solid-state nature realized by extension of the theory of continuous media to 2D crystals. In the framework of the microscopic and/or atomistic aspect, graphene deformation is described as a topological mechanochemical reaction, the central component of which is variation of the length of covalent C ~ C bonds in basic elements of the honeycomb structure. The relationship between the two aspects manifests itself in the macroscopic aspect covering the set of microscopic reactions occurring simultaneously in different parts of the sample. Taken together, both aspects are a natural reflection of the molecular–crystalline dualism of graphene and can reinforce each other; the latter is likely to manifest itself in a new remarkable mechanical property, auxetism, recently theoretically predicted in paper [226].

Macroscopic continual approaches in solid state physics making use of empirically found energy parameters of interatomic interactions fairly well reproduce solid-state characteristics of graphene strength. However, these approaches are limited by the framework of the simplified elasticity theory in which deformation of graphene and its derivatives has to be considered an elastic deformation. As a result, a large number of important mechanical properties of plastic graphene are disregarded, which hampers adequate prediction of its mechanical behavior under different conditions. The same limitations do not yet allow predicting prospects for the further development of the solid-state aspect. In contrast, these prospects are very apparent in the framework of the atomistic approach. Specifically, the algorithm based on the QMCRC approximation brings to light the following peculiarities:

(1) the high strength of chemical C ~ C bonds (both double and single);

(2) the mechanical anisotropy of hexagonal units of the honeycomb structure (graphene benzenoid units and cyclohexane units of its derivatives) arising from various orientations of applied loads with respect to chemical bond direction.

These factors determine the reaction of graphene and its derivatives to any mechanical impact controlled by the change in lengths of their covalent bonds, which accounts for the essentially plastic deformation of these materials. Continuous and irregular variation of C ~ C bond lengths in these objects during deformation can be represented in terms of standard continuous media mechanics as dislocation motion in solid bodies responsible for their pronounced plasticity. In addition, the formation of new chemical bonds C ~ X (X = H, O, F, N, etc.) uninvolved directly in the stretching of C ~ C bonds of the carbon skeleton but performing torsional movements around these bonds causes the superelastic rubber state manifested at the early stages of deformation of chemically modified graphene.

Apart from the aforementioned consequences of the atomistic approach, the variation of covalent bond lengths and their dispersion in response to mechanical impacts influences the correlation of odd p_z-electrons and related spin effects discussed at length in all sections of the present review. Clearly, these effects form the basis of graphene emergent mechanics and await further detailed consideration of themselves and in combination with disturbances of spin and time symmetry caused by mechanical deformation.

5. Conclusions

To conclude the story of the emergent properties of graphene, we cannot help mentioning one more unusual manifestation of emergentness to be considered in connection with new quasiparticles and their relation to graphene. R B Laughlin was the first to raise the question of emergentness of quasiparticles in Ref. [3] by stating that "*One of the things an emergent phenomenon can do is create new particles*." Simultaneously, the author emphasized that phonons are intrinsic constituents of the crystalline state and disappear together with the crystal. He similarly treated solitons and predicted, based on the fractional quantum Hall effect (FQHE) [227], the appearance of a new quantum particle with fractional charge [228], which was later called the *anyon*. It brought him the Nobel Prize in Physics in 1998. Anyons can exist only in 2D crystals exhibiting FQHE. All attempts to find and observe anyons failed and had practically been forgotten by 2010 when the Nobel Prize in Physics was awarded for the discovery of graphene. However, as soon as 2014 the first report of FQHE in bilayer graphene [229] was published, followed in two years by its confirmation [230]. No wonder the authors of another recent article proposed to

visualize the interaction of anyons responsible for FQHE [231] in graphene and confirm their origin as a topological quantum phase of matter, i.e., a new emergent phenomenon. There is little doubt that the unique properties of graphene will manifest themselves in this case, too. Then, the list of its crystalline emergents will be supplemented by a new quasiparticle, the anyon, while the list of Nobel Prizes in Physics 20... by another achievement, a surprising combination of FQHE and graphene.

The problem of real particles and fields, in addition to quasiparticles, also fell within the scope of graphenics. Photons, plasmons, electrons, and positrons are known to exist and interact in graphene in a specific way, as demonstrated in numerous review articles and monographs. In this context, an exclusive position is granted to new particles, bondons [6], or quanta of chemical fields. The possibility of observing them depends on spontaneous symmetry breaking and therefore relates to emergent phenomena. Graphenes may be of value for identifying conditions for the reliable observation of bondons [10].

These up-to-date findings of empirical graphenics should be supplemented by the latest events in virtual graphenics. As was mentioned in the Introduction, modern virtual DFT-TB graphenics espouses reductionist views and is essentially nonemergent. We tried to show in this review that the reductionist concept is in conflict with physical reality giving convincing evidence of the emergent electron system of graphene. However, today as half a century ago, it is an established opinion that the key question concerning the possibility of restoration of continuous symmetry has an *a priori* affirmative answer which can be derived from purely theoretical considerations by slightly complicating the RQC solution with the use of either holomorphic RHF and the theory of catastrophe [232] or spin projection HF [233]. True, the positive answer in these cases, as many years ago [1–5], was obtained only for two- and three-atom molecules of O_2 and H_3. As far as DFT programs are concerned, there is a tendency toward better understanding that "*the use of methods that cannot correctly describe the character of open shells leads to catastrophically incorrect structures*" [234]. The recent work of Kaplan [235] once again emphasizes the necessity to pay attention to the conceptual boundedness of the DFT approximation applicability to electron systems with degenerate states taking account of the spin. Furthermore, some steps are taken to transform the current Kohn–Sham DFT algorithms into more sophisticated ones, such as spin-flip (SF) algorithms of the time-dependent density functional theory (TDDFT) [236]. The possibility of restoring continuous symmetry in the case of open-shell molecules is tacitly implied.

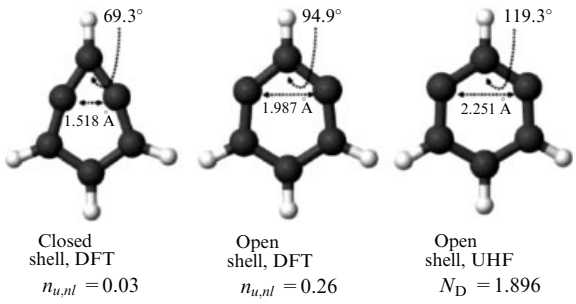

Figure 50. Numbers of effectively unpaired electrons in meta-benzene calculated in the Kohn–Sham DFT approximation, SF-TDDFT (both in Ref. [236]), and UHF.

The results of Ref. [236] make it possible to once again return to the disadvantages of applying the DFT method, even in its improved version, to the description of such molecules. Figure 50 presents results of calculations of one of the emergent order parameters (the total number of effectively unpaired electrons of these molecules) by two DFT methods and UHF. A zero value of $n_{u,nl}$ in the case of the Kohn–Sham algorithm is self-evident because of its closed-shell nonemergent character. Transition to the SF-TDDFT algorithm markedly improves the situation by convincingly demonstrating the open-shell character of the molecule. However, $n_{u,nl}$ value remains almost an order of magnitude smaller than N_D calculated in the UHF approximation. The difference can be partly attributed to the calculation of $n_{u,nl}$ and N_D using different formulas [237]. Nonetheless, it cannot be greater than twofold. The remaining difference reflects the inefficiency of the DFT method in this case.

Recognition of symmetry breaking as the leading factor with respect to its universality and understanding the emergent character of graphene properties open up a new paradigm of graphene applications. 'Clever' graphene material, as opposed to ordinary graphene, may prove more attractive and easier to implement in various devices to accelerate realization of high-performance applications. This conclusion is confirmed by extraordinary interface phenomena associated with ferromagnetism, spin filtration, and superconductivity considered in the review. Naturally, interfacial emergent phenomena revealed for the first time in physics have a common motif and can be considered in different areas of graphenics. Recent studies demonstrated enhanced charge transfer through the organic semiconductor/graphene interface [238]. Equally interesting is the formation of an organic spin interface with a magnetic coercive force at room temperature; it was prepared using phthalocyanine molecules deposited over a graphene-coated cobalt layer [239].

Even more interesting evidence of the role of interface was obtained in geology: the unique structure of nano-sized quartz inclusions built into shungite carbon (technical graphene). The nanoquartz enclosed in shungite carbon (unlike usual quartz highly variable in terms of chemical composition, defective structure, and size depending on birthplace) has a perfect crystal structure and practically equal size (~ 80 nm), irrespective of the shungite source [240]. It can be supposed that the quartz/shungite interface obeying emergent rules of graphene chemistry plays a key role in the formation of this structurally complicated mineral. There is reason to expect similar phenomena in graphene-based biomedicine, where graphene-containing interfaces are becoming a frequent occurrence.

The history of graphene continues and is taking shape right before our eyes. Time is running fast, and we are sure to witness many new interesting discoveries in the near future that will not only reveal still veiled secrets of graphenes but also strongly influence current views in the natural sciences.

Acknowledgments

The authors are deeply grateful to I S Burmistrov and M F Budyka for fruitful and enlightening discussions. This publication was supported by Program 5-100 of the People's Friendship University of Russia.

The idea for this review belongs to E F Sheka who, moreover, wrote Sections 2 and 3 and edited Section 4. N A Popova and V A Popova participated in drafting the text and collecting and treating materials for Section 4.

List of abbreviations

ACS — atomic chemical susceptibility
AFMI — aniferromagnetic Mott insulator
ARPES — angle-resolved photoelectron spectroscopy
CI — configuration interaction
DFT — density functional theory
DMRG — density matrix renormalization group (method)
EELS — electron energy loss spectrum
FQHE — fractional quantum Hall effect
GCHF — generalized complex Hartree–Fock (approximation)
GCN — graphitic carbon nitride
GHF — generalized Hartree–Fock (approximation)
HOMO — highest occupied molecular orbitals
KRHF — Kramers' restricted Hartree–Fock (approximation)
KUHF — Kramers' unrestricted Hartree–Fock (approximation)
LUMO — lowest unoccupied molecular orbitals
MCI — mechanochemical intrinsic (coordinates)
MCS — molecular chemical susceptibility
NC-AFM — noncontact atomic force microscopy
NRQCh — nonrelativistic quantum chemistry
PAH — polyaromatic hydrocarbons
PT — perturbation theory
QC — quantum-chemical
QMCRC — quantum mechanochemical coordinate (approach)
QSHI — quantum spin Hall insulator
QSL — quantum spin liquid
RHF — restricted Hartree-Fock (method)
ROHF — restricted Hartree-Fock approximation for open-shell molecules
RQC — relativistic quantum chemistry
RQCh — restricted quantum-chemical (approximation)
RSD — restricted single determinant
SEM — scanning electron microscope
SF — spin flip
SF-TDDFT — spin-flip time-dependent density functional theory (algorithm)
SM — semimetal
SOC — spin-orbital coupling
STEM — scanning transmission electron microscope
STM — scanning tunneling microscope
TB — tight binding (approximation)
TDDFT — time-dependent density functional theory
TEM — transmission electron microscope
TI — topological insulator
UDFT — unrestricted density functional theory (approximation)
UHF — Unrestricted Hartree–Fock (method)

References

1. Anderson P W *Science* **177** 393 (1972)
2. Laughlin R B *Rev. Mod. Phys.* **71** 863 (1999); *Usp. Fiz. Nauk* **170** 292 (2000)
3. Laughlin R B, Pines D *Proc. Natl. Acad. Sci. USA* **97** 28 (2000)
4. Yannouleas C, Landman U *Rep. Prog. Phys.* **70** 2067 (2007)
5. Pavarini E, Koch E, Schollwöck U (Eds) *Emergent Phenomena in Correlated Matter, Autumn School, Jülich, 23–27 September 2013* Vol. 3 (Eds E Pavarini, E Koch, U Schollwöck) (Jülich: Forschungszentrum Jülich and the German Research School for Simulation Sciences, 2013
6. Putz M V et al., in *Distance, Symmetry, and Topology in Carbon Nanomaterials* (Carbon Materials: Chemistry and Physics, Vol. 9, Eds A R Ashrafi, M V Diudea) (New York: Springer, 2016) p. 345
7. Hempel C, Oppenheim P, in *Emergence: Contemporary Readings in Philosophy and Science* (Eds M A Bedau, P Humphreys) (Cambridge, Mass.: MIT Press, 2008) p. 61; originally published in Hempel C G *Aspects of Scientific Explanation, and Other Essays in the Philosophy of Science* (New York: Free Press, 1965)
8. Earman J, in *Symmetries in Physics: Philosophical Reflections* (Eds K Brading, E Castellani) (Cambridge: Cambridge Univ. Press, 2003) p. 335
9. Butterfield J *Found. Phys.* **41** 1065 (2011)
10. Putz M V, Ori O *Chem. Phys. Lett.* **548** 95 (2012)
11. Jalbout A F, Ortiz Y P, Seligman T H *Chem. Phys. Lett.* **564** 69 (2013)
12. Löwdin P-O *Adv. Chem. Phys.* **2** 207 (1959)
13. Kitagawa Y et al. *J. Phys. Chem. A* **113** 15041 (2009)
14. Coe J P, Paterson M J *Int. J. Quantum Chem.* **116** 1772 (2016)
15. Cui Y et al. *J. Chem. Phys.* **139** 154107 (2013)
16. Novoselov K S et al. *Nature* **490** 192 (2012)
17. Sheka E *Adv. Quantum Chem.* **70** 111 (2015)
18. Sheka E *Fullerenes: Nanochemistry, Nanomagnetism, Nanomedicine, Nanophotonics* (Boca Raton, FL: CRC Press, 2011)
19. Sheka E *Spin Chemical Physics of Graphene* (Singapore: Pan Stanford, 2017)
20. Blanquart G *Int. J. Quantum Chem.* **115** 796 (2015)
21. Kaplan I G *Int. J. Quantum Chem.* **107** 2595 (2007)
22. Jacob C R, Reiher M *Int. J. Quantum Chem.* **112** 3661 (2012)
23. Fucutome H *Int. J. Quantum Chem.* **20** 955 (1981)
24. Takatsuka K, Fueno T, Yamaguchi K *Theor. Chim. Acta* **48** 175 (1978)
25. Staroverov V N, Davidson E R *Chem. Phys. Lett.* **330** 161 (2000)
26. Sheka E F, Zayets V A *Russ. J. Phys. Chem.* **79** 2009 (2005); *Zh. Fiz. Khim.* **79** 2250 (2005)
27. NWChem. Release66, http://www.nwchem-sw.org/index.php/Release66:Density_Functional_Theory_for_Molecules#ODFT_and_MULT_–
28. Gaussian 03 Online Manual. Stable, http://www.lct.jussieu.fr/manuels/Gaussian03/g_ur/k_stable.htm
29. Sheka E F *Int. J. Quantum Chem.* **114** 1079 (2014)
30. Gross L et al. *Science* **337** 1326 (2012)
31. Pavliček N et al. *Nature Nanotechnol.* **12** 308 (2017)
32. Mönig H et al. *Nature Nanotechnol.* **13** 371 (2018)
33. Sheka E F, unpublished UHF data (2018)
34. Van der Lit J et al. *Nature Commun.* **4** 2023 (2013)
35. Sheka E F *Int. J. Quantum Chem.* **112** 3076 (2012)
36. Sheka E F *Int. J. Quantum Chem.* **107** 2803 (2007)
37. Sheka E F *J. Struct. Chem.* **47** 593 (2006); *Zh. Strukt. Khim.* **47** 613 (2006)
38. Warner J H et al. *Nano Lett.* **14** 6155 (2014)
39. Nakada Ket al. *Phys. Rev. B* **54** 17954 (1996)
40. Barnard A S, Snook I K *Modelling Simulat. Mater. Sci. Eng.* **19** 054001 (2011)
41. Acik M, Chabal Y J *Jpn. J. Appl. Phys.* **50** 070101 (2011)
42. Mishra P C, Yadav A *Chem. Phys.* **402** 56 (2012)
43. Ang L S, Sulaiman S, Mohamed-Ibrahim M I *Monatsh. Chem. Chem. Monthly* **144** 1271 (2013)
44. Hoffmann R *Angew. Chem. Int. Ed.* **52** 93 (2013)
45. Mayer I *Int. J. Quantum Chem.* **29** 73 (1986)
46. Sheka E F, Popova N A *J. Mol. Model.* **18** 3751 (2012)
47. Sheka E F, Popova N A *Phys. Chem. Chem. Phys.* **15** 5304 (2013)
48. Elias D C et al. *Science* **323** 610 (2009)
49. Sofo J O, Chaudhari A S, Barber G D *Phys. Rev. B* **75** 153401 (2007)
50. Chuo C K, Pumera M *Chem. Soc. Rev.* **43** 291 (2014)
51. Liu W *Mol. Phys.* **108** 1679 (2010)
52. Dyall K, Faegri K *Introduction to Relativistic Quantum Chemistry* (New York: Oxford Univ. Press, 2007)

53. Reiher M, Wolf A *Relativistic Quantum Chemistry*: *The Fundamental Theory of Molecular Science* (New York: John Wiley and Sons, 2014)
54. Löwdin P-O, Mayer I *Adv. Quantum Chem.* **24** 79 (1992)
55. Marian C M, in *Reviews in Computational Chemistry* Vol. 17 (Eds K B Lipkowitz, D B Boyd) (New York: John Wiley and Sons, 2001), p. 99
56. Kim Y S et al. *Int. J. Quantum Chem.* **66** 98 (1996)
57. Nakano M, Seino J, Nakai H *Int. J. Quantum Chem.* **117** e25356 (2017)
58. Bučinský L et al. *Comput. Theor. Chem.* **1065** 27 (2015)
59. Wallace P R *Phys. Rev.* **71** 622 (1947)
60. Slonczewski J C, Weiss P R *Phys. Rev.* **109** 272 (1958)
61. Kane C L, Mele E J *Phys. Rev. Lett.* **95** 226801 (2005)
62. Katsnelson M I *Mater. Today* **10** 20 (2007)
63. Geim A K, Novoselov K S *Nature Mater.* **6** 183 (2007)
64. Kim P "Graphene and relativistic quantum physics", in *Matière de Dirac, Séminaire Poincaré XVIII* (Paris: Institut Henri Poincaré, 2014) p. 1
65. Hwang C et al. *Sci. Rep.* **2** 590 (2012)
66. Kara A et al. *Surf. Sci. Rep.* **67** 1 (2012)
67. Sheka E F *Nanosyst. Phys. Chem. Math.* **7** 983 (2016)
68. Zhang R et al. *Phys. Chem. Chem. Phys.* **18** 28134 (2016)
69. Gomes K K et al. *Nature* **483** 306 (2012)
70. Bhimanapati G R et al. *ACS Nano* **9** 11509 (2015)
71. Xu L-C, Du A, Kou L *Phys. Chem. Chem. Phys.* **18** 27284 (2016)
72. Wang C et al. *AIP Adv.* **6** 035204 (2016)
73. Li W et al. *Sci. Bull.* **63** 282 (2018)
74. Shao Y et al. *Nano Lett.* **18** 2133 (2018)
75. Wang A, Zhang X, Zhao M *Nanoscale* **6** 11157 (2014)
76. Zhang X, Wang A, Zhao M *Carbon* **84** 1 (2015)
77. Wei L, Zhang X, Zhao M *Phys. Chem. Chem. Phys.* **18** 8059 (2016)
78. Zhang H et al. *Nano Lett.* **16** 6124 (2016)
79. Si C et al. *Nano Lett.* **16** 6584 (2016)
80. Wang J et al. *Natl. Sci. Rev.* **2** 22 (2015)
81. Tsipas P et al. *ACS Nano* **12** 1696 (2018)
82. Kochat V et al. *Sci. Adv.* **4** e1701373 (2018)
83. Mounet N et al. *Nature Nanotechnol.* **13** 246 (2018)
84. Sheka E F, Orlenko E V *Fullerenes Nanotubes Carbon Nanostruct.* **25** 289 (2017)
85. Hohenadler M, Assaad F F *J. Phys. Condens. Matter* **25** 143201 (2013)
86. Mayorov A S et al. *Nano Lett.* **12** 4629 (2012)
87. Ortmann F et al. (Eds) *Topological Insulators*: *Fundamentals and Perspectives* (Chichester: Wiley, 2015)
88. Schüler M et al. *Phys. Rev. Lett.* **111** 036601 (2013)
89. Bach V, Lieb E H, Solovej J P *J. Stat. Phys.* **76** 3 (1994)
90. Zheng D, Zhang G-M, Wu C *Phys. Rev. B* **84** 205121 (2011)
91. Lu G et al. *Nanoscale* **5** 1353 (2013)
92. Chernozatonskii L A et al. *JETP Lett.* **85** 77 (2007); *Pis'ma Zh. Eksp. Teor. Fiz.* **85** 84 (2007)
93. Lu N et al. *J. Chem. Phys.* **133** 034502 (2010)
94. Pan S, Aksay I A *ACS Nano* **5** 4073 (2011)
95. Nebogatikova N A et al. *Phys. Chem. Chem. Phys.* **17** 13257 (2015)
96. Wang X, Bai H, Shi G *J. Am. Chem. Soc.* **133** 6338 (2011)
97. Kang J H et al. *Chem. Mater.* **28** 756 (2016)
98. Balog R et al. *Nature Mater.* **9** 315 (2010)
99. Jørgensen J H et al. *ACS Nano* **10** 10798 (2016)
100. Batzill M *Surf. Sci. Rep.* **67** 83 (2012)
101. Vlassiouk I V et al. *Nature Mater.* **17** 318 (2018)
102. Edmonds M T et al. *Science Adv.* **3** eaao6661 (2017)
103. Sepkhanov R A et al. *Phys. Rev. A* **75** 063813 (2007)
104. Haldane F D M, Raghu S *Phys. Rev. Lett.* **100** 013904 (2008)
105. Ling L, Joannopoulos J D, Soljačić M *Nature Photon.* **8** 821 (2014)
106. Tarruell L et al. *Nature* **483** 302 (2012)
107. Graß T et al. *2D Mater.* **4** 015039 (2016)
108. Jacqmin T et al. *Phys. Rev. Lett.* **112** 116402 (2014)
109. Wang S et al. *Nature Nanotechnol.* **13** 29 (2018)
110. Hubač I, Čársky P *Int. J. Quantum Chem.* **24** 141 (1983)
111. Yazyev O V *Rep. Prog. Phys.* **73** 056501 (2010)
112. Esquinazi P et al. *Phys. Rev. Lett.* **91** 227201 (2003)
113. Sepioni M et al. *Phys. Rev. Lett.* **105** 207205 (2010)
114. Nair R R et al. *Nature Phys.* **8** 199 (2012)
115. Eng A Y S et al. *ACS Nano* **7** 5930 (2013)
116. Nair R R et al. *Nature Commun.* **4** 2010 (2013)
117. Wang Y et al. *Nano Lett.* **9** 220 (2009)
118. Sheka E F, Golubev E A *Tech. Phys.* **61** 1032 (2016); *Zh. Tekh. Fiz.* **86** (7) 74 (2016)
119. Tada K et al. *Phys. Rev. Lett.* **107** 217203 (2011)
120. Ning G et al. *Carbon* **51** 390 (2013)
121. Magda G Z et al. *Nature* **514** 608 (2014)
122. Zvezdin A K et al. *Redkozemel'nye Iony v Magnitnouporyadochennykh Kristallakh* (Rare-Earth Ions in Magnetically Ordered Crystals) (Moscow: Nauka, 1985)
123. Van Vleck J H *The Theory of Electric and Magnetic Susceptibilities* (Oxford: The Clarendon Press, 1932)
124. Adamo C et al. *J. Chem. Phys.* **124** 107101 (2006)
125. Noodleman L *J. Chem. Phys.* **74** 5737 (1981)
126. Kahn O *Molecular Magnetism* (New York: VCH, 1993)
127. Gao X et al. *J. Phys. Chem. C* **112** 12677 (2008)
128. Enoki T, Kobayashi Y *J. Mater. Chem.* **15** 3999 (2005)
129. Sheka E F, Zaets V A, Ginzburg I Ya *JETP* **103** 728 (2006); *Zh. Eksp. Teor. Fiz.* **103** 728 (2006)
130. Nai C T et al. *ACS Nano* **10** 1681 (2016)
131. Hasan M Z, Kane C L *Rev. Mod. Phys.* **82** 3045 (2010)
132. Borovik E S, Eremenko V V, Mil'ner A S *Lektsii po Magnetizmu* (Lectures on Magnetism) (Moscow: Fizmatlit, 2005)
133. Fu L, Kane C L *Phys. Rev. Lett.* **102** 216403 (2009)
134. Akhmerov A R, Nilsson J, Beenakker C W J *Phys. Rev. Lett.* **102** 216404 (2009)
135. Abanin D A, Pesin D A *Phys. Rev. Lett.* **106** 136802 (2011)
136. Dreiser J et al. *ACS Nano* **10** 2887 (2016)
137. Liu Q et al. *Phys. Rev. Lett.* **102** 156603 (2009)
138. Efimkin D K, Galitski V *Phys. Rev. B* **89** 115431 (2014)
139. Checkelsky J G et al. *Nature Phys.* **8** 729 (2012)
140. Katmis F et al. *Nature* **533** 513 (2016)
141. Cobas E D et al. *ACS Nano* **10** 10357 (2016)
142. Khoo K H et al. *ACS Nano* **10** 11219 (2016)
143. Valli A et al. *Nano Lett.* **18** 2158 (2018)
144. Zhang L et al. *ACS Nano* **10** 3816 (2016)
145. Zhang L et al. *ACS Nano* **11** 6277 (2017)
146. Song K et al. *Nano Lett.* **18** 2033 (2018)
147. Heersche H B et al. *Nature* **446** 56 (2007)
148. Tan Z B et al. *Phys. Rev. Lett.* **114** 096602 (2015)
149. Di Bernardo A et al. *Nature Commun.* **8** 14024 (2017)
150. Cao Y et al. *Nature* **555** 151 (2018)
151. Akinwande D et al. *Extreme Mech. Lett.* **13** 42 (2017)
152. Liu M et al. *ACS Nano* **7** 10075 (2013)
153. Tashiro K, Kobayashi M, Tadacoro H *Polymer J.* **24** 899 (1992)
154. Nair R R et al. *Small* **6** 2877 (2010)
155. Tobolsky A, Eyring H *J. Chem. Phys.* **11** 125 (1943)
156. Georgiou T et al. *Appl. Phys. Lett.* **99** 093103 (2011)
157. Ritter S K, Bryson R, Blair T K *Chem. Eng. News* **88** 13 (2010)
158. Kane C L, Mele E J *Phys. Rev. Lett.* **78** 1932 (1997)
159. Sasaki K, Saito R *Prog. Theor. Phys. Suppl.* **176** 253 (2008)
160. Levy N et al. *Science* **329** 544 (2010)
161. Georgi A et al. *Nano Lett.* **17** 2240 (2017)
162. Cervetti C et al. *Nature Mater.* **15** 164 (2016)
163. Osváth Z et al. *Nanoscale* **7** 5503 (2015)
164. Osváth Z et al. *Nanoscale* **6** 6030 (2014)
165. Gill S T et al. *ACS Nano* **9** 5799 (2015)
166. Vinogradov N A et al. *J. Phys. Chem. C* **115** 9568 (2011)
167. Li G et al. *Appl. Phys. Lett.* **100** 013304 (2012)
168. Sheka E F, Shaymardanova L Kh *J. Mater. Chem.* **21** 17128 (2011)
169. Sheka E F, in *Topological Modelling of Nanostructures and Extended Systems* (Carbon Materials: Chemistry and Physics, Vol. 7, Eds A R Ashrafi et al.) (Berlin: Springer, 2013) p. 137
170. Zhang Y et al. *Nano Lett.* **18** 2098 (2018)
171. Wu Q et al. *Chem. Commun.* **49** 677 (2013)
172. Bissett M A et al. *ACS Nano* **7** 10335 (2013)
173. Rossi A et al. *J. Phys. Chem. C* **119** 7900 (2015)
174. Moritz W et al. *Phys. Rev. Lett.* **104** 136102 (2010)
175. Boukhvalov D W, Katsnelson M I *J. Phys. Chem. C* **113** 14176 (2009)
176. Goler S et al. *J. Phys. Chem. C* **117** 11506 (2013)
177. Castellanos-Gomez A et al. *Nano Res.* **58** 550 (2012)

178. Galiotis C et al. *Annual Rev. Chem. Biomol. Eng.* **6** 121 (2015)
179. Young R J et al. *Composit. Sci. Technol.* **72** 1459 (2012)
180. Suk J W et al. *Phys. Status Sol. RRL* **9** 564 (2015)
181. Shioya H et al. *Nano Lett.* **15** 7943 (2016)
182. Griep M et al. *Nano Lett.* **16** 1657 (2016)
183. Chen P-Y et al. *Adv. Mater.* **28** 3564 (2016)
184. Kudin K, Scuseria G E, Yakobson B I *Phys. Rev. B* **64** 235406 (2001)
185. Liu F, Ming P, Li J *Phys. Rev. B* **76** 064120 (2007)
186. Hemmasizadeh A et al. *Thin Solid Films* **516** 7636 (2008)
187. Wei X et al. *Phys. Rev. B* **80** 205407 (2009)
188. Shokrieh M M, Rafiee R *Mater. Design* **31** 790 (2010)
189. Li C, Chou T-W *Int. J. Solids Struct.* **40** 2487 (2003)
190. Sakhaee-Pour A *Solid State Commun.* **149** 91 (2009)
191. Hashemnia K, Farid M, Vatankhah R *Comput. Mater. Sci.* **47** 79 (2009)
192. Tsai J-L, Tu J-F *Mater. Design* **31** 194 (2010)
193. Bu H et al. *Phys. Lett. A* **373** 3359 (2009)
194. Van Lier G et al. *Chem. Phys. Lett.* **326** 181 (2000)
195. Gao Y, Hao P *Physica E* **41** 1561 (2009)
196. Topsakal M, Ciraci S *Phys. Rev. B* **81** 024107 (2010)
197. Sheka E F et al. *JETP* **112** 602 (2011); *Zh. Eksp. Teor. Fiz.* **139** 695 (2011)
198. Sheka E F et al. *J. Mol. Model.* **17** 1121 (2011)
199. Popova N A "Gidrirovanie i deformatsiya grafena v priblizhenii molekulyarnoi teorii" ("Hydrogenation and deformation of graphene in the molecular theory approximation"), PhD Thesis of Phys.-math. sci. (Moscow: RUDN Univ., 2011)
200. Sheka E F, Popova V A, Popova N A, in *Advances in Quantum Methods and Applications in Chemistry, Physics, and Biology* (Progress in Theoretical Chemistry and Physics, Vol. 27, Eds J Maruani, S Wilson) (Berlin: Springer, 2013) p. 285
201. Maeda S et al. *Int. J. Quantum Chem.* **115** 258 (2015)
202. Dewar M J S *Fortschr. Chem. Forsch.* **23** 1 (1971)
203. Khavryutchenko V et al. *Phys. Low-Dim. Struct.* **6** 65 (1995)
204. Nikitina E A et al. *J. Phys. Chem. A* **103** 11355 (1999)
205. Lee C et al. *Science* **321** 385 (2008)
206. Jin C et al. *Phys. Rev. Lett.* **102** 205501 (2009)
207. Jhon Y I et al. *Carbon* **66** 619 (2014)
208. Zhou C et al. *Nanoscale Res. Lett.* **9** 26 (2007)
209. Sahin H et al. *WIREs Comput. Mol. Sci.* **5** 255 (2015)
210. Savchenko A *Science* **323** 589 (2009)
211. Munos E et al. *Diam. Rel. Mat.* **19** 368 (2010)
212. Topsakal V, Cahangirov S, Ciraci S *Appl. Phys. Lett.* **96** 091912 (2010)
213. Leenaerts O et al. *Phys. Rev. B* **82** 195436 (2010)
214. Cadelano E et al. *Phys. Rev. B* **82** 235414 (2010)
215. Scarpa F, Chowdhury R, Adhikari S *Phys. Lett.* **375** 2071 (2011)
216. Pei Q X, Zhang Y W, Shenoy V B *Carbon* **48** 898 (2010)
217. Popova N A, Sheka E F *J. Phys. Chem. C* **115** 23745 (2011)
218. Colombo L, Giordano S *Rep. Prog. Phys.* **74** 116501 (2011)
219. Ishigaki et al. *Chem.* **4** 795 (2018)
220. Gribov L A, Dement'ev V A, Todorovskii A T *Interpretirovannye Kolebatel'nye Spektry Alkanov, Alkenov i Proizvodnykh Benzola* (Interpreted Vibrational Spectra of Alkanes, Alkenes and Benzene Derivatives) (Moscow: Nauka, 1986)
221. Eliashberg M E et al. *Interpretirovannye Kolebatel'nye Spektry Uglevodorodov — Proizvodnykh Tsiklogeksana i Tsiklopentana* (Interpreted Vibrational Spectra of Hydrocarbons — Derivatives of Cyclohexane and Cyclopentane) (Moscow: Nauka, 1988)
222. Mohr M et al. *Phys. Rev. B* **76** 035439 (2007)
223. Adamyan V, Zavalniuk V *J. Phys. Condens. Matter* **23** 015402 (2011)
224. Peelaers H et al. *Appl. Phys. Lett.* **98** 051914 (2011)
225. Sun C Q et al. *J. Phys. Chem. C* **113** 16464 (2009)
226. Burmistrov I S et al. *Phys. Rev. B* **97** 125402 (2018)
227. Laughlin R B *Phys. Rev. Lett.* **50** 1395 (1983)
228. Arovas D, Schrieffer J R, Wilczek F *Phys. Rev. Lett.* **53** 722 (1984)
229. Ki D-K et al. *Nano Lett.* **14** 2135 (2014)
230. Diankov G et al. *Nature Commun.* **7** 13908 (2016)
231. Papić Z et al. *Phys. Rev. X* **8** 011037 (2018)
232. Burton H G A, Gross M, Thom A J W *J. Chem. Theory Comput.* **14** 607 (2018)
233. Lestrange P J et al. *J. Chem. Theory Comput.* **14** 588 (2018)
234. Krylov A I, in *Reviews in Computational Chemistry* Vol. 30 (Eds A L Parrill, K B Lipkowitz) (New York: John Wiley and Sons, 2017) p. 151
235. Kaplan I *Mol. Phys.* **116** 658 (2018)
236. Orms N et al. *J. Chem. Theory Comput.* **14** 638 (2018)
237. Head-Gordon M *Chem. Phys. Lett.* **372** 508 (2003)
238. Boulanger N et al. *Phys. Chem. Chem. Phys.* **20** 4422 (2018)
239. Avvisati G et al. *Nano Lett.* **18** 2268 (2018)
240. Sadovnichii R V et al. *Tr. Karel'skogo Nauch. Tsentra Ross. Akad. Nauk. Ser. Geologiya Dokembriya* (2) 73 (2016)